

**Critical analysis on the suitability of a Constant Properties Model (CPM) for performance
analysis of thermoelectric generators**

Von der Fakultät für Ingenieurwissenschaften,
Abteilung Elektrotechnik und Informationstechnik
der Universität Duisburg-Essen

zur Erlangung des akademischen Grades

Doktor der Naturwissenschaften (Doctor rerum naturalium)

genehmigte Dissertation

von

Prasanna Ponnusamy

aus

Chennai, Indien

1. Gutachter: Jun. Prof. Dr. Johannes de Boor
2. Gutachter: apl. Prof. Dr. rer. nat. habil. Armin Feldhoff

Tag der mündlichen Prüfung: 18.10.2022

This cumulative thesis contains the following publications:

1. **Chapter 3 (Paper 1):** Ponnusamy, P., J. de Boor, and E. Müller, *Using the constant properties model for accurate performance estimation of thermoelectric generator elements*. Applied Energy, 2020. **262**: p. 114587.
2. **Chapter 4 (Paper 2):** Ponnusamy, P., de Boor, J., and Müller, E., *Discrepancy between constant property model and temperature dependent material properties for performance estimation of thermoelectric generators*. Entropy 22.10 (2020): 1128.
3. **Chapter 5 (Paper 3):** Ponnusamy, P., Kamila, H., Müller, E., and de Boor, J., *Efficiency as a performance metric for material optimization in thermoelectric generators*. Journal of Physics: Energy (2021).

These papers are presented as Chapters 3, 4 and 5, preceded by an introduction and overview of the thesis (Chapters 1 and 2) and succeeded by discussion (Chapter 6), conclusion (Chapter 7), outlook (Chapter 8) and references for Chapter 1 and 7. Each chapter containing a published paper includes a brief summary on the contents at the beginning.

Each paper is added to the thesis as the final revised submitted version, including its own references and supplementary material if any.

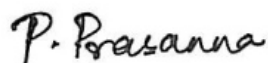
Declaration of Independence
(Versicherung & Selbständigkeitserklärung)

I hereby affirm that I have prepared the submitted thesis independently and without unauthorized outside support. All provided help and supervision are specified in the thesis and/or the acknowledgement, and all data taken from published work is marked as it is. Utilized methods, instruments and experimental setups are also all indicated in the corresponding chapter. Results and data resulting from collaborative work are specified as such, and were utilized with full agreement of the collaborators.

The three papers included in this cumulative thesis as Chapters 3, 4 and 5 were added after knowledge and agreement of all co-authors. An exhaustive list of all co-authors, as well as task distribution, is provided at the end of this manuscript.

Prasanna Ponnusamy

Date: 02-06-2022



Signature:

Acknowledgement

I am grateful and thankful to one and all who made this thesis possible. Doing a PhD thesis abroad alone, especially in a non-English speaking country comes with both positives and negatives. I am glad that I could experience both equally. Especially, if you are sick, it is more than just a normal experience. Thanks to all around me who made this journey possible.

My first and foremost sincere thanks goes to Dr. Johannes de Boor, who is more than just a supervisor, a good scientist as well as a good human and a nice friend. There were unforgettable dramatic incidents, which made me stay strong and stand for myself, which I never thought I would face in my lifetime. For the first time, I learnt how to work under uncomfortable and uncertain situations which life might pose. I highly appreciate his patience with these problems and the ensuing delays. His friendly approach made the whole process comfortable, I cannot thank him enough for that. I completely admire his patience, empathy, hard work and his ability to efficiently manage his work life balance. I wish him and his family the best of everything. I missed our group lunch sessions badly during the pandemic. Many thanks to him for spending memorable time with us in Russia during the conference despite his busy schedule.

I highly value my interactions with Prof. Eckhard Müller who was always available whenever needed. This is very rare to see in a Professor of his rank and status who are normally very busy with a lot of their own work. I was very lucky to have a topic where he is an expert and he never hesitated to give me valuable suggestions and insights. I thoroughly enjoyed his enthusiasm in scientific discussions despite his highly demanding administrative tasks. During the pandemic, I badly missed the 'brain jogging' we used to do together often. Many thanks to all that he has done to me. I will always cherish our time in Korea during ICT 2019.

My sincere thanks goes to Dr. Armin Feldhoff from Universität Hannover for making me a reviewer in journals (as well as thanks to Johannes again for the same reason). My heartfelt thanks goes to Dr. Isabel Kinski from Fraunhofer for nurturing my interest in thermoelectrics when most need and for being a great mentor whenever required, a dear friend and well-wisher, and to my Master thesis supervisors Dr. Hans Peter Martin, Dr. Bing Feng and Dr. Sybrand van der Zwaag for their encouragement and appreciation all the time. Their words often echo in my head during tough times

and keep me going. I also thank Dr. Alexandra Zevalkink for her kindness, patience and guidance with my career choice whenever needed.

I would like to thank my dear friends here who were like family away from my family: especially Sahar and Peter Philipp Bauer, who made my local travel very comfortable during the pandemic and for having so many bubble tea sessions together. My special thanks go to my dear colleague and officemate Sahar Ayachi, with whom I shared a close bond from the moment I met her. I am very grateful for all the love she showered on me. Given that I am less emotional in general, she bore all the emotions on my behalf whenever I had a crisis and made sure to take me out from my 'Corona castle' (my room) at regular intervals to keep me sane. I wish her all the best for her future endeavours. Peter has been very helpful towards the end especially, and made me feel at home in Germany, dedicating his time and presence. I wish him all the good for his kind and extremely helpful heart. I am specially thankful to my ideal friend Harshita, who fed me almost all day during the last one year, and for our very long and deep conversations, sharing our interests in science, music, life, philosophy, human behavior and so on. That 5 mins will hopefully last longer, a bond which will never break. I should specifically thank Aryan for dedicating a great deal of his time and efforts in sending me ample opportunities to apply for my post doc and encouraging me to apply at the right places, despite his busy schedule. Mila has been very loving, kind and supportive during times of crisis, whenever we needed her, she was our home, providing us love, food and support, thanks a lot to Mila, 'we all were in this together as always'. I wish Mila and Reza a lovely family soon! I highly value my dear friends Gustavo and Julia (and Louis) and our were wolf sessions, crane sessions together. We were a family! I thank Mohammad Yasseri for our coffee sessions together, sharing our worries and for his wise words of advice at appropriate times. I cannot thank my dear friends enough for being there for me anytime, loving me, supporting me and inspiring me to be who I am: Pugazh, Leroy, Neola and Shikar, Shruthi, Priya Periyasamy, Chetan and Sri, Shreyas, Vishnu Budama, Nikhil, Gautami, Vijey Subramani, Ramakrishnan, Dr. D.K. Misra (who shockingly succumbed to covid), Nader, Ngan, Silvana, Shalini, Radhika, Kunal Mitra, Sreejha, Preetha, Swathi and Alessio, Akilan, Bharath, my badminton friends Alex, Marcel and my Airbnb friends, especially Milu aunty from Portugal, Mrs. Teresa and Uncle Andrew from Poland, Dr. Susan Crawford from Ireland, Valerija and Dr. Oleg Poljakov from Lithuania, Kirsten from Scotland and many others, and my previous colleague and dear friend Dr. Anke Triebert and her lovely

family, my flatmates Bill, Mike, Martin, Yassin, Aldo, my Bachelor's professor Rathinasamy Dhanraj, Agila akka from Chennai Chef and the list goes on and on, I am sorry if I have missed any of you but you know that you all mean a lot to me, despite if I mention or not.

My biggest thanks go my panacea Richard P Feynman whose books serve as my all-time companion, and to all the beautiful places I travelled to and the wonderful people I met.

Throughout my life journey, I am grateful for the love and support of my sisters and brothers, my nieces and nephews and my biggest inspiration, my Mom, my role model. Special thanks to my niece Pooja and my nephew Kavin for their unconditional love and for keeping me engaged with regular video calls. I thank Andreas for introducing me to a new world I didn't know before and for making me feel special, as well as for his help with translating my abstract. His kindness, wit and open-mindedness are highly admirable.

Last but not the least, I would like to thank myself for not giving up and staying strong despite odds, all thanks to my Mom for making me who I am. I thank DAAD for the scholarship and the support with health insurance.

To all those who had to lose their loved ones to this cruel pandemic, I wish you great strength and courage to deal with the loss and hope for a better future. To those who suffer from pain, I wish you all the strength to bear and heal.

I would also like to acknowledge the fact that the work involved in a PhD is not the one that makes PhD journey a struggle. But being too self-critical, long waits and frustration and the situation around us in general are the ones that might make the journey look strenuous. I cannot stress enough how important it is to find a good, supporting and motivating supervisor who can turn your weaknesses into strengths, not otherwise, or, at least someone, who will not demotivate you for the rest of your life: science needs more people.

Thank you all for being with me. For someone who spent her early years jumping around trees as I could not afford to go to a proper school, a PhD might be sound like a dream come true. But I see this as just the beginning of a journey long awaited.

Short Summary

A thermoelectric generator (TEG) consists of a series of p-n semiconductor leg pairs electrically connected in series and thermally in parallel, and converts thermal energy to electrical energy, serving as a potential solution to meet increasing energy demands by harvesting energy from waste heat. Accurate performance analysis of TEGs requires solving the Domenicali's thermoelectric heat balance equation, which is a second order nonlinear partial differential equation with non-constant coefficients, numerically solvable by Finite Element Methods (FEM). Since FEM is costly and time consuming, an approximate model assuming constant material properties suggested by Ioffe is widely used. However, the thermoelectric (TE) material properties are temperature (T) dependent in general, and the Constant Properties Model (CPM) can yield meaningful estimates only if the constant values (obtained by averaging the T dependent data) are physically appropriate. The question of the effect of selecting an appropriate averaging method has not been exhaustively discussed yet. Additionally, the magnitude of remaining uncertainty when using CPM for TEG performance calculations has not been of much focus in the TE literature. Therefore, this thesis deals with this aspect in larger detail at various levels, focussing on the device aspect but also linking module to material optimization.

Initially, by comparing different averaging modes we demonstrate that a combination of integral averaging over the temperature scale for the Seebeck coefficient and spatial averages (integration over length) for the electrical and thermal resistivities proves to be the best to represent the constant property values. We show that the still remaining deviation due to uncompensated Thomson heat can be corrected using a simple entropy flow diagram. Further, using a material-device model developed in-house, we not only show that the material figure of merit zT , based on CPM, can be misleading in the search for optimum material parameters (such as carrier concentration), but we also demonstrate the usefulness of this tool in studies such as functional material grading.

In summary, this research work provides useful insights about the usage of CPM which is most commonly used in thermoelectrics, clarifying wide spread misconceptions, as well as providing faster and efficient tools for performance calculation and for accurate material optimization.

Kurze Zusammenfassung

Ein thermoelektrischer Generator (TEG) besteht aus einer Reihe von p-n-Halbleiterschlenkelpaaren, welche elektrisch in Reihe und thermisch parallel geschaltet sind und die thermische Energie in elektrische Energie umwandeln. Sie sind eine potenzielle Lösung zur Deckung des steigenden Energiebedarfs, da sie Energie aus Abwärme gewinnen können. Eine genaue Leistungsanalyse von TEGs erfordert die Lösung der thermoelektrischen Wärmebilanzgleichung von Domenicali: einer nichtlinearen partiellen Differentialgleichung zweiter Ordnung mit nicht konstanten Koeffizienten, die numerisch durch Finite-Elemente-Methoden (FEM) gelöst werden kann. Da die FEM kostspielig und zeitaufwendig ist, wird häufig ein von Ioffe vorgeschlagenes Näherungsmodell mit konstanten Materialeigenschaften verwendet. Die thermoelektrischen (TE) Materialeigenschaften sind jedoch im Allgemeinen temperaturabhängig (T), und das Modell der konstanten Eigenschaften (constant property modell - CPM) kann nur dann aussagekräftige Schätzungen liefern, wenn die konstanten Werte (die durch Mittelwertbildung der T-abhängigen Eigenschaften ermittelt werden) physikalisch angemessen wurden. Die Frage, wie sich die Wahl einer geeigneten Mittelungsmethode auswirkt, ist noch nicht vollständig erörtert worden. Darüber hinaus wurde das Ausmaß der verbleibenden Unsicherheit bei der Verwendung von CPM für TEG-Leistungsberechnungen in der TE-Literatur nicht abschließend diskutiert. Daher wird dieser Aspekt in dieser Arbeit auf verschiedenen Ebenen ausführlicher behandelt, wobei der Schwerpunkt auf dem Geräteaspekt liegt, aber auch eine Verbindung zwischen Modul und Materialoptimierung hergestellt wird.

Zunächst zeigt ein Vergleich verschiedener Mittelungsmodi, dass sich eine Kombination aus integraler Mittelung über die Temperaturskala für den Seebeck-Koeffizienten und räumlichen Mittelungen (Integration über die Länge) für den elektrischen und thermischen Widerstand als am besten geeignet erweist, um die konstanten Eigenschaftswerte darzustellen. Wir zeigen, dass die noch verbleibende Abweichung aufgrund der nicht kompensierten Thomson-Wärme durch ein einfaches Entropieflussdiagramm korrigiert werden kann. Darüber hinaus zeigen wir anhand eines selbst entwickelten Material-Bauteil-Modells nicht nur, dass die auf CPM basierende Materialkennzahl zT bei der Suche nach optimalen Materialparametern (wie z. B. der

Ladungsträgerkonzentration) irreführend sein kann, sondern wir demonstrieren auch die Nützlichkeit der entwickelten Methodik bei weitergehenden Studien wie der Materialoptimierung durch Gradierung.

Zusammenfassend lässt sich sagen, dass diese Forschungsarbeit nützliche Einblicke in die Verwendung des CPM liefert, welches in der Thermoelektrik am häufigsten verwendet wird, weit verbreitete Missverständnisse ausräumt und schnellere und effizientere Werkzeuge für die Leistungsberechnung und die genaue Materialoptimierung bereitstellt.

Abstract

A thermoelectric generator (TEG) converts thermal energy to electrical energy, serving as a potential energy solution to meet increasing energy demands by harvesting energy from waste heat. A typical TEG consists of a series of p-n semiconductor leg pairs connected electrically in series and thermally in parallel. Accurate performance analysis of TEGs requires solving the Domenicali's thermoelectric heat balance equation, which is a second order nonlinear partial differential equation with non-constant coefficients, numerically solvable by Finite Element Methods (FEM). Since FEM is costly and time consuming, an approximate model assuming constant material properties suggested by Ioffe is widely used. However, the thermoelectric (TE) material properties are temperature (T) dependent in general, and the Constant Properties Model (CPM) can yield meaningful estimates only if the constant values (obtained by averaging the T dependent data) are physically appropriate. The question of the effect of selecting an appropriate averaging method has not been exhaustively discussed yet. Additionally, the magnitude of remaining uncertainty when using CPM for TEG performance calculations has not been of much focus in the TE literature. Therefore, this thesis deals with this aspect in larger detail at various levels, focussing on the device aspect but also linking module to material optimization.

Initially, a comparison of different averaging modes shows that a combination of integral averaging over the temperature scale for the Seebeck coefficient and spatial averages (integration over length) for the electrical and thermal resistivities ($\frac{1}{\sigma}$ and $\frac{1}{\kappa}$ respectively) proves to be the best to represent the constant property values. However, averaging spatially requires the exact temperature distribution along the length of the thermoelectric leg (temperature profile $T(x)$). Therefore, a fast and easy way of obtaining the axial T profile of a TE leg in a one-dimensional (1D) approach using simple integration is introduced in this study. The solution is obtained by finding $T(x)$ iteratively, starting with a linear $T(x)$ and converging quickly. With this tool, not only the calculation speed is reduced by orders of magnitude compared to 3D FEM, but also the physical origin of the non-linearity of the T profile, its relevance and magnitude can be visualised by separately plotting the individual contributions to the bending of the temperature profile. The heat balance equation consists of contributions from Fourier heat (due to the temperature difference between hot and cold sides),

Joule (due to internal electrical resistance) and Thomson heat (due to the T dependence of Seebeck coefficient). On analyzing the temperature profiles for six highly efficient and widely studied thermoelectric materials, we find that the pronounced temperature dependence of the thermal conductivity (κ) significantly contributes to the deflection of real temperature profiles from a linear one. It is found that the asymmetry in heat distribution (with respect to conduction and internal sources) is important to consider and hence, a simple temperature average which is often used for κ in CPM won't be sufficient to appropriately represent $\kappa(T)$. This is because temperature averages cannot represent spatial variation of the material properties.

Another explicit source of error in the CPM is the Thomson heat as CPM considers a constant Seebeck coefficient (α). One of the most common assumptions is that Thomson heat is quite negligible and hence, can be ignored. However, despite utilizing physically appropriate averages, we find that CPM overestimates performance for many materials (e.g., for PbTe by up to 6%). On analyzing by means of an entropy flow diagram based on the $\alpha(T)$ plot, we show that this remaining deviation occurs to a large extent due to uncompensated Thomson heat, leading to a discrepancy in the estimation of the inflowing heat, the optimum current and thus of the efficiency as calculated in the CPM compared to the real case. The estimate of generated power at maximum efficiency however remains less affected as it is only related to the discrepancy in the optimum current estimation, which is usually $<1\%$. Using the simple entropy flow diagram, we demonstrate how the error in the estimation of Thomson heat at the hot side can be corrected.

One of the major uses of the CPM model in TE material development is to theoretically optimize material properties based on the TE figure of merit zT (defined as $\frac{\alpha^2 \sigma}{\kappa}$). However, the TE material properties α , σ , κ cannot be optimized independently of each other and are directly and partially inversely interrelated. The optimization is typically done by plotting zT vs. carrier concentration (n) or a composition-related parameter (x) or any other parameter that needs to be optimized, for each temperature, and finding the parameter value (e.g., n) corresponding to the maximum of zT . zT as a performance metric is based on an analytical relation for maximum efficiency within the CPM theory. Due to the above-mentioned uncertainties related to CPM, optimized parameters based on zT for a module can be misleading. To test this, a study based on efficiency is conducted on p-type $\text{Mg}_2\text{Si}_{1-x}\text{Sn}_x$ solid solutions which suffers from poorer material properties than its n-type counterpart

and needs optimization of n and x . The 1D iterative solution method for device performance calculation is integrated with an existing electronic band structure-based material model, in this case, a single parabolic band (SPB) model, with an effective mass linearly dependent on composition x and carrier concentration, and acoustic phonon and alloy scattering as charge carrier scattering mechanisms. It is found that for a hot side temperature (T_h) of 500 K (which is well within the validity limits of an SPB model) and a cold side temperature (T_c) of 300 K, the difference in optimum n for $\text{Mg}_2\text{Si}_{1-x}\text{Sn}_x$ calculated once based on leg efficiency using T dependent properties or, on the contrary, based on zT optimization, is found to be about 20%. Additionally, the usage of the temperature average of zT within the CPM formulae for predicting optimum parameters is also analysed and proves to be quite accurate in the determination of n or x , even though the predicted efficiency with the temperature average of zT may be significantly different.

As a further step, in order to demonstrate the utility of this integrated performance estimation tool, a study on the effect of grading and segmentation on Mg_2Sn -based modules is presented. Here, a two-band model developed in the work group is used to describe the properties of n-type Mg_2Sn . A functionally graded leg constructed with locally varying n (optimized based on peak zT vs n) according to linear T variation along the length of the TE leg, amounts to a gain of about 7% in efficiency for $T_h = 700$ K and $T_c = 300$ K. The compatibility criterion is checked, and it is found that this gain is very close to the maximum gain possible with this graded configuration. Additionally, a two-segmented TE leg was studied with $T_h = 700$ K, $T_c = 500$ K for the first half of the leg and $T_h = 500$ K, $T_c = 300$ K for the second half. The optimum (constant) n for these two segments are found using the tool based on device efficiency maximization, to construct the material properties of the two segments. A gain in efficiency of 5% is predicted.

In summary, this research work provides useful insights about the usage of CPM which is most commonly used in thermoelectrics, clarifying wide spread misconceptions, as well as providing faster and more efficient tools for performance calculation and for accurate material optimization.

Table of Contents

Acknowledgement.....	v
Short Summary.....	viii
Kurze Zusammenfassung	ix
Abstract	xi
Table of Contents	xiv
List of Symbols	xvii
List of Acronyms.....	xx
List of Figures	xxii
1 Introduction	1
1.1 Thermoelectric effects	2
1.2 Performance estimation of a 1D TEG element.....	5
1.2.1 Thermoelectric heat balance equation.....	6
1.2.2 Analytical method – Ioffe’s Constant Properties Model (CPM).....	10
1.3 Factors affecting performance of a TEG module	14
1.4 Material aspects of thermoelectric performance.....	16
1.4.1 Optimization of material properties	16
1.4.2 Modelling TE properties using a Single Parabolic Band model	18
1.5 Material grading and segmentation	21
1.5.1 Compatibility.....	23
2 Aim and overview of the thesis.....	27

Paper Catalogue.....	29
3 Using the Constant Properties Model for accurate Performance Estimation of Thermoelectric Generator Elements (Publication 1)	30
3.1 Abstract.....	30
3.2 Introduction	32
3.3 Methods and results	32
3.3.1 Estimation of TE performance by CPM.....	35
3.4 Discussion.....	35
3.4.1 Influence of temperature dependence of material properties	39
3.4.2 Insight into the discrepancy with CPM.....	39
3.5 Conclusion	42
References for chapter 3 (paper 1)	52
4 Discrepancies associated with the use of CPM (Publication 2)	55
4.1 Introduction	56
4.2 Methods, results and discussion	57
4.2.1 Role of the T dependence of material properties in performance estimation	57
4.2.2 Peltier-Thomson heat balance and the resulting uncertainty in CPM efficiency	60
4.2.3 Refining the CPM efficiency estimate	63
4.3 Conclusion	66
Appendix A	68
References for chapter 4 (paper 2):	73
5 Material optimization using exact efficiency (Publication 3)	76
Efficiency as a performance metric for material optimization in thermoelectric generators	76

5.1	Introduction	78
5.2	Method.....	79
5.3	Results	82
5.3.1	Optimum carrier concentration	83
5.4	Discussion.....	85
6	Discussion	98
1.1	Optimum carrier concentration.....	102
1.2	Material grading	102
7	Conclusion and outlook.....	110
	Quantification of asymmetry in heat distribution	112
	Effect of 3D current and heat flow	113
	Effect of scattering mechanisms on temperature dependence and therefore on heat flow	113
8	References	114

List of Symbols

Thermoelectric properties

Symbol	Description	Unit
α	Seebeck coefficient	[V/K]
κ	Thermal conductivity (zero current)	[W/(Km)]
σ	Electrical conductivity (isothermal)	[$(\Omega\text{m})^{-1}$]
ρ	Electrical resistivity, $\rho = \frac{1}{\sigma}$	[Ωm]

Thermoelectric module parameters

Symbol	Description	Unit
T	Temperature	[K]
$T(x)$	Temperature profile	[K]
T_h, T_a	Temperature at hot side / heat absorbing side	[K]
T_c, T_s	Temperature at heat sink side / cold side	[K]
V	Voltage	[V]
V_0	Seebeck Voltage	[V]
τ	Thomson coefficient	[V/K]
Π	Peltier coefficient	[V]
z	Material figure of merit	[K^{-1}]
Z	Device figure of merit	[K^{-1}]
L	Length of TE element	[m]

x	Position along the length of the TE leg	[m]
A	Cross-sectional area of TE element	[m ²]
K	Thermal conductance	[W/K]
R_{in}	Inner electrical resistance	[Ω]
R_L	Load resistance	[Ω]
P, P_{el}	Electrical power	[W]
p	Power output density	[W m ⁻²]
p_v	Power output per volume	[W m ⁻³]
E	Electric Field	[V/m]
η	Efficiency	[-]
I	Electric current	[A]
I_{opt}	Optimum current	[A]
j	Electrical current density	[A/m ²]
\dot{Q}, Q	Heat flow	[W]
\dot{q}, q	Heat flux	[W/m ²]
Q_{in}, Q_h	Heat flow in at the hot side	[W]
Q_{out}, Q_c	Heat flow out at the cold side	[W]
Q_F	Pure Fourier heat flow	[W]
Q_J	Heat flow due to inner Joule heat release	[W]
Q_τ	Heat flow due to Thomson heat	[W]
Q_Π	Peltier heat flow	[W]
\dot{S}	Entropy flow	[W/K]

Material parameters:

Symbol	Description	Unit
μ	Charge carrier mobility	$[\text{m}^2 \text{V}^{-1} \text{s}^{-1}]$
κ_L	Lattice thermal conductivity	$[\text{W K}^{-1} \text{m}^{-1}]$
κ_e	Electronic thermal conductivity	$[\text{W K}^{-1} \text{m}^{-1}]$
n	Electron concentration	$[\text{m}^{-3}]$
p	Charge Carrier Concentration of holes	$[\text{m}^{-3}]$
m_S^*	Single valley effective mass	$[\text{kg}]$
m^*_D	Density of states effective mass	$[\text{kg}]$
\hbar	Reduced Planck's constant	$[\text{J s}]$
R_H	Hall coefficient	$[\text{m}^3 \text{C}^{-1}]$
η_c	Chemical potential	$[\text{eV}]$
L	Lorentz number	$[\text{V}^2 \text{K}^{-2}]$
k	Electron wave vector	$[\text{m}^{-1}]$
E_g	Band gap	$[\text{eV}]$
q	Electric charge of carrier	$[\text{C}]$
E	Energy	$[\text{eV}]$
E_F	Fermi energy	$[\text{eV}]$
$F_i(\eta_c)$	Fermi integral	-
ρ	Mass density	$[\text{kg m}^{-3}]$
N_V	Valley degeneracy	-
N_0	Atomic density	m^{-3}

λ	Scattering parameter	-
E_{Def}	Deformation potential constant	[eV]
E_{AS}	Alloy scattering parameter	[eV]
v_1	Longitudinal velocity of sound	[m s ⁻¹]
μ_0	Mobility parameter	[m ² V ⁻¹ s ⁻¹]

Fundamental Constants :

Quantity	Symbol	Value
Electronic charge	e	1.6×10^{-19} C
Planck's constant	h	6.62×10^{-34} m ² kg s ⁻¹
Electron rest mass	m_0	9.1×10^{-31} kg
Boltzmann's constant	k_B	8.61×10^{-5} eV K ⁻¹

List of Acronyms

Short form	Expansion
0D	Zero-dimensional
1D	One dimensional
2D	Two dimensional
3D	Three dimensional

RTG	Radioisotope Thermoelectric Generator
NASA	National Aeronautics and Space Administration of the U.S.
TE	Thermoelectric
TEG	Thermoelectric Generator
emf	Electromotive force
FEM	Finite Element Method
FDM	Finite Difference Method
FVM	Finite Volume Method
CPM	Constant Properties Model
SPB	Single Parabolic Band
LCB	Light Conduction Band
HCB	Heavy Conduction Band
AP	Acoustic Phonon
AS	Alloy Scattering
VB	Valence Band
SpAv	Spatial Average
TA_v	Temperature average
MVBT	Mean value at boundary temperatures
IWA_v	Ioffe's weighted average
BC	Boundary Condition

List of Figures

Figure 1-1: Schematic representation of a TEG module consisting of pn leg pairs electrically connected in series and thermally in parallel (reproduced with permission from [25]). 2

Figure 1-2: Thermodiffusion of electrons in an n-type semiconductor due to higher momentum at the hot side compared to the cold side, generating a positive open circuit voltage V_o . Here, T_h and T_c indicate hot side and cold side temperature respectively..... 3

Figure 1-3: Schematic explaining the Peltier effect at a metal-semiconductor junction. As electrons move through the circuit (indicated by arrow direction), they gain energy when travelling from a metal in which carriers move at an average lower energy level ($\approx EF_1$) to a semiconductor of higher energy E (n-type) cooling that side, and lose energy in the form of heat on the other side when dropping down to a metal again. The second metal contact here has a lower Fermi energy (EF_2) due to the application of voltage V . When the direction of flow of current is reversed, the effect is reversed. 4

Figure 1-4: Schematic of an n-type TE leg of length L with hot side temperature (T_h) and cold side temperature (T_c) connected to an external load resistor RL . I indicates the current. The graph above the leg shows the temperature variation along the length of the TE leg (T profile): the solid curved line shows the actual T profile due to Thomson and Joule effects and the temperature dependence of the thermal conductivity. It can either be above or below the linear T profile (dotted line) depending on the material properties. On the right, an equivalent electrical circuit indicating the involved resistances and voltage is presented. 5

Figure 1-5: a) A meshed TEG leg. The colour variations indicate the temperature variation with red being hot and blue being cold. A schematic of a sample T profile is shown above the leg. b) the list of available toolboxes in workbench showing Thermal-Electric toolbox and the steps involved in the FEM analysis can be seen. 9

Figure 1-6: Thermoelectric solver interface showing the boundary conditions (temperature, voltage and current) on the left side pane and the simulated single TE leg on the right-side workspace. The blue arrow on the rectangular TE leg indicates the direction of current flow..... 10

Figure 1-7: a) Schematic of a p-n leg pair connected to an external load resistor RL . The heat flow direction for a leg is shown on the right. As current I flows through the TE leg, Joule heat QJ , and Peltier heat $Q\pi$, are generated. Fourier heat $Q\kappa$ flows due to the supplied temperature difference, b) Schematic representation of heat transfer and electrical power production in a single leg. Here, $Q_{in} \leftrightarrow Q_h$, $Q_{out} \leftrightarrow Q_c$, $R_{in} \leftrightarrow R$ and $P_{el} \leftrightarrow P$ are equivalently used (taken from [28])...... 11

Figure 1-8: Electric power density p_{out} vs. j a) for different zT_m ($Th = 600 K$) b) for different Th ($zT_m = 1$); TEG efficiency η vs. j characteristics c) for different zT_m ($Th = 600 K$) d) for different Th ($zT_m = 1$), calculated for a typical TE material (taken from [28]). The larger black dotted lines represent points of maximum power or efficiency accordingly and dotted and dashed lines to serve as eye guide for primary and secondary points of maximum. For example, in a) the dashed lines with bigger solid dots represent points of P_{max} and dotted lines and small dots represent points of η_{max} . Here, $T_c = 300 K$, $\alpha = 180 \mu V/K$, and $\kappa = 1.5 W/m K$ 13

Figure 1-9: Power output density (P/NA) characteristics (left y-axis) and conversion efficiency (right y-axis) for different ΔT for a commercial TE material with thermal and electrical contact resistances (taken from [18]). Here, N indicates the number of pn leg pairs and A is the cross-sectional area of the pn couple, $n = 0.05 m$ and $r = 5$ 16

Figure 1-10: Typical variation of TE material properties α, σ and κ and zT vs free carrier concentration for parameters corresponding to a typical TE material [25]...... 18

Figure 1-11: a) Single Parabolic Band approximation to $Mg_2Si_{0.3}Sn_{0.7}$ solid solution [90]. Here, the combination of a light conduction band (LCB) and a heavy conduction band (HCB) are approximated to a single parabolic band. b) Electronic band structure of $Mg_2Si_{0.6}Sb_{0.4}$ where the Fermi level is indicated by the horizontal line [91]. The x-axis indicates different points in the Brillouin zone. At the X point (highlighted in green), the two converging conduction bands that contribute to conduction can be approximated by an SPB..... 19

Figure 1-12: Modelling zT using SPB model, zT variation with composition and carrier concentration in p- $Mg_2Si_{1-x}Sn_x$ at 500 K [95]. 21

Figure 1-13: Concept of material segmentation depicted using three materials Bi_2Te_3 , $PbTe$ and $SiGe$ which have their zT_{max} at different temperatures of about 400 K, 650 K and 1190 K

respectively. A TE leg made of these materials together as depicted in the figure, operating between a $T_h = 1200$ K and $T_c = 300$ K might be expected to have a higher overall efficiency as each material is operating near its zT_{max} [23]...... 22

Figure 1-14: A segmented leg in 1D maintained between temperatures T_a at $x = 0$ and T_s at $x = L$ with current density j flowing through it [28]...... 23

Figure 3-1: Schematic showing a TE leg connected in a circuit to an external load resistor. At open loop ($j = 0$), only Fourier heat is flowing whereas in non-zero current case additionally Joule, Peltier and Thomson heat are involved (j – current density)...... 32

Figure 3-2: Graphical representation of different averages along with the T -dependent material data for a) n-type $Mg_2(Si,Sn)$ [34] and b) p-type $Mg_2(Si,Sn)$ [35]. The legend for all the graphs is given on the top left diagram. $T_c = 383$ K and $T_h = 723$ K..... 37

Figure 3-3: Comparison of maximum efficiency calculated using different averages in CPM formulation (Eq.(46)): a) FMT, MVBT, T_{Av} , IW_{Av} and $(zT)T_{Av}$ and b) Sp_{Av} for resistivities and T_{Av} for Seebeck coefficient, as a comparison with FEM results for six representative TE materials. 39

Figure 3-4: a) Temperature profiles and the corresponding variation of the TE properties b) Thermal conductivity c) Electrical resistivity d) Seebeck coefficient, along the TE leg for p-type Bi_2Te_3 . Spatial averages for the resistivities and temperature average for the Seebeck coefficient are shown as horizontal dashed lines..... 40

Figure 3-5: Partial contributions to the bending of the temperature profile for p-type Bi_2Te_3 . $\Delta T_{\kappa T}(x)$, $\Delta T_{\tau}(x)$ and $\Delta T_{J}x$ indicate the contributions due to the T dependence of the thermal conductivity, Thomson heat and Joule heat, respectively. For better readability, the linear part of the temperature profile has been subtracted here. 41

Figure 3-6: Linear, CPM and the actual temperature profiles for p-type Bi_2Te_3 at optimum current. 42

Figure 3-7: Normalised temperature profiles omitting the linear part ($Tx - Tlin$) at zero current for Bi_2Te_3 , $SnSe$, p-type $Mg_2(Si,Sn)$, Mg_2Si , n-type $Mg_2(Si,Sn)$ and HMS..... 45

Figure 4-1: a) Comparison of the relative deviation of the calculated maximum efficiency of 2TD model materials (one of the TE properties kept constant,) from their real counterpart for the example materials, b) T profile bending caused by Joule heat for example materials. Distinct asymmetry is observed particularly for PbTe and SnSe, correlated to maximum offset values in the middle part of Fig a). 59

Figure 4-2: a) Bending of T profiles for the real materials at $j = 0$ (dotted lines) and $j = j_{opt}$ (solid lines), normalized to ΔT , b) T profile bending for the 1TD and 2TD model materials in comparison to the full T dependent case and the CPM case, along with the individual contributions to the fully T dependent profile for a n-Mg₂(Si,Sn) TE leg with $T_h = 723$ K and $T_c = 383$ K. 59

Figure 4-3: Schematic representation of reversible heat exchange in a TE leg for a linear $\alpha(T)$ curve (black line) in a plot of the convective 1D entropy flow with a constant current I . According to the relation $Q\pi = I\alpha T$ areas in the $S(T)$ diagram represent certain amounts of (flowing or exchanged) Peltier (including Thomson) heat. The dark blue and light blue rectangles – in- and outflowing Peltier heat; trapezium above the $S(T)$ curve – Thomson heat (marked with slant lines); trapezium below the $S(T)$ curve (marked in checked lines) – gross electrical power generated (VoI); red trapezium – Thomson heat flowing to the hot side; orange rectangle – hot side Peltier heat (CPM). The green triangle indicates part of the difference amount of absorbed Peltier heat at the hot-side between the actual and the CPM cases) that is not compensated in the real material by backflowing Thomson heat $Q\tau, h$ 61

Figure 4-4: Calculated relative deviation (RD) of a) the maximum efficiency, $\delta\eta_{max}$, heat input, δQ_{in} , power at maximum efficiency, $\delta P\eta_{max}$, and optimum current, $\delta I_{opt, \eta}$; additionally, δQ_{in} when neglecting $\delta I_{opt, \eta}$ (black stars), b) Joule heat, $\delta Q_{\pi th}$, reversible heat, δQ_{Jh} (see Eq. (12)) and, for direct comparison, also $dQ_{Jh}/Q_{\pi th}$ 63

Figure 4-5: Plot of the convective 1D entropy flow at constant current I for a) PbTe and b) SnSe. Relevant areas are marked to determine the uncompensated Peltier-Thomson heat $dQ_{\pi th}$ (green area). Note that the $L2$ temperature and the temperature $T_{\tau, ex}$ according to the extremum of $\Delta T_{Thomsonx}$ may be located quite apart (b) whereas $T_{\tau, ex}$ is very close to the crossing point of αT to α 65

Figure 4-6: RD in maximum efficiency, $\delta\eta_{\max\text{corr}}$, corrected with respect to $dQ_{\pi\tau h}, I = \text{const}$ ($T\tau, \text{ex}$ according to the peak of the exact Thomson profile; blue), $dQ_{\pi\tau h}$ (exact numerical calculation; red; cmp. also Eq. 12) and a first guess by the **L2** position..... 65

Figure 5-1: Comparison of the interpolated experimental figure of merit and the figure of merit calculated by the SPB model for different carrier concentrations $n=1.51, 2.47,$ and $2.68 \times 10^{20} [\text{cm}^{-3}]$ in p-type Mg_2Sn . The temperature corresponding to the peak (marked) of the experimental zT curves is taken as the validity limit of the SPB model..... 81

Figure 5-2: Contour plot indicating the temperatures up to which the SPB was applied as function of x and carrier concentration n for p-type $\text{Mg}_2\text{Si}_{1-x}\text{Sn}_x$ 83

Figure 5-3: a) Maximum calculated efficiency for $T_h = 500 \text{ K}$ and $T_c = 300 \text{ K}$; b) zT at 500 K; c) zT_{TAV} for $T_h = 500 \text{ K}$ and $T_c = 300 \text{ K}$, for different n and x for p-type $\text{Mg}_2\text{Si}_{1-x}\text{Sn}_x$; the SPB approximation does not hold in the shaded region on the graphs as discussed by Fig 2. d) optimum n with respect to the calculated maximum efficiency ($x = 0.64$), zT_{\max} ($x = 0.65$), and zT_{TAV} ($x = 0.64$), all curves normalized to their maximum values. 84

Figure 5-4: Calculated maximum efficiency contours for a cold side temperature of $T_c = 300 \text{ K}$ and hot side temperature T_h of 610 K with the black line showing the validity limit of the SPB model. With increasing distance from the black line into the dimmed region the predicted efficiency is increasingly overestimated as the (detrimental) influence of the minority carriers is not taken into account by the employed SPB model..... 86

Figure 5-5: a) Change in optimum carrier density n and b) optimum composition x , estimated using $zT_{\max}, zT_{\text{TAV}}$ and exact efficiency. 86

Figure 6-1: T profile bending beyond linearity for graded and homogenous material. Since the maximum possible deviation is only about 22 K, the $n_{\text{opt}}(T)$ was found simply for a linear T profile instead of iterating the procedure with the actual T profile. It should also be pointed out that for the considered case the $T(x)$ of the graded sample is more linear than that of the optimum homogeneous material..... 100

Figure 6-2: a) Schematic of a TE leg connected to an external load resistor R_L with an applied temperature difference $\Delta T = T_h - T_c$. Taking the shown linear $T(x)$ as a starting point, the $n(x)$

for a graded sample is chosen according to the $\mathbf{nopt}, \mathbf{zT}$ (optimum \mathbf{n} based on $\mathbf{zT}_{\max, n}$). For segmentation, $\mathbf{nopt}, \boldsymbol{\eta}$ for each section i (e.g., $T_{h,s1}=700\text{K}-T_{c,s1}=T_{h,s2}=600\text{K}$ and so on) is used, b) Optimum \mathbf{n} according to \mathbf{zT} ($\mathbf{nopt}, \mathbf{zT}$) is found for each T and the properties corresponding to $\mathbf{nopt}, \mathbf{zTT}$ are set at each temperature point, dashed vertical lines indicate the corresponding optimum \mathbf{n} 101

Figure 6-3: Optimum \mathbf{n} according to different optimization parameters: $\mathbf{nopt}, \mathbf{zTT}, \mathbf{nopt}, \boldsymbol{\eta}(Th = T, Tc)$ and $\mathbf{nopt}, \mathbf{zTTAv}(Th = T, Tc)$ (for $T_c = 300\text{K}$). 102

Figure 6-4: a) Seebeck coefficient; b) electrical conductivity; c) thermal conductivity and d) \mathbf{zT} , for a graded material with $\mathbf{nopt}, \mathbf{zT}(T)$ and the homogenous material with the optimum constant \mathbf{n} for the full T range based on efficiency. The material properties of the graded material are obtained at each T from the $\mathbf{nopt}, \mathbf{zT}$ at that T 103

Figure 6-5: a) Variation of \mathbf{u} and \mathbf{s} with T for the graded and homogenous material. Maximum $\boldsymbol{\eta}_r$ is obtained locally when $\mathbf{u} = \mathbf{s}$. b) Actual $\boldsymbol{\eta}_r$ and maximum $\boldsymbol{\eta}_r$ for the graded and homogenous material. It can be seen that at higher temperatures, actual $\boldsymbol{\eta}_r$ is quite deviant from maximum $\boldsymbol{\eta}_r$ for homogenous material. 105

Figure 6-6: Material properties of segmented Mg_2Sn leg a) Seebeck coefficient b) Electrical conductivity c) Thermal conductivity d) \mathbf{zT} . For the segment 700 K-500 K $\mathbf{n} = 2.27 \times 10^{20} \text{cm}^{-3}$ and for the second segment 500 K-300 K $\mathbf{n} = 9.87 \times 10^{19} \text{cm}^{-3}$, e) \mathbf{u} and \mathbf{s} e) Actual $\boldsymbol{\eta}_r$ and maximum $\boldsymbol{\eta}_r$ 106

Figure 6-7: a) $\mathbf{nopt}, \mathbf{zTT}(\mathbf{x})$ where $T(\mathbf{x})$ is the temperature profile of the graded material (red curve in b)Figure 6-7) formed assuming a linear $T(\mathbf{x})$. The temperature profile of the graded material obtained after setting the $\mathbf{nopt}, \mathbf{zTT}(\mathbf{x})$ according to the red curve. The red and black curves (with square symbols) coincide as can be seen. 109

1 Introduction

The importance of thermoelectric (TE) power generation can be seen from a long series of successful U.S. and Russian deep-space and rover missions up to the recent (2020) success of NASA's (National Aeronautics and Space Administration) Perseverance rover operating on Mars, including the farthest manmade objects in space (Voyager 1 and 2) that are still sending us deep space data for more than 40 years [1-6]. Since solar power is not always available in such missions these probes are powered by what is called Radioisotope Thermoelectric Generators (RTG). RTGs use the decay heat from radioactive isotopes such as plutonium and convert it to electric power for mission supply. Thermoelectric energy harvesting has gained interest in the recent years, due to rapid advancements in materials research, as well as due to the ongoing energy crisis [7-10]. The need for alternative and sustainable sources of energy is on the rise as fossil fuels are depleting quickly [11]. It is also well known that about 60% of usable primary energy is being wasted in the form of heat, such as loss in the intermediate processes in the conversion from fuel to electricity, waste heat from industries, engine exhausts and other sources [12-14]. Thermoelectricity helps to harvest such wasted energy and serves as a silent, pollution-free, reliable, maintenance-free, long lasting, direct form of energy conversion [15-18].

'Thermo'electricity as the name implies is the reversible conversion of thermal energy into electrical energy or vice versa [17]. Conversion of heat flow (due to an applied temperature difference) into electrical power is the power generation mode and this can have potential for waste heat scavenging [14], self-powering sensors [19, 20] and many applications more [15, 21-24]. A thermoelectric generator (TEG) is a device made of a number of leg pairs made of *p*- and *n*-type semiconductor material, electrically connected in series and thermally in parallel. A schematic of a typical TEG module is shown in Figure 1-1, where a number of pn leg pairs can be seen between electrically insulating ceramic plates.

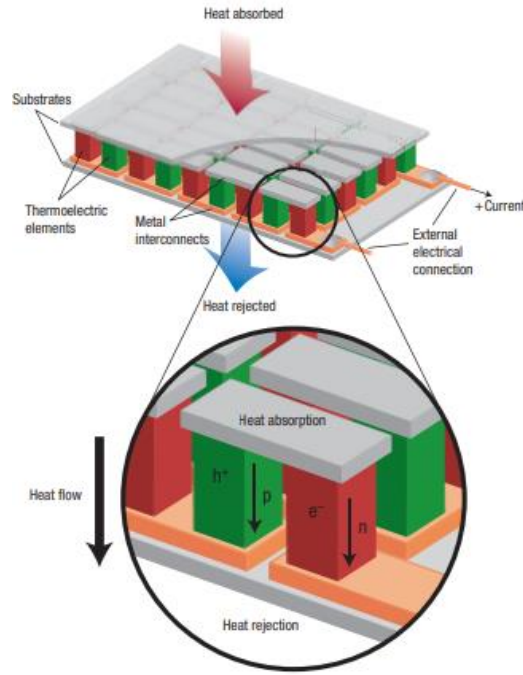


Figure 1-1: Schematic representation of a TEG module consisting of pn leg pairs electrically connected in series and thermally in parallel (reproduced with permission from [25]).

1.1 Thermoelectric effects

Generation of a voltage due to a temperature difference is called the Seebeck effect [26], which is the phenomenon that the charge carriers (holes/electrons) which have higher kinetic energy at the hot side (h) move to the cold side (c), resulting in an accumulation of charge on one side compared to the other. This results in a potential difference between the hot and cold sides, giving rise to an electromotive force (emf) [27]. The material property which quantifies this behavior is called Seebeck coefficient (α). It is simply the amount of voltage generated due to a given temperature difference ($\Delta T = T_h - T_c$). A simple schematic explaining the mechanism of the Seebeck effect in an n-type TEG leg is shown in Figure 1-2. Assuming that only one type of carrier exists in this leg (electrons here), an equivalent electron gas model can be considered [28]. A gradient in charge carrier concentration n can be seen throughout the leg and here for simplicity, the accumulation of electrons only at the ends is shown. The open circuit voltage (V_o) generated due to a given temperature difference is given by,

$$V_o = -\alpha\Delta T \quad (1)$$

The negative sign is due to the fact that the direction of the Seebeck voltage generated is against the direction of the temperature gradient. For example, the Seebeck coefficient of an n-type semiconductor is negative and it creates a positive potential at the hot side compared to the cold side, while a p-type material (positive α) creates a negative potential at the hot side.

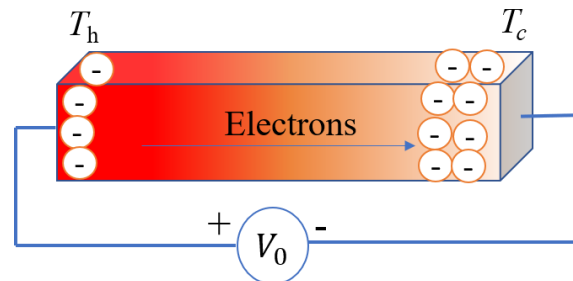


Figure 1-2: Thermodiffusion of electrons in an n-type semiconductor due to higher momentum at the hot side compared to the cold side, generating a positive open circuit voltage V_0 . Here, T_h and T_c indicate hot side and cold side temperature respectively.

The reverse effect, that when an electric current is passed through a thermoelectric material, heat is absorbed at one side and released at the other side, is called Peltier effect and can be used for cooling/heating applications and small-scale heat pumps such as portable refrigerators [29-33], vaccine transportation boxes, car seat heating/cooling etc. [34, 35]. The Peltier effect at a metal-semiconductor junction is represented by a simple schematic in Figure 1-3 [36]. By applying a voltage difference, the electrons are forced to move between these two materials (A and B) having different Seebeck coefficients (and therefore having different average energy levels at which the carriers move). The electrons have to gain energy to jump from metal in which carriers move at the average energy level E_{F1} to semiconductor of average energy E (when $E > E_{F1}$ as for n-type semiconductor) by absorbing heat, and therefore cooling the environment at this side and leave the semiconductor of energy E to a metal at lower energy level E_{F2} , releasing the heat (warming). Here, qV represents the difference in the Fermi level between the two contacts due to the application of voltage V . The dotted sloping line inside the semiconductor represents the decreasing electrochemical potential from left to right. A vertical energy axis is shown on the left for reference. The Peltier effect causes the material to serve as a heat pump between two junctions between materials of different Seebeck coefficient [16, 37]. Unlike the irreversible Joule heating effect, the Peltier effect is reversible. When the direction of current is reversed the heating/cooling effect is reversed. The Peltier coefficient Π is given by,

$$\Pi_A - \Pi_B = \frac{Q_\pi}{I} \quad (2)$$

where Q_π is the heat flow absorbed/generated at the contact of two materials A and B when current I flows through the interface. Q and \dot{Q} are equivalently used throughout this thesis to indicate heat flow (\dot{Q} represents heat flow rate conventionally). $\Pi_A - \Pi_B = \Pi_{AB}$ is called the relative Peltier coefficient, while Π_A is called the absolute Peltier coefficient which is just associated with material A . Π is related to the Seebeck coefficient as, $\Pi = \alpha T$ [38]. This is called the first Kelvin's relation [39].

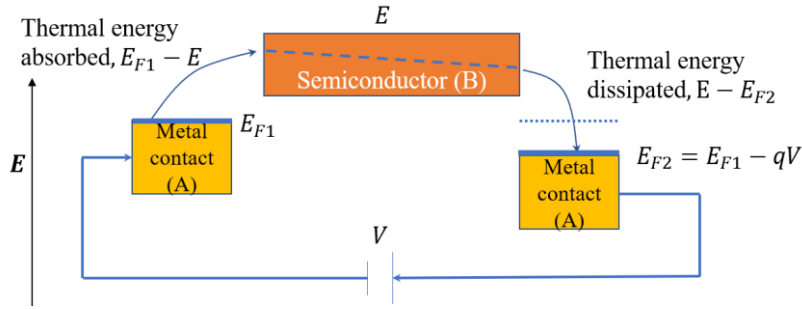


Figure 1-3: Schematic explaining the Peltier effect at a metal-semiconductor junction. As electrons move through the circuit (indicated by arrow direction), they gain energy when travelling from a metal in which carriers move at an average lower energy level ($\approx E_{F1}$) to a semiconductor of higher energy E (n-type) cooling that side, and lose energy in the form of heat on the other side when dropping down to a metal again. The second metal contact here has a lower Fermi energy (E_{F2}) due to the application of voltage V . When the direction of flow of current is reversed, the effect is reversed.

Figure 1-3 depicts an isothermal condition. However, when there is a temperature gradient in the semiconductor, and if the average energy is T dependent, i.e., if the Seebeck coefficient is temperature dependent, then the Peltier effect happens continuously in a TE leg and the related distributed Peltier effect is called the Thomson effect. It is basically the generation or absorption of heat in a current carrying conductor when there is a temperature gradient. It occurs due to temperature dependence of α [38]. The Thomson coefficient τ , is given by

$$\tau = T \frac{d\alpha}{dT} \quad (3)$$

Hence when $\alpha(T)$ is constant, $\tau = 0$. From the above expression (eq. (3)), the heat generated/absorbed is given by,

$$dQ = \tau I \frac{\partial T}{\partial x} dx \quad (4)$$

From the Peltier coefficient ($\Pi = \alpha T$) and Eq. (3), it can be seen that

$$\frac{d\Pi}{dT} = \tau + \alpha \quad (5)$$

This is called the second Kelvin's relation. The majority of this thesis deals with the Peltier-Thomson effect and the widely assumed notion that Thomson heat is quite negligible [40, 41] and is usually ignored. A detailed explanation for the Peltier-Thomson balance and its effect on performance estimation can be found in Chapters 3 and 4.

1.2 Performance estimation of a 1D TEG element

TEG performance estimation involves mainly finding the power output (P) and efficiency (η). This thesis entirely deals with steady state calculations. The effects of convective and radiative heat losses are not considered.

Consider a single TE leg of length L as shown in Figure 1-4, supplied with a constant hot side and cold side temperature.

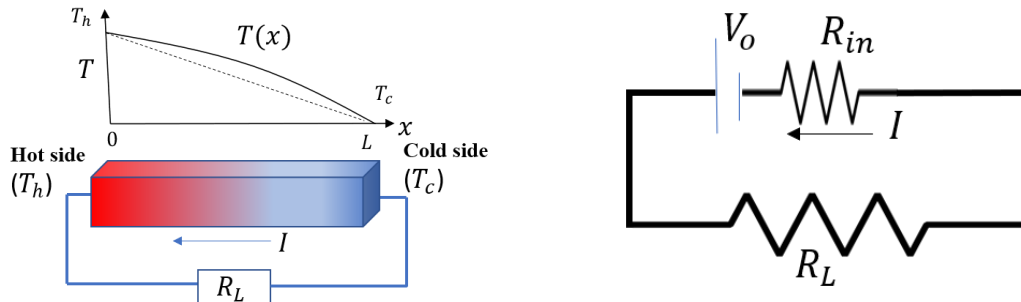


Figure 1-4: Schematic of an n-type TE leg of length L with hot side temperature (T_h) and cold side temperature (T_c) connected to an external load resistor R_L . I indicates the current. The graph above the leg shows the temperature variation along the length of the TE leg (T profile): the solid curved line shows the actual T profile due to Thomson and Joule effects and the temperature dependence of the thermal conductivity. It can either be above or below the linear T profile (dotted line) depending on the material properties. On the right, an equivalent electrical circuit indicating the involved resistances and voltage is presented.

The electrical power output at the load resistor due to a current flow I is given by [18].

$$P = V \cdot I, \text{ where } V = V_o - R_{in}I \quad (6)$$

Here, V is the output voltage measured at the terminals of the TEG leg, V_o is the Seebeck voltage generated (the maximum output voltage, reached at open loop) given by eq. (1), $R_{in}I$

is the voltage drop due to the internal resistance (R_{in}) of the TE material ($R_{in} = \rho L/A$, where ρ is the electrical resistivity of the TE material, L – length, A – cross-sectional area).

Efficiency is given by the ratio of output power to the input heat flow (Q_{in}).

$$\eta = P/Q_{in} \quad (7)$$

Calculation of Q_{in} depends on if the model is considering fully T dependent material properties or if the constant properties model (CPM) is considered. Both models will be discussed in the following sections. While all these equations apply for a single leg, the performance of a TEG module is scaled under ideal conditions (zero contact resistance) by the following considerations given in Table 1, where N is the number of pn pairs.

Table 1: Thermoelectric quantities used in performance estimation of TEG modules (reproduced from [28]).

Entity	Single leg	pn couple	TEG
Seebeck coefficient (α)	α_p, α_n	$\alpha_{pn} = \alpha_p + \alpha_n $	$N \cdot \alpha_{pn}$
Electrical resistance (R)	R_p, R_n	$R_{pn} = R_p + R_n$	$N \cdot R_{pn}$
Thermal conductance $K = (\frac{\kappa A}{L})$, where κ is the thermal conductivity	K_p, K_n	$K_{pn} = K_p + K_n$	$N \cdot K_{pn}$
Voltage	V_p, V_n	$V_{pn} = V_p + V_n$	$N \cdot V_{pn}$
Current	$I_p = I_n$	$I_{pn} = I_p = I_n$	I_{pn}
Heat flow	Q_p, Q_n	$Q_{pn} = Q_p + Q_n$	$N \cdot Q_{pn}$
Electrical Power output	P_p, P_n	$P_{pn} = P_p + P_n$	$N \cdot P_{pn}$
Efficiency	η_p, η_n	$\eta_{pn} = \frac{P_{pn}}{Q_{pn}}$	η_{pn}

1.2.1 Thermoelectric heat balance equation

Domenicali [42] arrived at the thermoelectric heat balance equation considering an isotropic material. This equation is obtained from the fact that the divergence of flowing Fourier heat

equals the sum of the source terms which are the Joule heat and Thomson heat [18]. From the energy conservation, it follows that for an n type leg,

$$\nabla q = p_v \quad (8)$$

Here, p_v is the electrical power produced per volume. Heat flux q and electric field E at any point in the TE leg, following the sign convention in Figure 1-4 is given by

$$E = \alpha \nabla T + \rho j \text{ and } q = -\kappa \frac{\partial T}{\partial x} + \alpha T j \quad (9)$$

where $p_v = Ej$. Hence, substituting eq. (9) in eq. (8), we get

$$\nabla(-\kappa \nabla T + \alpha T j) = p_v \quad (10)$$

Expanding, we get,

$$\nabla(-\kappa \nabla T) + \nabla \alpha \cdot T j + \nabla T \cdot \alpha j + \nabla j \cdot \alpha T = j(\alpha \nabla T + \rho j) \quad (11)$$

Due to charge conservation $\nabla j = 0$ holds. Hence, eq. (11) simplifies to,

$$\nabla(-\kappa \nabla T) + \nabla \alpha \cdot T j = \rho j^2 \quad (12)$$

Expanding $\nabla \alpha \cdot T j$ and recollecting the second Kelvin relation $\Pi = \alpha T$, we get,

$$\nabla \alpha \cdot T j = \nabla \left(\frac{\Pi}{T} \right) \cdot T j = \left(\frac{1}{T} \nabla \Pi - \frac{1}{T^2} \Pi \nabla T \right) \cdot T j = (\nabla \Pi - \alpha \nabla T) \cdot j \quad (13)$$

This again reinforces the fact that Peltier and Thomson effects are different aspects of $\nabla \alpha$. Pictorially this is represented in Figure 4-3 of chapter 4. $\nabla \alpha \cdot T j$ is the Peltier-Thomson term.

From the second Kelvin relation (eq. (5)), and eq.(13), eq. (12) simplifies to

$$\begin{aligned} \nabla(-\kappa \nabla T) + \left(\frac{d\Pi}{dT} \frac{dT}{dx} - \alpha \nabla T \right) \cdot j &= \rho j^2 \cdot \\ \nabla(-\kappa \nabla T) + ((\tau + \alpha) \nabla T - \alpha \nabla T) \cdot j &= \rho j^2 \cdot \end{aligned} \quad (14)$$

Eq. (14) therefore simplifies to the thermoelectric heat balance equation of TE conversion as follows,

$$\nabla(-\kappa \nabla T) + \tau j \cdot \nabla T = \rho j^2 \cdot \quad (15)$$

When incorporating the T dependence of the material properties α , κ and σ , the eq. (15) is a second order non-linear partial differential equation, typically solved using numerical methods like Finite Element Methods (FEM) [28, 43], Finite Volume Methods (FVM) [44-46] or Finite Difference Methods (FDM) [28] and similar numerical tools [47, 48]. Although all three

methods are suitable, in the following section, the basic methodology of FEM is discussed briefly as it was used to validate the solution developed in this thesis (Chapter 3).

At the hot side, the heat flux q_{in} is given according to Fourier's law. In a TE material, Peltier heat is additionally generated and hence q_{in} is given by

$$q_{in} = -\kappa_h \frac{dT}{dx_h} + j\alpha_h T_h. \quad (16)$$

Here, $-\kappa_h \cdot \frac{dT}{dx_h}$ is the Fourier heat flux entering at the hot side and $j \cdot \alpha_h \cdot T_h$ is the absorbed Peltier heat flux at the hot side [27, 28]. Here, $\kappa_h = \kappa(T_h)$ and $\alpha_h = \alpha(T_h)$. To obtain $\frac{dT}{dx}$ for determining q_{in} , the thermoelectric heat balance equation given (in 1D) by eq. (17) is solved for $T(x)$.

$$\kappa(T) \frac{\partial^2 T}{\partial x^2} + \frac{d\kappa}{dT} \left(\frac{\partial T}{\partial x} \right)^2 - jT \frac{d\alpha}{dT} \frac{\partial T}{\partial x} = -\rho(T)j^2 \quad (17)$$

$T(x)$ gives a relation between the Fourier heat flux $(\kappa(T) \frac{\partial^2 T}{\partial x^2} + \frac{d\kappa}{dT} (\frac{\partial T}{\partial x})^2)$, the Joule heat $(\rho(T)j^2)$ and the Thomson heat $(jT \frac{d\alpha}{dT} \frac{\partial T}{\partial x})$, refer eq.

(4) per area. For steady state heat conduction with constant material properties, the temperature profile is linear between the hot and cold sides at $j = 0$. However, in a TE leg, the T profile is slightly bent from linearity due to the contributions from Joule and Thomson heat (at $j \neq 0$) as well as due to the temperature dependence of κ (even under $j = 0$ condition) as shown in the schematic in Figure 1-4. The importance of the T profile and the temperature dependence of material properties is discussed in Chapter 3.

1.2.1.1 Finite Element Method (FEM)

The Finite Element Method is a widely used numerical solution method to solve partial differential equations which can't be solved by simple integration [49-51]. FEM works by discretizing the geometry into finite elements (meshing) and thereby forming nodes. At each node the solution is obtained by simplifying the governing equations (for example, in our case, eq. (17)) to simple algebraic equations and allowing for the solution to converge. In other words, a product of a weighted function and its residual is minimized, where the weighted function is a trial fitting function to the solution and the residual is the remaining deviation involved in these fitting functions. One of the major advantages of FEM is that any geometry

can be solved unlike FDM as FDM uses only rectilinear domains. An inbuilt TE toolbox in ANSYS workbench was used to validate the solution method involved in this thesis (Chapter 3) [52]. A sample TE leg used in the simulation and the toolbox interface is shown in Figure 1-5. A schematic temperature profile is drawn above the simulated TE leg in Figure 1-5a. As can be seen from Figure 1-5b, the thermoelectric material properties are input in the ‘Engineering Data’ (in the sample leg shown in a), T dependent properties are given as input), geometry is created in step 2 (in this case, a rectangular bar) and meshed to created nodes in step 3. The boundary conditions such as temperature difference between the hot and cold sides, voltage and/or current supplied are set up in step 4 [53]. The output variables such as temperature profile, voltage, heat flux at the hot and cold sides (to determine power output and efficiency) are indicated in the solution step. In Figure 1-6, the workbench solution interface is shown. As can be seen, the boundary conditions for the steady state thermoelectric conduction are indicated: hot and cold side temperatures, current flow on one side whereas the other side is electrically grounded. Throughout this work, the sides are assumed to be insulated and the effect of heat loss out of the leg due to convection or radiation is not considered. All the simulation is done in 3D. Even though 3D simulation doesn’t differ from the 1D solution for a single TE leg and symmetric boundary conditions, it becomes inevitable when a π -shaped TE couple is simulated. In this case especially when simulating using electrical and thermal contacts, 3D effects such as distortion of current lines at the edges can become relevant. The solution tab shows the output variables that we require (heat flux at the hot and cold sides and the voltage output generated).

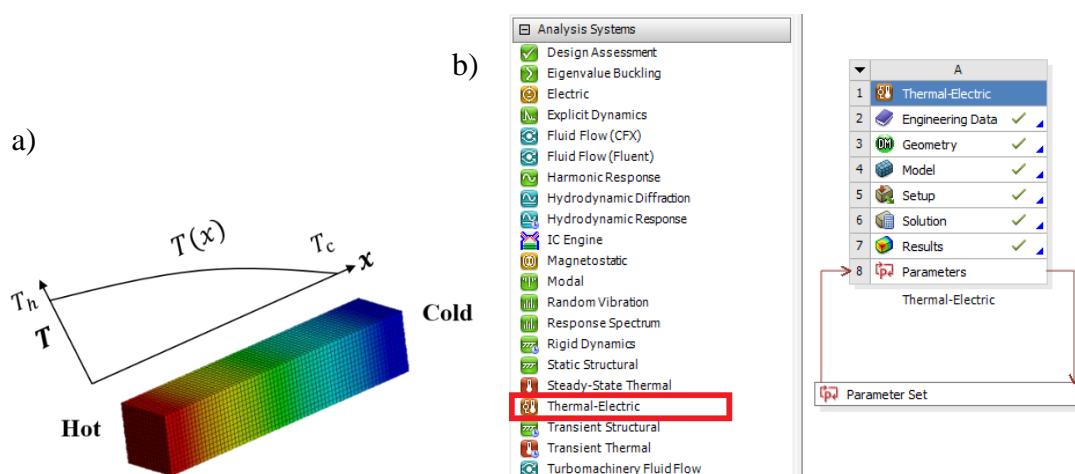


Figure 1-5: a) A meshed TEG leg. The colour variations indicate the temperature variation with red being hot and blue being cold. A schematic of a sample T profile is shown above the leg. b) the list of available

toolboxes in workbench showing Thermal-Electric toolbox and the steps involved in the FEM analysis can be seen.

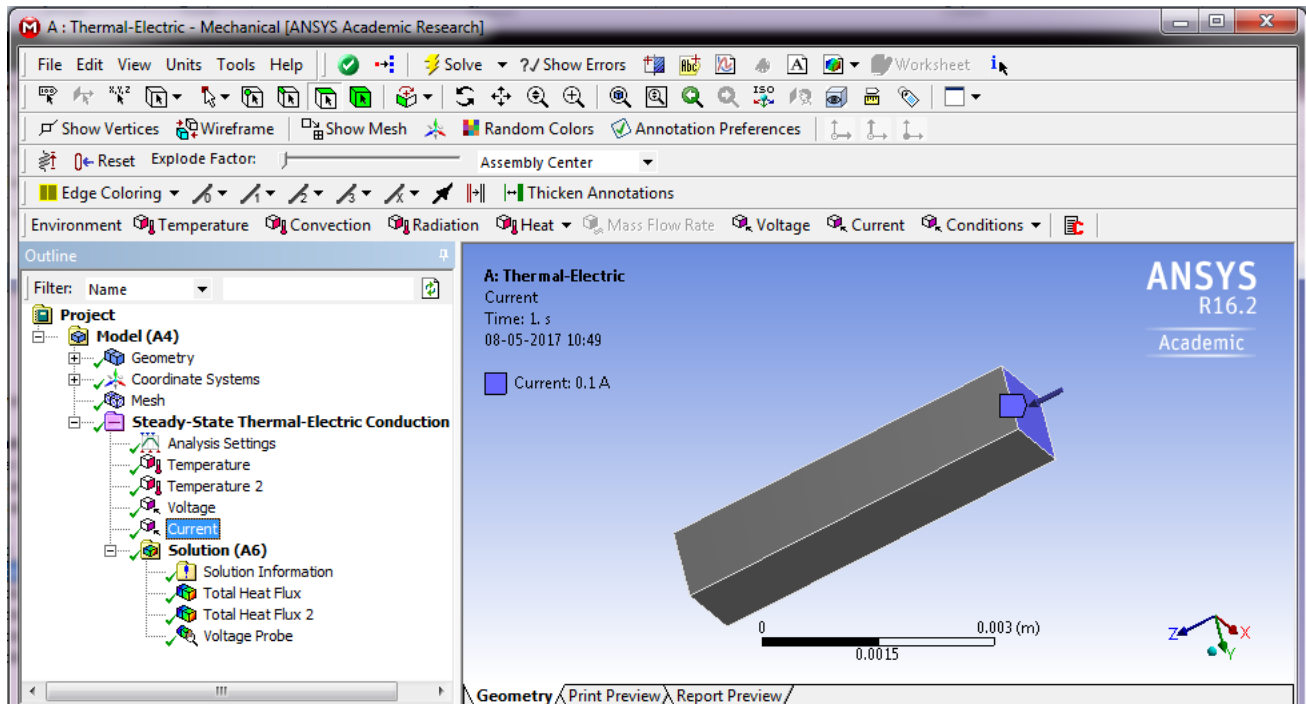


Figure 1-6: Thermoelectric solver interface showing the boundary conditions (temperature, voltage and current) on the left side pane and the simulated single TE leg on the right-side workspace. The blue arrow on the rectangular TE leg indicates the direction of current flow.

1.2.2 Analytical method – Ioffe’s Constant Properties Model (CPM)

Numerical solution methods such as FEM are time consuming and costly and are therefore inconvenient for parameter studies to determine suitable geometry and boundary conditions for optimizing performance in different application scenarios. In order to quickly estimate the efficiency and power output, a constant properties model (CPM) suggested by Ioffe is often used [54-57]. Consider a single TE leg out of a pn pair as shown in Figure 1-7a, maintained between constant hot and cold sides temperatures. In each leg, there are three mechanisms contributing to the heat flow at each side which are indicated by blue arrows on the right [58, 59]. The generated heat flow due to temperature difference (indicated as Q_K), the Peltier (indicated as Q_π), and the Joule heat (indicated as Q_J), are transported. Figure 1-7b schematically shows the heat transfer mechanisms in a TE leg: part of the Peltier heat difference between the hot and cold sides is converted into useful electrical power (P_{el} and P are equivalently used throughout this work).

At the hot junction, the energy balance consists of

- Fourier heat conduction ($Q_k = K\Delta T$) away from the hot side
- Peltier heat flowing away from the hot side ($Q_\pi = I\alpha T_h$) and
- Half of the heat from resistive Joule heating flowing towards the hot side ($Q_J = -\frac{1}{2}I^2 R_{in}$)

At the cold junction, the energy balance consists of

- Fourier heat conduction ($Q_k = K\Delta T$) towards the cold side
- Peltier heat flowing towards the cold junction ($Q_\pi = I\alpha T_c$) and
- Half of the heat from resistive Joule heating flowing towards the cold side ($Q_J = \frac{1}{2}I^2 R_{in}$)

From the energy balance, the following equations hold

$$Q_h = K\Delta T + I\alpha T_h - \frac{1}{2}I^2 R_{in} \text{ and } Q_c = K\Delta T + I\alpha T_c + \frac{1}{2}I^2 R_{in}. \quad (18)$$

Where Q_h and Q_c are the total heat flowing into and out of the TEG respectively.

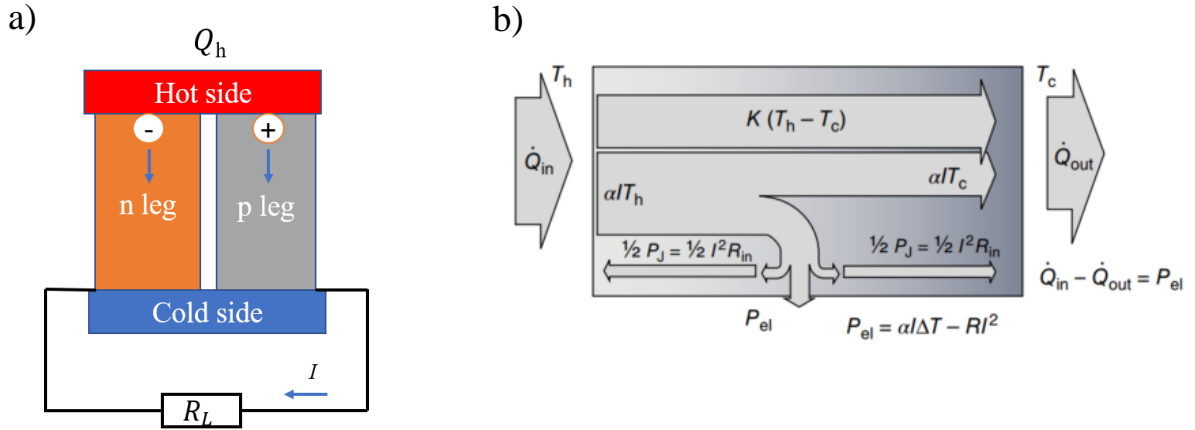


Figure 1-7: a) Schematic of a p-n leg pair connected to an external load resistor R_L . The heat flow direction for a leg is shown on the right. As current I flows through the TE leg, Joule heat Q_J , and Peltier heat Q_π , are generated. Fourier heat Q_k flows due to the supplied temperature difference, b) Schematic representation of heat transfer and electrical power production in a single leg. Here, $\dot{Q}_{in} \leftrightarrow Q_h$, $\dot{Q}_{out} \leftrightarrow Q_c$, $R_{in} \leftrightarrow R$ and $P_{el} \leftrightarrow P$ are equivalently used (taken from [28]).

As the heat flows from hot to cold junction, a certain portion of the heat is converted into electrical power [27]. Hence, from Eq. (18),

$$P = Q_h - Q_c = I(\alpha\Delta T - IR_{in}). \quad (19)$$

The external load resistance plays an important role for the operation of a TEG as it determines, together with the inner resistance, the current flow. Typically, power vs. current and efficiency vs. current characteristics are studied in the optimization procedure as shown in Figure 1-8 and the TEG is operated at the optimum current corresponding to the peak performance (either power or efficiency). Considering a TE leg connected to an external circuit as shown in Figure 1-4, eq. (6) can be written as

$$0 = (V_o - R_{in}I - R_L I)I \quad (20)$$

Where,

$$I = \left(\frac{V_o}{R_{in} + R_L} \right) \quad (21)$$

Setting the ratio $m = R_L/R_{in}$, and from eq. (6), (21)(20) simplifies to

$$P = \left(V_o - R_{in} \frac{V_o}{R_{in}} \frac{1}{(1+m)} \right) \left(\frac{V_o}{R_{in}} \frac{1}{(1+m)} \right) \quad (22)$$

$$P = \frac{V_o^2}{R_{in}} \frac{m}{(m+1)^2}$$

The maximum power is obtained by setting $\frac{dP}{dI} = 0$. Therefor from eq. (19), it can be seen that P_{max} occurs when

$$I = \alpha \frac{\Delta T}{2R_{in}} \quad (23)$$

This current I is called the optimum current for maximum power, $I_{opt,p}$. Therefore P_{max} is given from eq. (22) as

$$P_{max} = \alpha^2 \frac{\Delta T^2}{4\rho L} A \quad (24)$$

From eq. (23) and (24) it can be deduced that for P_{max} $R_L = R_{in}$ i.e., $m = 1$. Here, $\alpha^2 \sigma$ ($\sigma = \frac{1}{\rho}$ is the electrical conductivity) is called the thermoelectric power factor.

By maximising $\eta = \frac{P_{el}}{Q_h}$, the maximum efficiency is obtained as [27],

$$\eta_{max} = \frac{\Delta T}{T_h} \frac{-1 + \sqrt{1 + zT_m}}{\frac{T_c}{T_h} + \sqrt{1 + zT_m}} \quad (25)$$

where $\frac{\Delta T}{T_h}$ is the Carnot efficiency, $zT_m = \frac{\alpha^2}{\rho\kappa} \cdot T_m$ is the dimensionless figure of merit and $T_m = \frac{T_h+T_c}{2}$ is the mean temperature. $\eta_r = \frac{-1+\sqrt{1+zT_m}}{\frac{T_c}{T_h}+\sqrt{1+zT_m}}$ is called the reduced efficiency which will be

discussed briefly in the section on compatibility (section 1.5.1). As can be seen, efficiency is limited by the Carnot efficiency. The optimum current at maximum efficiency ($I_{opt,\eta}$) is given by

$$I_{opt,\eta} = \frac{\alpha\Delta T}{R(1 + \sqrt{1 + zT_m})} \quad (26)$$

which occurs at $R_L = R_{in}\sqrt{1 + zT_m}$. Therefore, as can be seen from Figure 1-8, the optimum current for maximum power is always higher than the optimum current for maximum efficiency. For optimizing TEGs for application scenarios, curves as given in Figure 1-8 are calculated for different zT and hot side and cold side temperatures and for any other parameter that needs to be optimized.

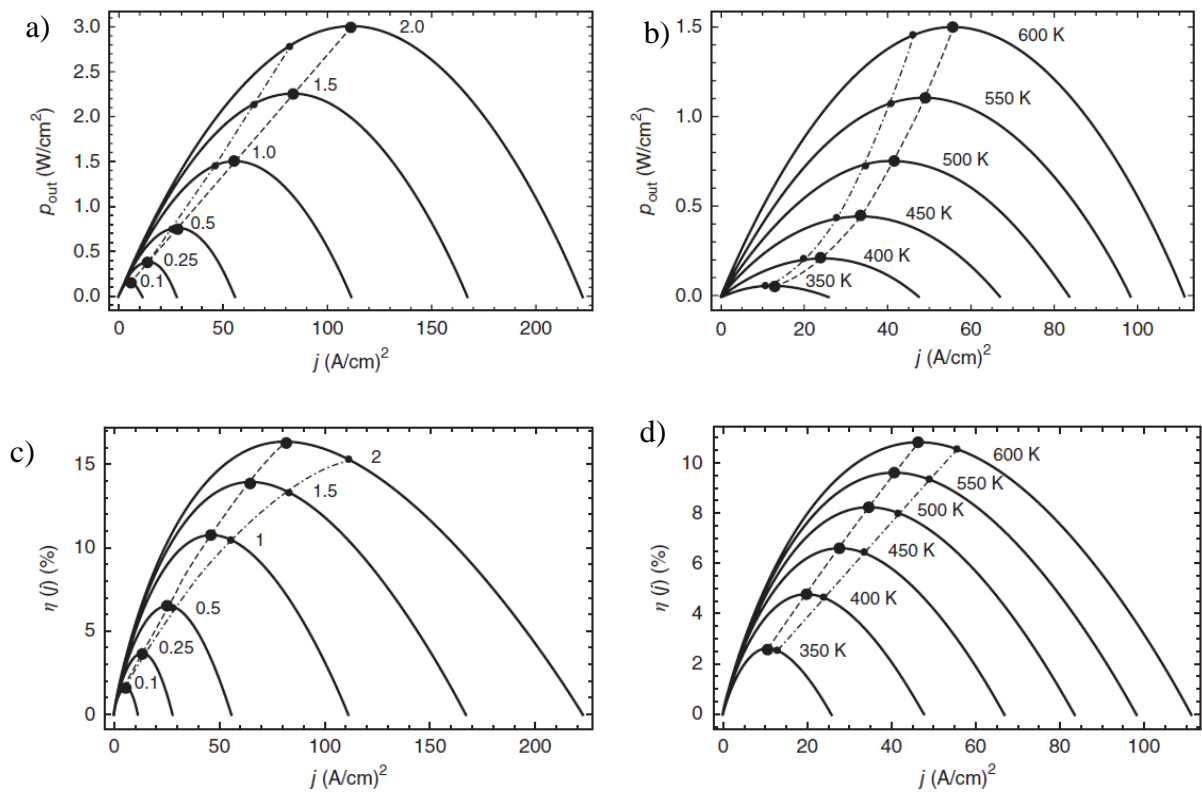


Figure 1-8: Electric power density p_{out} vs. j a) for different zT_m ($T_h = 600$ K) b) for different T_h ($zT_m = 1$); TEG efficiency η vs. j characteristics c) for different zT_m ($T_h = 600$ K) d) for different T_h ($zT_m = 1$), calculated for a typical TE material (taken from [28]). The larger black dotted lines represent points of maximum power or efficiency accordingly and dotted and dashed lines to serve as eye guide for primary

and secondary points of maximum. For example, in a) the dashed lines with bigger solid dots represent points of P_{\max} and dotted lines and small dots represent points of η_{\max} . Here, $T_c = 300$ K, $\alpha = 180$ $\mu\text{V/K}$, and $\kappa = 1.5$ W/m K.

It has become almost synonymous when estimating device performance from among them properties that the analytical expressions given by eq. (24) and eq. (25) are the power output and efficiency of a TEG. However, as these are derived based on the assumption of constant properties, the question of selection of appropriately averaged values [60-64] for the TE properties to be used in the CPM formulae has not been answered clearly yet. Usually, temperature averaging (averaging of the properties over the temperature scale of the range of consideration – in the following denoted by T_{Av}) is widely used but is physically not strict [18, 28, 47, 54, 65]. The error involved can be high depending on the chosen temperature range and the temperature dependence of the material [28, 61, 64, 66]. So far, there has not been a clear explanation as to why sometimes CPM works better and sometimes not. Often, the neglect of Thomson heat and/or the Joule heat asymmetry are assumed to be the reasons why CPM calculation deviates from exact results and there are some publications arguing on that the Thomson heat is significant [40, 67-69] while others argue that it is negligible. Neither a clear conclusion on the reasoning, nor a suitable average that can be used universally for all materials and boundary conditions, has been proposed yet. Therefore, Chapters 3 and 4 in the thesis address these issues.

Although not required for performance estimation, it can be seen that for CPM, eq. (17) reduces to

$$\kappa \frac{d^2 T}{dx^2} = -\frac{j^2}{\sigma} \quad (27)$$

resulting in a parabolic T profile

$$T(x) = T_h + (T_c - T_h) \frac{x}{L} + \frac{j^2}{2\sigma\kappa} x(L - x). \quad (28)$$

1.3 Factors affecting performance of a TEG module

To summarise, as can be seen from eqs. (24) and (25) and Table 1, the performance of a single TEG leg (in 1D, considering ideally conductive bridges) depends on

- Material properties: α , σ (or ρ), κ
- Geometry: area, length and the number of TE legs

- Contact resistances
- Supplied temperatures/heat flux
- External load resistance (or current) (discussed in the previous section 1.2.2)

Additionally, working/boundary conditions (BC) like coupling to the surrounding and convection, and radiation affect the performance. These losses can be ideally minimized using thermal insulation. These effects are discussed in detail in [70, 71].

Let us discuss briefly how exactly these factors affect the power output and efficiency in a specific single leg.

Material:

The zT is a measure of the effect of material properties on efficiency as indicated by eq. (25) and is discussed further in section 1.4. This is under the CPM assumption and hence, the heat flow due to inner heat sources is assumed to be symmetric. However, in reality, the heat transfer from the hot side to the cold side could be asymmetric due to the temperature dependence of material properties and is discussed in detail in chapters 3 and 4.

Geometry and contact resistance:

Further, as can be seen from eq. (24)(24), the power output increases with area and decreases with length of the TE leg due to the internal resistance. Ideally, the power output goes to infinity for a leg of infinitesimally small length. However, this cannot happen in reality since contacts are present at the ends of the TE leg and at small leg lengths the contact resistance will dominate. Additionally, with infinitesimally small length, the thermal conductance would be infinite and the temperature difference would no more be maintained. Gao Min [72-74] obtained a simple analytical expression for power output incorporating the effect of thermal and electrical contact resistance, based on CPM.

$$P = \frac{\alpha^2}{2\rho} \frac{A(T_h - T_c)^2}{(L + n)(1 + 2rw)^2} \quad (29)$$

$$\eta_{\max} = \left(\frac{T_h - T_c}{T_h} \right) \left\{ (1 + 2rw)^2 \left[2 - \frac{1}{2} \left(\frac{T_h - T_c}{T_h} \right) + \frac{4}{zT_h} \left(\frac{L + n}{1 + 2rw} \right) \right] \right\}^{-1} \quad (30)$$

Here, $r = \kappa/\kappa_c$, $w = L_c/L$ and $n = 2\rho_c/\rho$. Subscript c is used to indicate the properties of the contacts. Note that ρ_c here is the specific contact resistance ($\Omega \text{ m}^2$) and hence n has the unit of length. Unlike n , r has no dimensions as κ_c indicates thermal conductivity of the contact

material. Normally, a good contact resistance is supposed to be around less than 10% of the internal resistance of the TE leg [16]. For optimisation of performance curves like the ones shown in Figure 1-9 are plotted, where the power vs length curve has a peak and drops for smaller lengths. The longer the TE leg, the smaller will be the influence of contacts and hence the efficiency curves increase initially and are nearly constant, reaching the limit corresponding to ideal contacts further on.

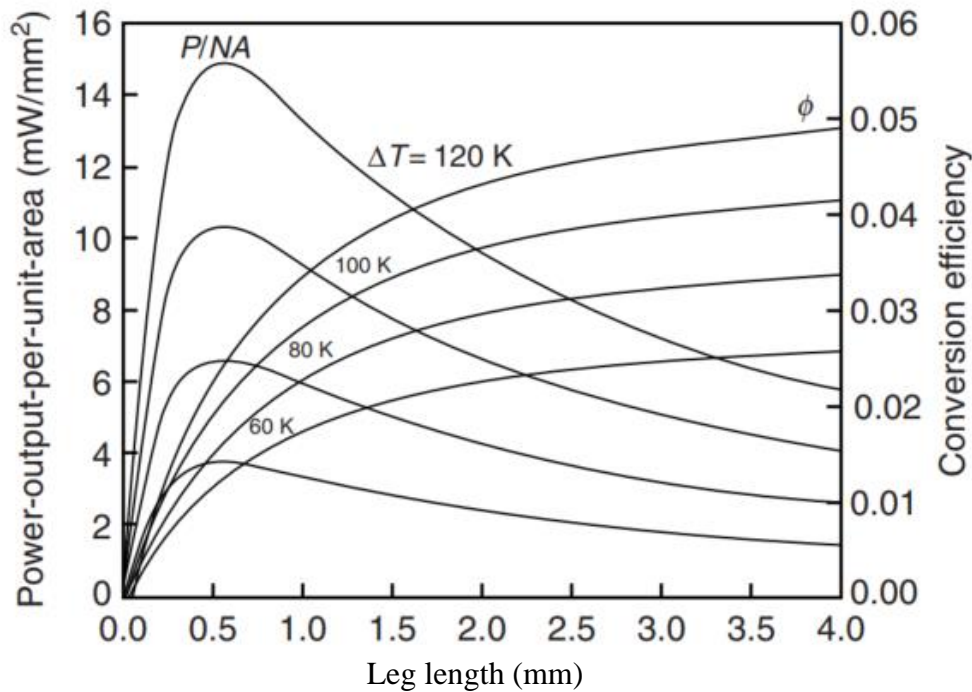


Figure 1-9: Power output density (P/NA) characteristics (left y-axis) and conversion efficiency (right y-axis) for different ΔT for a commercial TE material with thermal and electrical contact resistances (taken from [18]). Here, N indicates the number of pn leg pairs and A is the cross-sectional area of the pn couple, $n = 0.05$ m and $r = 5$.

Temperature:

The larger the temperature difference, the larger is the power output and efficiency according to eqns. (24) and (25). However, the efficiency cannot exceed the Carnot limit as stated earlier.

1.4 Material aspects of thermoelectric performance

1.4.1 Optimization of material properties

As can be seen from eq. (25), the material efficiency is mainly determined by the dimensionless figure of merit zT . Intuitively, it can be seen that for a good thermoelectric material, the

Seebeck coefficient should be high for generating more power output, and electrical conductivity (σ) should be high to reduce the losses due to the internal resistance, while the thermal conductivity should be low. However, these are contradicting requirements since the electrical conductivity is directly proportional to the carrier concentration while the Seebeck coefficient is inversely related to n . Additionally, since charge carriers also carry heat with them, the thermal conductivity consists of the electronic part (κ_e) as well as the lattice conduction part (κ_L) as given by [25, 73],

$$\kappa = \kappa_L + \kappa_e , \quad (31)$$

where $\kappa_e = L \sigma T$ considers a single type of charge carriers, according to Wiedemann Franz law (L is the Lorenz number). Hence, the electronic part of thermal conductivity and electrical conductivity are directly proportional. Therefore, TE materials need to be optimized by tuning the carrier concentration through doping, and possibly compositional variations to obtain the best performance [54, 75-82]. The variation of the three main thermoelectric properties, α , σ and κ along with zT , with the carrier concentration n , for insulators, semiconductors and metals is shown in Figure 1-10.

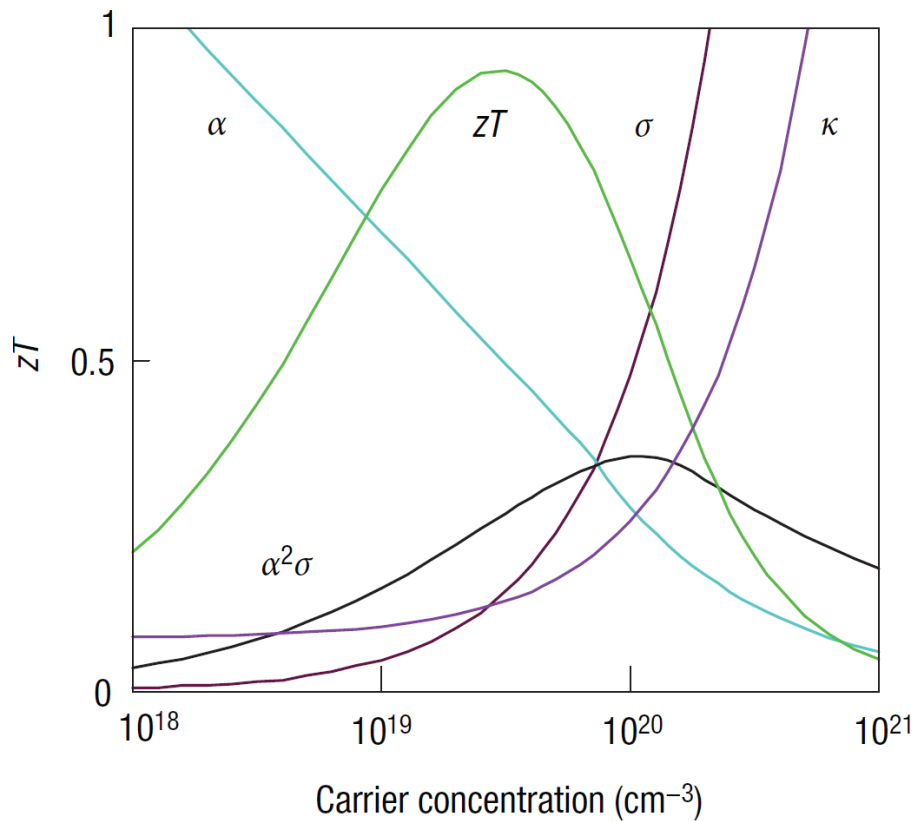


Figure 1-10: Typical variation of TE material properties α , σ and κ and zT vs free carrier concentration for parameters corresponding to a typical TE material [25].

To reduce time-consuming and costly efforts to experimentally prepare numerous samples to optimize the TE properties, modelling and predicting material properties from basic electronic band structure data assuming probable scattering mechanisms is a usual approach. One of the simplest models to calculate material properties of highly degenerate (heavily doped) semiconductors is the Single Parabolic Band (SPB) model [83, 84]. The SPB model predicts the $\alpha(T)$, $\sigma(T)$ and $\kappa(T)$ of materials assuming that only a single parabolic band contributes to conduction and hence when bipolar contribution occurs (as in a typical semiconductor material), SPB can no longer be applied. In such cases at higher temperatures where bipolar conduction dominates, more sophisticated models such as a two band model [84, 85] or multi band model [83] can be used. The main advantage of SPB model lies in its simplicity. The fundamental idea involved in SPB modelling is discussed in the next section (1.4.2).

Traditionally, zT is being used as a measure for material optimization, usually for optimizing the carrier concentration. However, since optimizing n based on zT is for fixed temperatures and not for a temperature range as in real application scenarios, the optimum n for a module could be wrongly predicted [86, 87]. Hence, Chapter 5 discusses the effect of using zT as a parameter for optimization of material parameters and additionally, presents a combined material and device model to address TEG efficiency directly as the maximization parameter for optimizing material parameters. Further, the use of such a combined material-device model for grading and segmentation studies is discussed in Chapter 6.

1.4.2 Modelling TE properties using a Single Parabolic Band model

The band theory of solids describes the energy levels that the electrons/holes can occupy in a solid as well as the forbidden energy zones [88, 89]. Through this knowledge, the behaviour of solids such as electrical properties can be predicted using analytical relations. Energy band diagrams are obtained by solving the time-independent Schrödinger wave equation, and one such example for $\text{Mg}_2\text{Si}_{0.6}\text{Sb}_{0.4}$ is shown in Figure 1-11b. In this section a simple Single Parabolic Band (SPB) model is presented to outline the basic idea behind material modelling.

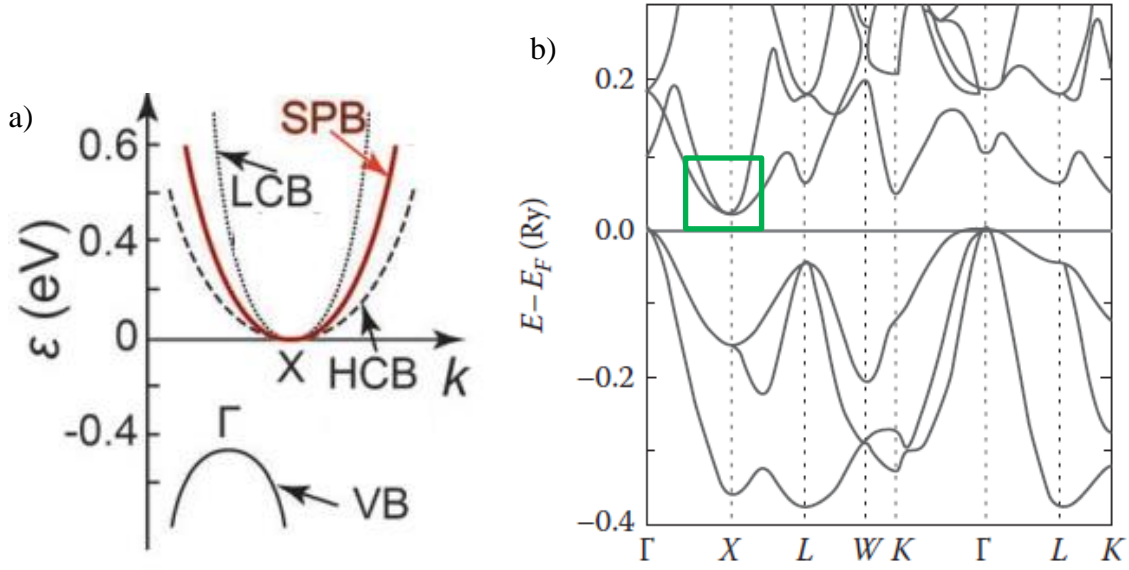


Figure 1-11: a) Single Parabolic Band approximation to $\text{Mg}_2\text{Si}_{0.3}\text{Sn}_{0.7}$ solid solution [90]. Here, the combination of a light conduction band (LCB) and a heavy conduction band (HCB) are approximated to a single parabolic band. b) Electronic band structure of $\text{Mg}_2\text{Si}_{0.6}\text{Sb}_{0.4}$ where the Fermi level is indicated by the horizontal line [91]. The x-axis indicates different points in the Brillouin zone. At the X point (highlighted in green), the two converging conduction bands that contribute to conduction can be approximated by an SPB.

The SPB assumption comes from the fact that the energy dependence of electron waves in the crystal lattice can be considered to be parabolic [83, 88] as shown by Figure 1-11a for $\text{Mg}_2\text{Si}_{0.3}\text{Sn}_{0.7}$ where the (two converged) conduction bands at the X point are approximated by an SPB. Generally, the energy bands are not always parabolic, however, since most thermoelectric materials have their Fermi levels close to the bottom of the conduction band (for n-type) or near the top of the valence band (for p-type), the assumption of parabolic bands as shown in Figure 1-11 is often justified.

The main equations governing the SPB model are obtained from the Boltzmann transport equation under the relaxation time approach and are given in Chapter 5. The significance of the model is that the properties can be described by a single density of states effective mass m_D^* and assigning suitable valley degeneracy N_v (number of distinct extrema of the Fermi surface contributing to conduction) to the single band under consideration as given by eq. (32)[88, 89].

$$m_D^* = \sqrt[3]{N_v^2 m_S^*} \quad (32)$$

Here, m_S^* is the single valley effective mass. m_S^* plays an important role in the electrical conductivity since the mobility of charge carriers depends on it through the following equation[88].

$$\mu_D = \frac{2e}{3m_S^*} \tau_0 \frac{F_0(\eta_c)}{F_{0.5}(\eta_c)} \quad (33)$$

Here, μ_D is the drift mobility of electrons and $F_i = \int_0^\infty \frac{\epsilon^i d\epsilon}{1+e^{[\epsilon-\eta_c]}}$ is the Fermi integral of the order i , η_c is the chemical potential, e is the electronic charge, τ_0 is the total relaxation time constant which depends on the scattering mechanisms such as acoustic phonon scattering, alloy scattering, grain boundary scattering, point defect scattering, ionized impurity scattering and so on, according to the scattering parameter λ . For example, for acoustic phonon scattering, $\lambda = 0$ and τ_0 has a $T^{-1.5}$ dependence [17, 88, 92].

According to the Drude theory, which attempts to explain the behaviour of electrons under the influence of electric field E as governed by scattering process like in the kinetic theory, the electrical conductivity is given by [93]

$$\mathbf{j} = e n v_d \quad (34)$$

where v_d is the drift velocity given by $E\mu_D$. Therefore, according to Ohm's law $j = \sigma E$ the electrical conductivity is given by $\sigma = en\mu_D$. The scattering mechanisms determine the temperature dependence of the electrical conductivity. The Seebeck coefficient is given by

$$\alpha = \left(\frac{k_B}{e}\right) \left(\frac{(2+\lambda)F_{\lambda+1}(\eta_c)}{(1+\lambda)F_\lambda(\eta_c)} - (\eta_c)\right) \quad (35)$$

For metals and highly degenerate semiconductors, this simplifies as follows.

$$\alpha = \frac{8\pi^2 k_B^2}{3eh^2} m_D^* T \left(\frac{\pi}{3n}\right)^{2/3} \quad (36)$$

where k_B is the Boltzmann constant and h is Planck's constant. λ is the scattering parameter [88]. It can be seen that the Seebeck coefficient increases with temperature and effective mass and reduces with increase in charge carrier concentration, while thermal and electrical conductivity increase with n . Since these are contradictory requirements, fundamental parameters governing these properties need to be optimized. By modelling α , σ and κ and therefore zT with the SPB model, the optimum carrier concentration for maximum zT or efficiency can be found. A contour plot of a 2D dependence of zT for p-Mg₂Si_{1-x}Sn_x at 500 K

for which the carrier concentration and composition are to be optimized is shown in Figure 1-12. Here, acoustic phonon scattering and alloy scattering mechanisms for the solid solution were used [94]. The red area indicates the region with optimum n and x . In chapter 5, the 1D solution method developed in chapter 3 is combined with the SPB model and the efficiency is directly predicted from the T dependent α, σ and κ calculated by the SPB model. For comparison, the use of a temperature-averaged figure of merit (zT_{Tav}) for determining optimum parameters is also discussed.

Since bipolar conduction, which is relevant at higher temperatures, is not considered in a SPB model, two-band models are required to model properties of materials at higher temperatures appropriately. Therefore, a two band model description for Mg_2Sn is used in Chapter 6 and the use of the combined material-device model for studying the effect of grading and segmentation (which will be introduced in the following section (1.5)) is discussed.

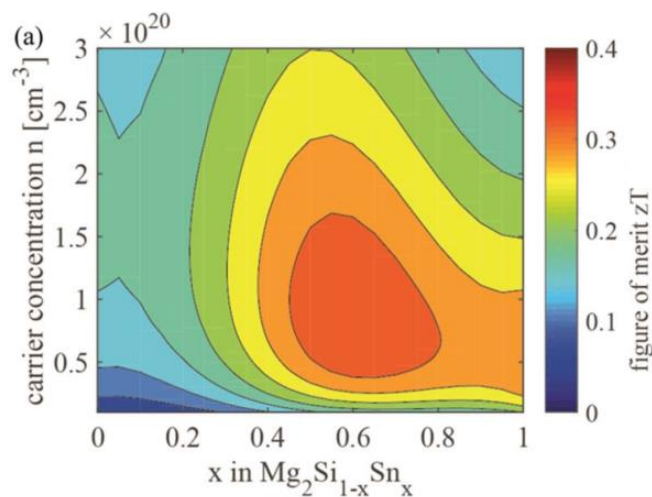


Figure 1-12: Modelling zT using SPB model, zT variation with composition and carrier concentration in p- $Mg_2Si_{1-x}Sn_x$ at 500 K [95].

1.5 Material grading and segmentation

As we have seen that the temperature dependence of the material properties affects the heat generation and transfer according to eq. (17), one of the important problems in designing a TEG is finding the optimum material profile along the length of the TE leg, for best performance.

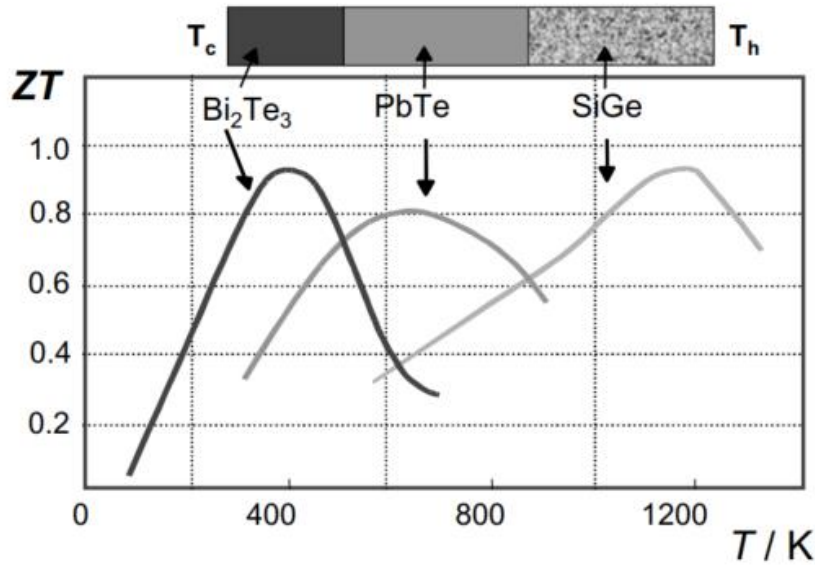


Figure 1-13: Concept of material segmentation depicted using three materials Bi_2Te_3 , PbTe and SiGe which have their zT_{max} at different temperatures of about 400 K, 650 K and 1190 K respectively. A TE leg made of these materials together as depicted in the figure, operating between a $T_h = 1200$ K and $T_c = 300$ K might be expected to have a higher overall efficiency as each material is operating near its zT_{max} [23].

Grading and segmentation are ways of improving performance of TEGs by modifying the properties of the TE leg along its length, a concept initially proposed by Ioffe [23]. Segmentation involves using homogeneous material segments with peak performance at different temperature intervals along the TE leg as shown in Figure 1-13. As can be seen, the zT_{max} for each of these materials occurs at different temperatures and hence having these segments work together for a temperature interval between 300 K to 1200 K can improve efficiency. Functional grading (or material grading) is fundamentally a continuous gradual segmentation. Material grading involves e.g. changing the material composition and/or the carrier concentration along the length of the TE leg [23, 96].

Computational techniques to theoretically find the performance of segmented and graded TE legs have been developed [18, 28]. The assumption here is that the TE leg is made up of a number of small segments as shown in Figure 1-14 with constant properties each. Applying suitable boundary conditions, the constitutive equations are formed and solved. In our case, the effects of segmentation and grading were calculated using the tool developed in chapter 6. As the 1D solution used to calculate the temperature profiles in homogeneous TEG elements (Chapter 3) is also based on dividing the TE leg into small segments and considering fully T

dependent material properties, it is quite convenient to study the effect of grading and segmentation with this tool, likewise.

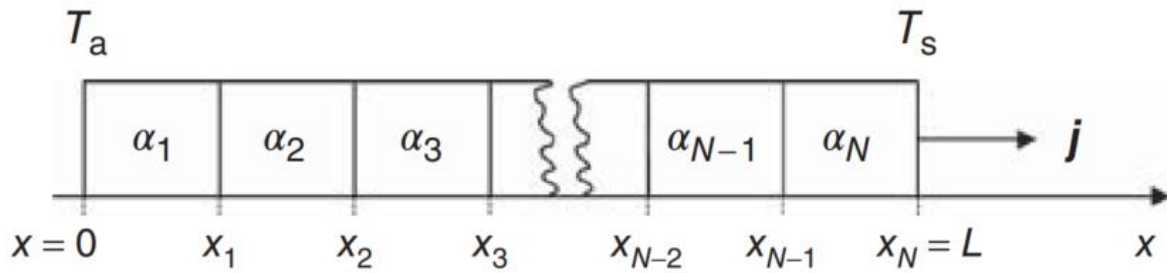


Figure 1-14: A segmented leg in 1D maintained between temperatures T_a at $x = 0$ and T_s at $x = L$ with current density j flowing through it [28].

As seen in the previous section (section 1.4), the optimum carrier concentration varies depending on the local temperature of interest. Hence, in this thesis, segments were made of the same material composition but with the properties corresponding to the optimum carrier concentration for each segment i.e. with the carrier concentration that gives the highest efficiency for the temperature interval of that segment. From the integrated SPB-TEG calculation tool introduced in the chapter 5, an example grading with the optimum n based on local maximum zT for each T and based on maximum efficiency for each segment are shown in the discussion chapter 6.

One of the major challenges with segmentation is the effect of contact resistance between the segments which should not overpower the gain in efficiency/CTE mismatch etc. [97]. Another important factor to consider in segmented and graded materials is the compatibility between segments. The following section sheds light on this.

1.5.1 Compatibility

The concept of compatibility originated from around 1960s, in the works of Sherman [98] and was further developed by Snyder and Ursell [99]. The concept arises from the fact that the optimum current depends on the material properties as also can be seen from eqs. (23) and (26) and if the TEG is operated at non-optimum currents, performance drops. This concept can be transferred to an infinitesimal element in a TEG leg, and thus the condition of optimal current density in dependence on material properties can be formulated locally. In a segmented element, the j_{opt} condition may be different between the segments because of their different TE properties, but the current through all elements, as connected serially, will be the same.

Thus, independent of the choice of j it will be deviating from the locally optimum current in most of the segments. Achieving compatibility means to adjust the properties of the joined segments in a way that the optimum current condition is fulfilled in each segment simultaneously.

In principle same problem exists when joining a p- and an n-type leg into a couple. However, this can easily be resolved by adjusting the ratio of the cross sections of p and n-type legs. Changing the ratio will vary the electric current density ratio between p and n independently from their heat flux ratio. The crux for segmentation is that the optimum current density condition can be traced back to a relation between electric flux and (Fourier) heat flux. Because of the electrical and thermal serial connection of the segments in a segmented leg, the ratio between thermal and electrical flux will not change when varying the cross section. Thus, the only option to reduce non-compatibility is varying the TE properties locally.

The clue of the compatibility concept is that a local condition was formulated that describes the state of compatibility in terms of material properties, in relation to the electrical and Fourier heat flux. In a real element with T -dependent properties the TE properties will vary locally and with them the j_{opt} condition will vary locally, continuously. If it varies very little over the whole T range, i.e. the whole leg, we call it self-compatible.

In the compatibility approach, the efficiency is redefined in terms of intensive quantities with inherent constraints, avoiding the explicit need for spatial dependence. Through such a definition, the efficiency is seen as an intensive thermodynamic quantity and makes the inherent constraints within the TE heat-current flow clearer. In this process, an additional parameter called the compatibility factor is identified in addition to z as a metric to be considered while designing modules.

This approach considers a TE leg to be made of infinitesimal segments each consisting of constant properties at that segment and considers the compatibility of heat and current flow within such segments. Considering the relative current density u defined to be the ratio of electrical to thermal current, i.e., $u = \frac{-j}{\kappa \frac{dT}{dx}}$ (negative sign is due to the sign convention according

to Figure 1-4), eq. (9) and (11) can be rewritten in terms of u as, $q = -\kappa \frac{\partial T}{\partial x} - \alpha T u \frac{dT}{dx} = -\kappa \frac{dT}{dx} (1 + \alpha T u)$ and $p_v = j(\alpha \nabla T + \rho j) = -u \kappa \frac{dT}{dx} \left(\alpha \nabla T - \rho u \kappa \frac{dT}{dx} \right) = -\kappa \left(\frac{dT}{dx} \right)^2 u (\alpha -$

$u\rho\kappa$). Therefore, the efficiency at infinitesimal distance dx for a cross section of the leg can be written as,

$$\eta = \frac{p_v dx}{q} = \frac{\kappa \left(\frac{dT}{dx}\right)^2 u(\alpha - u\rho\kappa) dx}{\kappa \frac{dT}{dx} (1 + \alpha u T)} = \frac{dT}{T} \frac{u(\alpha - u\rho\kappa)}{\alpha u + \frac{1}{T}} \quad (37)$$

Here, $\eta_r = \frac{u(\alpha - u\rho\kappa)}{\alpha u + \frac{1}{T}}$ is the reduced efficiency and $\frac{dT}{T}$ is the infinitesimal Carnot efficiency.

$dx = \frac{dT}{\nabla T} \cdot \eta_r$ can be written in terms of the figure of merit z as

$$\eta_r = \frac{1 - \frac{u\alpha}{z}}{1 + \frac{1}{u\alpha T}} \quad (38)$$

The value of u which maximizes the reduced efficiency is called the compatibility factor s [18, 99]. s given by

$$s = \frac{\sqrt{1 + zT} - 1}{\alpha T} \quad (39)$$

As can be seen s is a T dependent material property and is independent of geometry. If u is quite different from s , then the material isn't converting heat efficiently into electricity. The significance of this approach is that the efficiency is written in terms of the minimal (reduced) number of variables. As s is T dependent, one can also check the self-compatibility within the leg by observing the change in $s(T(x))$ [24, 100, 101]. The maximum reduced efficiency which is achieved when $u = s$ is given by

$$\eta_{r,\max} = \frac{\sqrt{1+zT}-1}{\sqrt{1+zT}+1}. \quad (40)$$

Comparing eq. (25) and the case of T_h approaching T_c in eq. (40), we can easily see that compatibility approach is nothing but local formulation of maximisation of efficiency by adjusting the optimising current. The importance of the compatibility approach lies in the fact that it determines the efficacy of two adjacent TE segments to work together towards higher efficiency. A high zT everywhere along a segmented leg doesn't necessarily mean good compatibility. Therefore, for grading and segmentation studies, it is important to check the compatibility of the segments to judge if performance is improved.

In this thesis work, the self-compatibility of graded material designed in Chapter 6 is checked and it is analyzed whether the gain in efficiency by grading is due to increased compatibility and/or increased zT .

2 Aim and overview of the thesis

The objective of this thesis work is to find fast and accurate ways to calculate the performance of TEGs under steady state operation. To this end, the use of the most commonly used CPM model is analyzed and the shortcomings are pointed out. Additionally, an alternate and fully T dependent exact solution method based on a simple iterative procedure is suggested and the advantages of this method are shown through a combined material-device modeling which can be used to study the effect of grading and segmentation in TE legs. The contents of the thesis are arranged as follows:

In Chapter 3 (Paper 1), the use of appropriate averages is explained by considering the effect of the contributing mechanisms to the bending of the T profile: pure Fourier heat, Joule heat and Thomson heat. The individual contributions to the temperature profile are calculated using an iterative procedure, the use of which is validated using FEM. Through this simple calculation procedure, the calculation times are reduced by approximately 300 times compared to FEM solution.

The importance of the individual contributions to heat transfer in a TE leg is quantitatively discussed in Chapter 4 (Paper 2) and the remaining differences between CPM and temperature dependent calculations are discussed by means of an entropy flow diagram. The importance of the contribution of Thomson heat to inflowing heat in real device that is neglected in CPM, however, partly compensated in CPM by an additional amount of Peltier heat, is highlighted. With the entropy flow diagram, a correction for this incomplete compensation of neglected Thomson heat in CPM is suggested and graphically illustrated.

Additionally, the suitability of using a CPM to guide material optimization is discussed in Chapter 5 (Paper 3). It is shown that using zT (at e.g. the hot side temperature) as a metric for carrier concentration optimization can mislead the search for optimum n , as zT is a local parameter and insufficient for modules which operate over an extended temperature range. Therefore, the use of efficiency as target parameters for material optimization is used and the results are compared to or zT_{TAV} and to local zT . These calculations are employed on the popular p-type $Mg_2Si_{1-x}Sn_x$ solid solutions which need optimisation of n and x . Here, an SPB model is used to model the material properties and identifying the optimum values, providing a guideline for experimentalists.

In Chapter 6, the use of the combined material / device optimization tool developed and implemented in the previous chapters is discussed with a more accurate two-band model. With Mg_2Sn as an example material, the effect of functional grading and segmentation on module performance is presented. A two-band model is used to describe the material properties of Mg_2Sn to account for the relevant influence of bipolar conduction at upper temperatures and the degree of compatibility reached by a straight-forward local material optimization is checked for a graded TE leg.

Overall, with the developed tools, design optimization of TEG legs can be easily done and routes for gain in efficiency can be accurately predicted.

Paper Catalogue

Chapter 3: Paper 1

Chapter 4: Paper 2

Chapter 5: Paper 3

3 Using the Constant Properties Model for accurate Performance Estimation of Thermoelectric Generator Elements (Publication 1)

P. Ponnusamy¹, J. de Boor¹ and E. Müller^{1,2}

¹German Aerospace Center (DLR), Institute of Materials Research, D-51170 Köln, Germany

²Justus Liebig University Gießen, Institute of Inorganic and Analytical Chemistry, D-35392 Gießen, Germany

This paper/chapter explains the use of suitable averages while using a CPM model. A comparison of conventionally used averaging techniques is shown. By studying the temperature profiles for six commonly used materials, it is shown that the temperature averaging for Seebeck coefficient and spatial averages for electrical and thermal resistivities are physically appropriate.

This article was published on 15th March 2020 in Applied Energy Journal (Elsevier). The DOI of the article is <https://doi.org/10.1016/j.apenergy.2020.114587>. Author contributions are specified in the published article as well as at the end of this thesis.

3.1 Abstract

Thermoelectric devices convert thermal energy directly into electrical energy or vice versa. Analytically, the performance (efficiency and power output) of a thermoelectric generator can be quickly estimated using a Constant Properties Model (CPM) suggested by Ioffe. However, material properties in general are temperature dependent and the CPM can yield meaningful estimates only if the constant values of the TE properties used in the formulations are physically appropriate. In this study, a comparison of different averaging modes shows that a combination of integral averaging over the temperature scale for the Seebeck coefficient and spatial averages

for the electrical and thermal resistivities proves to be the best among the considered approximations to represent the constant property values. However, averaging spatially requires the knowledge of the exact temperature distribution along the length of the thermoelectric leg (temperature profile), which is usually obtained by Finite Element Method (FEM) calculations. Since FEM is costly and time consuming, a fast and easy way of obtaining a well approximated self-consistent temperature profile is used in this study. The relevance, magnitude and the physical origin of the non-linearity of the temperature profile are visualised by separately plotting the individual contributions to the bending of the temperature profile (Joule, Thomson and Fourier heat contributions). On analyzing the temperature profiles for different highly efficient thermoelectric materials, it is found that the non-constancy of the temperature dependence of the thermal conductivity significantly contributes to the deflection of real temperature profiles from a linear one. This mainly explains the considerable discrepancy of CPM results from exact calculations whereas, so far, the neglect of Thomson heat has been assumed to be the main source of discrepancy and several models with Thomson correction factors have been proposed. With our current view, such models cannot completely remove the discrepancy to CPM unless the T profile is taken into account and can lead to unpredictable error for different material cases and temperatures.

Keywords: TEG performance, Device modeling, Temperature profile, Constant properties model, Fourier heat, Thomson heat.

3.2 Introduction

Thermoelectric generator (TEG) materials work by converting a certain fraction of the heat passed through them into useful electrical power, involving interplay of the transport of charge and heat in the solid state. Typically, a thermoelectric (TE) module consists of a series of pairs of legs made of n- and p-type semiconductor material, electrically connected in series and thermally in parallel [1]. Consider a single TE leg of length L as shown in Figure 3-1, supplied with a constant hot side temperature of T_h and a cold side temperature of T_c , where $\Delta T = T_h - T_c$.

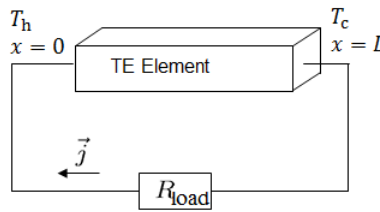


Figure 3-1: Schematic showing a TE leg connected in a circuit to an external load resistor. At open loop ($j = 0$), only Fourier heat is flowing whereas in non-zero current case additionally Joule, Peltier and Thomson heat are involved (j – current density).

At open circuit condition, the heat flow entering at the hot side (Q_{in}) is the same as the heat flow leaving at the cold side (Q_{out}) and no electrical power is generated. But, when the TE leg is connected to a load as shown in Figure 3-1, current $I = jA$ (j is the current density and A is the area of cross section) flows in this closed circuit due to the generated thermoelectric voltage and a part of the input heat, equivalent to $Q_{in} - Q_{out}$ is converted into the thermoelectric power P [2].

$$P = Q_{in} - Q_{out} = V \cdot I, \text{ where } V = V_o - R_{in}I, \quad V_o = \alpha\Delta T \quad (41)$$

Here, V is the output voltage at the TE leg which is given by the Seebeck voltage generated V_o (the maximum output voltage, reached at open loop) minus the voltage drop due to internal resistance (R_{in}) of the TE material ($R_{in} = \rho L/A$, where ρ is the electrical resistivity of the TE material, L – length). The material properties, α (Seebeck coefficient) and ρ are generally temperature dependent and hence the overall Seebeck voltage V_o and the net internal resistance (R_{in}) are calculated by integrating over temperature and length, respectively, *i.e.*, $V_o =$

$\int_{T_c}^{T_h} \alpha(T) dT$ and $R_{in} = \int_0^L \rho(T(x)) dx/A$. Here, $T(x)$ is the temperature profile (temperature distribution along the length of the TE leg).

Like for any thermodynamic machine, the efficiency (η) of a thermoelectric generator (TEG) is given by the ratio of output power (P) to the input heat flow (Q_{in}).

$$\eta = P/Q_{in} \quad (42)$$

Here,

$$Q_{in} = -\kappa_h \cdot A \cdot \frac{dT}{dx_h} + I \cdot \alpha_h \cdot T_h \quad (43)$$

which is the heat input at the hot side, split into the Fourier heat flow $-\kappa_h \cdot A \cdot \frac{dT}{dx_h}$ (including contributions to balance the Joule and Thomson heat released in the element) plus the absorbed Peltier heat flow $I \cdot \alpha_h \cdot T_h$ (κ being the thermal conductivity). Please note that Q_{in} , Q_{out} , $-\kappa_h A \frac{dT}{dx_h}$, $I \alpha_h T_h$ are formally heat flows [W]. The suffix h denotes the hot side values, with $\kappa_h = \kappa(T_h)$ and $\alpha_h = \alpha(T_h)$. Here, it is noteworthy that the gradient of $T(x)$ *i.e.*, $\frac{dT}{dx}$ is required for determining Q_{in} and, thus, the efficiency. $T(x)$ is obtained by solving the thermoelectric heat balance equation, which is a second order non-linear partial differential equation, written in 1D as,

$$\kappa(T) \frac{\partial^2 T}{\partial x^2} + \frac{d\kappa}{dT} \left(\frac{\partial T}{\partial x} \right)^2 - jT \frac{d\alpha}{dT} \frac{\partial T}{\partial x} = -\rho(T) j^2 \quad (44)$$

This equation is obtained from the physical implication that the divergence of flowing Fourier heat equals the sum of locally appearing Joule heat and Thomson heat [2]. Thomson heat is fundamentally the consequence of the local heat balance when flowing Peltier heat within the TE leg changes with local temperature variation due to the temperature dependence of the Seebeck coefficient $\alpha(T(x))$. Exchanged Peltier heat at the junctions of the n or p leg which is the difference of the inflowing and outflowing Peltier heat – to be distinguished from the flowing Peltier heat itself, $I \cdot \alpha \cdot T$, flowing at any point of a thermoelectric circuit – is considered as an additional heat input as in Eq. (43) and is relevant for the estimation of efficiency but is furthermore not affecting the shaping of the temperature profile. Here, τ is the Thomson coefficient which is given by $T \frac{\partial \alpha}{\partial T}$ [3]. In a strict case (incorporating the T dependence of the material properties α , κ and σ), the accurate $T(x)$ can be obtained by solving Eq. (44)

using numerical methods like Finite Element Methods (FEM) [4, 5], Finite Volume Methods (FVM) [6-8] or Finite Difference Methods (FDM) [5] and according numerical tools [9, 10]. These solution methods are time consuming and costly and are impractical for parameter studies if the geometry is varied as is intended for computational TEG module design.

On the contrary, in order to quickly estimate the electrical output power and the conversion efficiency of a TEG, a constant property model (CPM) suggested by Ioffe is often used [3]. But, the question of selection of appropriately averaged values [11-15] for the TE properties to be used in the CPM formulae has not been answered clearly yet. Practically, averaging of the properties over the temperature scale of the range of operation (temperature averaging – in the following denoted by T_{Av}) is the easiest and accordingly has been used already from Ioffe's times [3]. It has been shown to work well for certain materials [2, 5, 9, 16]. Nevertheless, the error involved in such an approximation can be high depending on the chosen temperature range and the temperature dependence of the material [5, 12, 15, 17], as will be shown in this work. So far, the neglect of Thomson heat and the Joule heat asymmetry are generally assumed to be the reasons why CPM deviates from exact results and hence, there are many publications on the importance of Thomson heat [18-21]. But, a clear conclusion has not been achieved yet nor has a suitable average been proposed that can be used universally for all materials and boundary conditions.

Apart from CPM, there are also simplified models based on assuming different analytical formulations for the T dependencies of the material properties [16, 22-24] and/or different mathematical functions for $T(x)$ [25-27]. For example, recently, Ryu *et al.* [24] suggested an interesting model based on the exact theory, with linear assumption of $\alpha(T)$ and $\kappa\rho(T)$ which holds good for most of the thermoelectric materials. Some models are based on electrical analogy of thermal flow [28], some assume a constant Thomson coefficient [29, 30] and some assuming different mathematical functions for the Thomson heat [19, 31]. However, these are again approximate methods applicable for specific materials and for certain temperature ranges. On similar lines, recently, a novel definition of a technologically relevant figure of merit ZT_{eng} has been suggested by Kim *et al.* [12], but here again temperature averages are used to compensate for the 'missing' Thomson heat in CPM [14, 32].

In addition to the above, the excel calculator by Snyder *et al.* [2, 33] based on Finite Difference Method (FDM), provides fast and accurate results with reduced variables based on the compatibility approach. But, the temperature profile, which is significant for understanding the

working of a TE element, is not calculated explicitly in this approach and since the calculations are in terms of reduced current, a direct picture of the different TE effects taking place in the leg is not easily visualised. Moreover, the calculation is no more straightforward when thermal and electrical contact resistances have to be considered in the calculation.

In this study, the degree of universality of existing averaging methods for CPM is analysed on material classes with different T dependence, selected based on low, medium and mid-high temperature operations and physically appropriate averages to be used with CPM are proposed. By analysing the individual contributions to the temperature profile, we will demonstrate how the TE performance estimation using CPM deviates unpredictably in different material cases and different operating temperature ranges when conventional averaging methods are used. Further, based on the temperature profiles, we will explain when and why CPM works and why it fails in some cases.

3.3 Methods and results

3.3.1 Estimation of TE performance by CPM

According to the Constant Properties Model (CPM) suggested by Ioffe [3], accumulated heat at the hot and cold sides is given by,

$$Q_{in} = Q_h = K\Delta T + \alpha T_h I - \frac{1}{2} R_{in} I^2 \quad \text{and} \quad Q_{out} = Q_c = K\Delta T + \alpha T_c I + \frac{1}{2} R_{in} I^2 \quad (45)$$

Here K is the thermal conductance given by $\frac{\kappa A}{L}$. $K\Delta T$ corresponds to the average Fourier heat flow along the element, $\alpha T_h I$ and $\alpha T_c I$ are the absorbed and released Peltier heat and $R_{in} I^2$ is the Joule heat released in the leg which overlays the average Fourier heat flow, being transported by half to each of the hot and cold sides, respectively. The maximum efficiency η_{max} of a TE leg is obtained from the above equations (substituting Eq. (45) in Eq.(42)) and is given by,

$$\eta_{max} = \frac{\Delta T}{T_h} \frac{(-1 + \sqrt{1 + zT_m})}{\left(\frac{T_c}{T_h} + \sqrt{1 + zT_m}\right)} \quad (46)$$

where $\frac{\Delta T}{T_h}$ is the Carnot efficiency and zT_m is the dimensionless figure of merit at the mean temperature $T_m = \frac{T_h+T_c}{2}$, defined as $\frac{\alpha^2}{\rho\kappa} \cdot T_m$. The maximum electrical power output using CPM is given by ($P = Q_{in} - Q_{out}$),

$$P_{\max} = \alpha^2 \frac{\Delta T^2}{4\rho L} A \quad (47)$$

where $\alpha^2\sigma$ is called the thermoelectric power factor. The constant property values α , σ and κ have to be obtained from the temperature dependent TE data by averaging. The following are the most common averaging methods currently in practice [3, 12, 14, 15] – here, p indicates any of the three thermoelectric properties α , σ and κ .

1. Temperature average (TA_v): $p_{\text{TA}v} = \frac{1}{\Delta T} \int_{T_c}^{T_h} p(T) dT,$

also applied for averaging zT : $(zT)_{\text{TA}v} = \frac{1}{\Delta T} \int_{T_c}^{T_h} z(T)T dT$

2. Function value at mean temperature T_m (FMT) (i.e., zT_m): $p_{T_m} = p(T_m)$

3. Mean of the function values at the boundary temperatures (MVBT):

$$p_m = \frac{p(T_h)+p(T_c)}{2} = \frac{p_h+p_c}{2}$$

4. Weighted average introduced by Ioffe (IWA_v): $p_{\text{I}w\text{av}} = \frac{1}{\ln(T_h/T_c)} \int_{T_c}^{T_h} \frac{p(T)}{T} dT$

Assuming a continuous curve of a temperature dependence $p(T)$ which can be represented by an appropriate fit to experimental data points, the above averages can be numerically calculated. Since resistances (but not conductances) add up in series, for finding the integral average value for κ , $1/\kappa(T)$ was used. Likewise, the electrical resistivity ρ is averaged to obtain the CPM value of $\rho(T)$. Figure 3-2a shows the constant material property values obtained from the averaging techniques 1–4 (above) along with the temperature dependent data for an n-type $\text{Mg}_2(\text{Si},\text{Sn})$ sample [34]. Third order polynomial fits were used for this material to approximate the temperature curves of all properties. For such a material with nearly linear T dependence, all the averages are located close together. For a material with strongly temperature dependent properties like the p-type $\text{Mg}_2(\text{Si},\text{Sn})$ shown in Figure

3-2b, the choice of an appropriate average is not straightforward as can be seen from the figure. 5th order polynomial fits were used for this material.

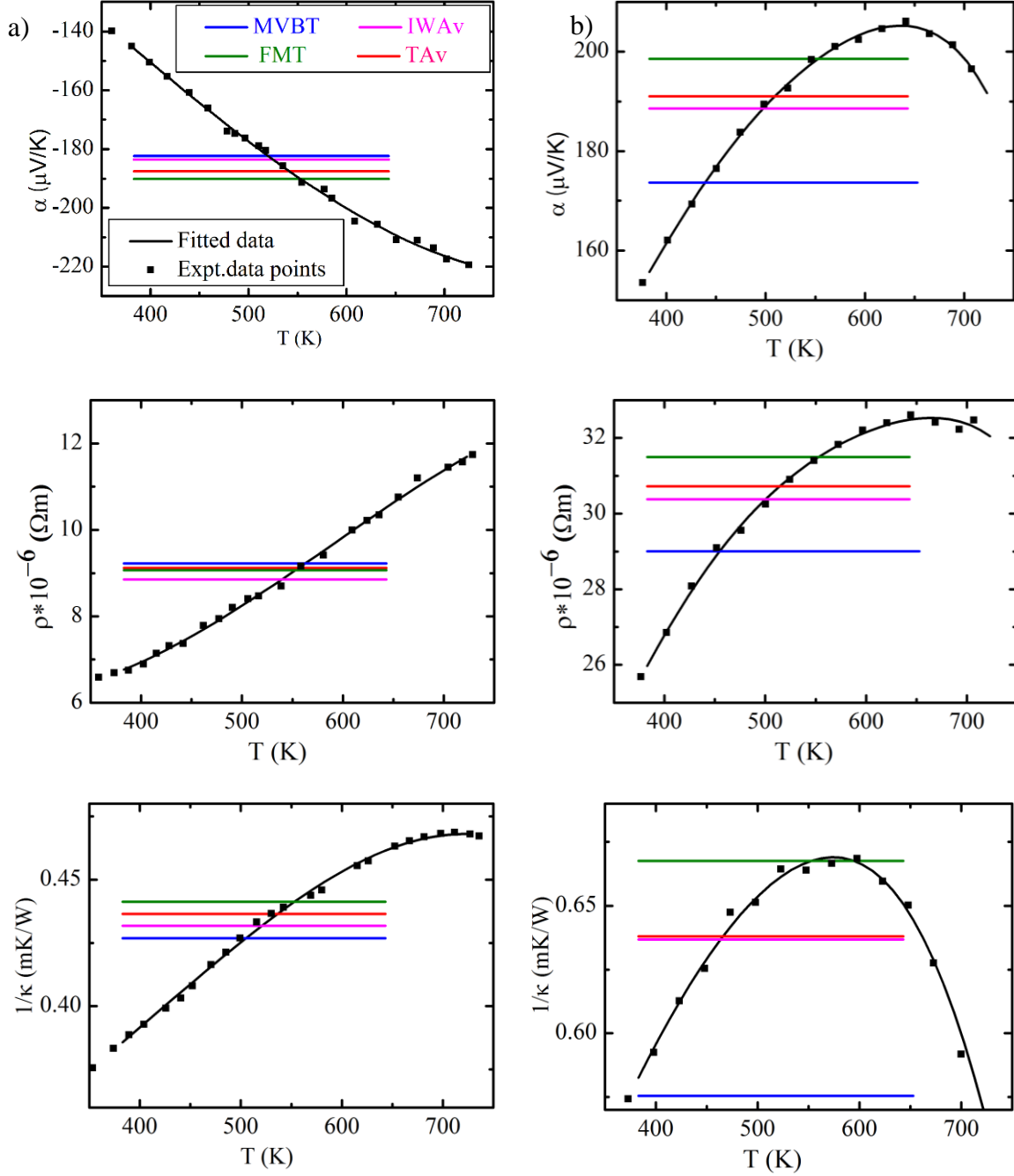


Figure 3-2: Graphical representation of different averages along with the T -dependent material data for a) n-type $\text{Mg}_2(\text{Si},\text{Sn})$ [34] and b) p-type $\text{Mg}_2(\text{Si},\text{Sn})$ [35]. The legend for all the graphs is given on the top left diagram. $T_c = 383 \text{ K}$ and $T_h = 723 \text{ K}$.

By calculating z for each of the above averaging methods from the individually averaged properties (except for the $(zT)_{\text{TAV}}$ case where zT curve is directly averaged) for different material classes, the maximum efficiency using CPM formulation (Eq. 46) was calculated. The

material data were taken from literature [34-37] (given in Appendix A). Figure 3-3 shows a comparison of the maximum efficiency calculated using the CPM formulation, with the exact results calculated using a Finite Element Method (calculated using Ansys 17.0 with a converged mesh size). As can be seen, none of the above considered averages are consistent in predicting the exact performance (Figure 3-3a). TAV – considered to be the best averaging technique so far [2] – could involve an error as high as 5-16% for strongly temperature dependent materials as seen. Moreover, there is no consistency in over-prediction or under-estimation of performance with different averaging methods except that TAV and $TAV(zT)$ seem to always overestimate efficiency. In order to overcome this, a combination of spatial averages for resistivities and TAV for Seebeck coefficient was studied as these are physically closest to Ioffe’s definition (Eq.(45)) i.e, $SpAv$ of ρ and $1/\kappa$ and TAV of α are the physically correct representations of the device parameters R_{in} , K and α , which Ioffe’s derivation of TE device performance is based upon.

The spatial average of a temperature dependent quantity p [3, 24, 29] is given by

$$p_{SpAv} = \frac{1}{L} \int_0^L p(T(x)) dx . \quad (48)$$

Since resistances add spatially, spatial averaging is physically appropriate for thermal and electrical resistivities. Hence, as can be seen from Figure 3-3b, performance prediction is within an error of 1.5%, much better than any of the other averaging methods. However, calculation of the spatial averages requires knowledge of the exact temperature profile $T(x)$. The results shown here are calculated with the temperature profiles corresponding to the optimum j in the temperature dependent case, obtained with FEM (Ansys 17.0) which is again time-consuming. j_{opt} is obtained by calculating η for current densities in the range of the CPM j_{opt} (calculated using TAV), for the temperature dependent case, fitting a polynomial for η and finding the j corresponding to the maximum η (the point where $\frac{d\eta}{dj}$ becomes zero). In order to find $T(x)$ quickly, an intuitive way of obtaining the temperature profile through numerical integration is presented in Appendix B. The T profile is obtained iteratively by integration using a linear T profile as a starting solution.

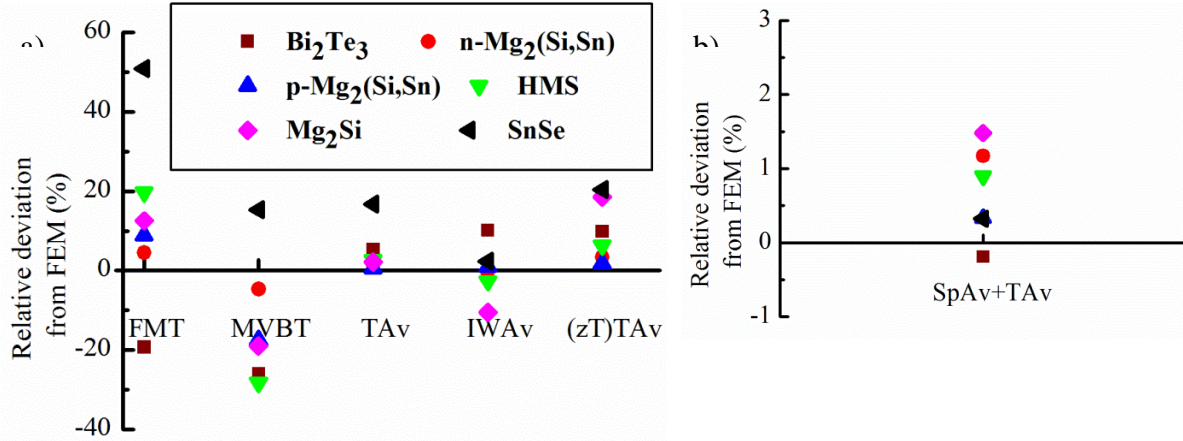


Figure 3-3: Comparison of maximum efficiency calculated using different averages in CPM formulation (Eq.(46)): a) FMT, MVBT, TAv, IWA v and (zT)TAv and b) SpAv for resistivities and TAv for Seebeck coefficient, as a comparison with FEM results for six representative TE materials.

3.4 Discussion

3.4.1 Influence of temperature dependence of material properties

In thermoelectrics, the temperature profile plays a significant role in reliably predicting the performance parameters as outlined in the introduction. Each term in Eq. (44) corresponds to the influence of one out of the three main thermoelectric properties $\kappa(T)$, $\rho(T)$ and $\alpha(T)$ in the heat balance *i. e.*,

- Fourier heat flow along the leg due to the applied ΔT between the hot and cold sides which leads to a significant bow of the temperature profile if the thermal conductivity varies with temperature,
- Joule heat release due to internal resistance $\rho(x)j^2$ which is locally distributed along the length x of the TE leg, and
- similarly, Thomson heat due to the T dependence of the Seebeck coefficient $\alpha(T)$ amounting to $jT \frac{d\alpha}{dT} \frac{dT}{dx}$ (which is physically a distributed Peltier effect due to the temperature gradient and the temperature dependence of the Seebeck coefficient) which causes a locally distributed source or sink of heat along x .

Two main aspects governing the curvature of the T profile in a real case are local heat generation/absorption (due to Joule and Thomson effects) and heat redistribution by conduction (obeying Fourier's law), both depending on the temperature dependence of the material

properties ($\rho(T)$, $\alpha(T)$, and $\kappa(T)$). The local Joule heat and Thomson heat that are generated at each point are being transported by Fourier conduction, each making up an individual contribution to the bow of the temperature profile. According to the magnitude of current passing through the TE leg, the temperature profile will vary due to the current-dependent contributions from Joule and Thomson heat. Hence, the material properties $p(T(x))$, vary locally according to the $T(x)$ for each current.

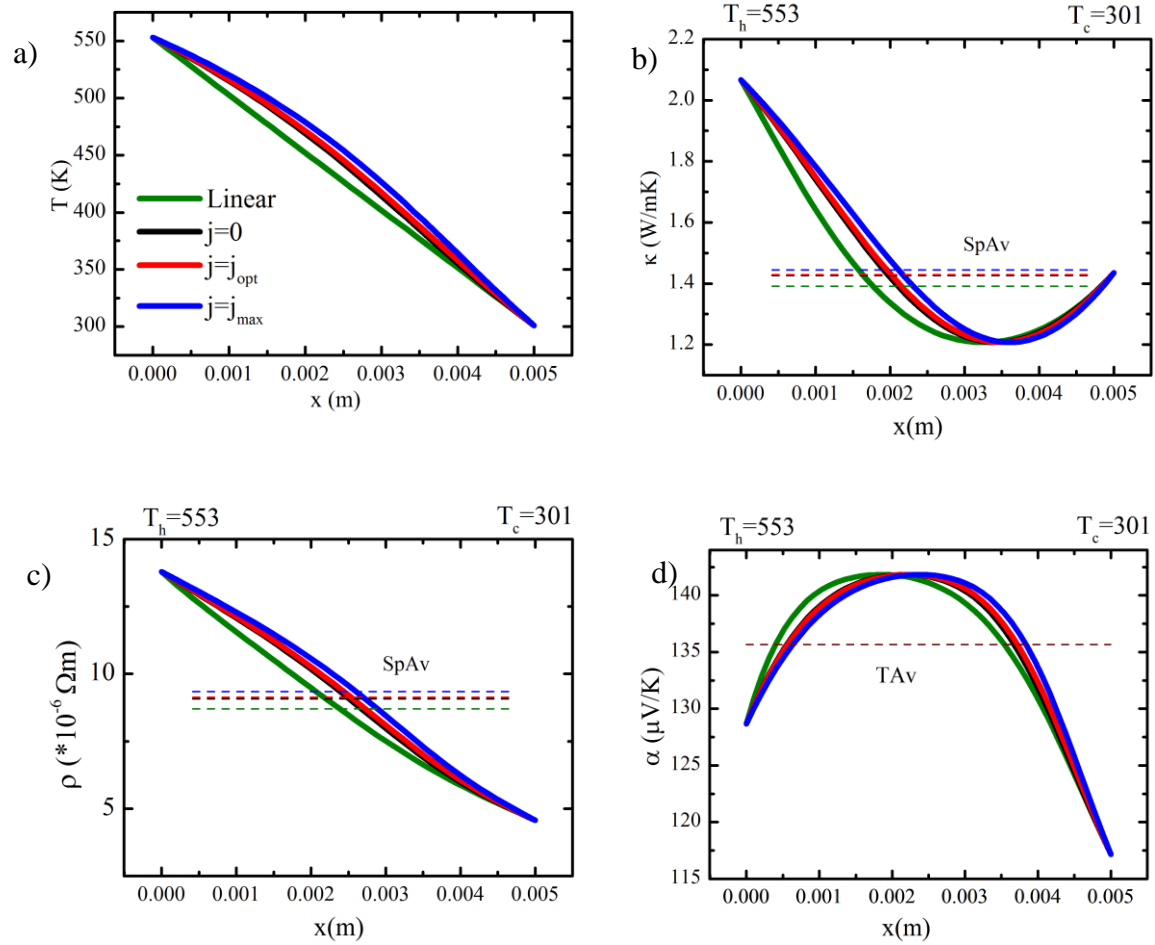


Figure 3-4: a) Temperature profiles and the corresponding variation of the TE properties b) Thermal conductivity c) Electrical resistivity d) Seebeck coefficient, along the TE leg for p-type Bi₂Te₃. Spatial averages for the resistivities and temperature average for the Seebeck coefficient are shown as horizontal dashed lines.

For visualization, the temperature profiles and the corresponding material property profiles $p(x)$ for different current flow cases (open circuit, j_{opt} and j_{max}) in p-type Bi₂Te₃ are shown in Figure 3-4. Here, j_{max} indicates the maximum current density at which the output voltage

vanishes and no more thermoelectric power output is obtained, *i.e.*, when $V_o = R_{in}I$. The spatial averages (for resistivities) and the temperature average of the Seebeck coefficient which represent effective constant material properties are indicated as horizontal dashed lines.

The spatial average for a linear T profile is the same as the temperature average. Hence, the difference between TAv and SpAv is illustrated by comparing the green (lowest, in our example) dashed lines to the other ones, consequently leading to different performance predictions as seen in Figure 3-3.

As can be seen for this material, for the $j = 0$ case the temperature profile is significantly bent compared to the linear T profile. This implies that the temperature dependence of $\kappa(T)$ significantly contributes to the bending of the temperature profile in this material and for this particular temperature range. Since Joule and Thomson heat contribute only slightly to the bending of T profile, the red and blue curves (corresponding to Joule and Thomson heat respectively) are bent only slightly further. This can be verified by visualizing the partial contributions to the T profile (see integration method in Appendix B). By considering the terms corresponding to $\kappa(T)$, Joule heat and Thomson heat separately and equating to $\kappa(T) \frac{\partial^2 T}{\partial x^2}$, the temperature profiles corresponding to the individual contribution are obtained by double integration. The exact $\kappa(x)$, $\rho(x)$ and $\alpha(x)$ at j_{opt} were used.

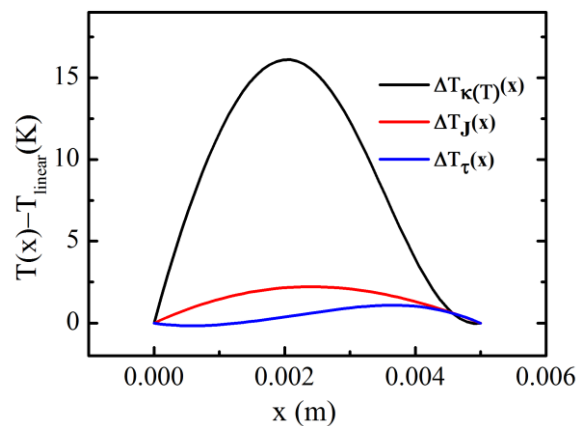


Figure 3-5: Partial contributions to the bending of the temperature profile for p-type Bi_2Te_3 . $\Delta T_{\kappa(T)}(x)$, $\Delta T_{\tau}(x)$ and $\Delta T_J(x)$ indicate the contributions due to the T dependence of the thermal conductivity, Thomson heat and Joule heat, respectively. For better readability, the linear part of the temperature profile has been subtracted here.

Figure 3-5 shows the individual contributions to the deviation from a linear T profile for p-type Bi_2Te_3 at optimum current (maximum efficiency operation). The results are in accordance with

the spatial profiles of the temperature dependent material properties (Figure 3-4). The contribution due to non-constancy of $\kappa(T)$ is positive (T profile bending above the linear T profile) since κ is higher at the hot side than at the cold side. Joule and Thomson heat generated (or absorbed) are carried away from their points of generation (or towards their locations of absorption) forming partial T gradients which overlay the open loop temperature profile. Thomson heat, as depends on the slope of the $\alpha(T)$ curve, is negative (will be absorbed) at the warmer section of the leg, becomes zero at the α peak and is released in the colder part as can be read from the blue curve in Figure 3-5.

3.4.2 Insight into the discrepancy with CPM

In the CPM, Eq. (44) reduces to

$$\kappa \frac{d^2 T}{dx^2} = -\rho j^2 \quad (49)$$

giving a temperature profile as

$$T(x) = T_h + (T_c - T_h) \frac{x}{L} + \frac{\rho j^2}{2\kappa} x(L - x) \quad (50)$$

which consists only of the linear part $T_h + (T_c - T_h) \frac{x}{L}$ due to Fourier heat assuming a constant κ and the parabolic part $\frac{\rho j^2}{2\kappa} x(L - x)$ due to Joule heat [2], neglecting the actual bending due to $\kappa(T)$. For p-type Bi_2Te_3 , a comparison of the actual T profile (with temperature dependent material data as input) to the CPM T profile (Eq. (50) using spatially averaged ρ and κ) can be seen in Figure 3-6 at $j = j_{\text{opt}}$, where clearly the CPM temperature profile is quite close to a linear curve but far from the actual T profile obtained by FEM.

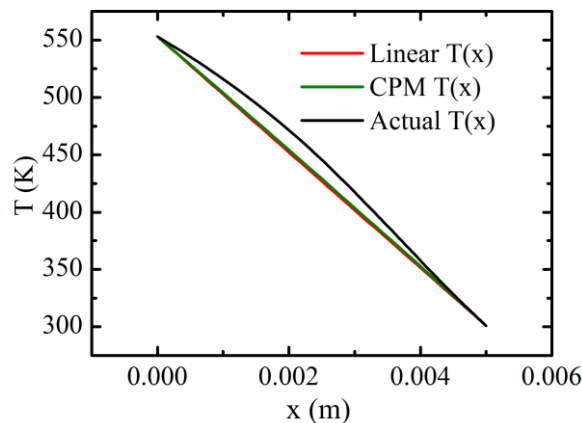


Figure 3-6: Linear, CPM and the actual temperature profiles for p-type Bi_2Te_3 at optimum current.

The maximum efficiency formulation by CPM (Eq. (46)) is based on the heat balance at the hot and cold sides (Eq. (45)) in which a linear T profile is assumed for the contribution from average Fourier heat flow, see Eq.(50). In the real case involving the temperature dependence of the material properties, the temperature profile due to $\kappa(T)$ is quite different from a linear one and hence κ_h and κ_c and the corresponding $\frac{dT}{dx}$ are considered to find the heat input or output as in Eq. (43). On a first glance, it could be expected that this might lead to significant error of an efficiency estimate in CPM. However, this is not the case because the temperature profile due to $\kappa(T)$, defined as a partial profile, does not involve any additional source of heat but rather a locally modified T gradient as a response to the local variation of κ together with an unchanged constant transmitted Fourier heat flow of the amount $\frac{K\Delta T}{L}$. Overall Fourier heat flow is formed from the net Fourier heat transfer related to the thermal conductance K plus smaller locally varying Fourier heat flow contributions to balance the internally released or absorbed Joule heat plus Thomson heat respectively. In the SpAv+TA_v case, the appropriate amounts of pure Fourier heat input and output due to the transferred Fourier heat are calculated, due to spatial averaging of κ . As the constant κ computed using SpAv exactly represents the true thermal conductance (since spatial averaging incorporates the exact temperature distribution), it compensates for not considering different $\kappa(x)$ and the corresponding $\frac{dT}{dx}$ at the hot and cold sides. With that, the replacement of the real Fourier heat flow by $K\Delta T$ in the CPM case is complete and exact.

Likewise, overall Joule heat is correctly estimated by SpAv of ρ ; however, its distribution to both sides is not anymore ideally symmetric to both sides as in CPM, but is biased by both the asymmetric release due to spatial dependence of ρ and the asymmetric conduction of (even symmetrically) released Joule heat towards both ends due to spatial asymmetry of κ over the element; with that, Q_{in} and the efficiency calculated by the CPM formula can be slightly inaccurate. Additionally, neglecting Thomson heat in CPM is mainly compensated by considering an averaged α in the Peltier heat input and output calculation, instead of considering α_h and α_c separately. It would be exactly compensated if Thomson heat was symmetrically released to both ends, i.e. in a situation with linear $\alpha(x)$ and symmetric $\kappa(x)$. In any case, the overall Peltier plus Thomson heat balance is correct; merely the location of its appearance is shifted from the interior of the leg (as Thomson heat, in the real case) to the junctions (as Peltier heat, for CPM). However, also here, like for the Joule heat, asymmetric

appearance or transmission of Thomson heat may lead to a slightly shifted distribution of the overall unchanged Thomson heat among both ends of the leg in the real case and may thus contribute to the remaining inaccuracy of the CPM result. We note that due to this almost complete compensation, SpAv+TA_v averaging provides quite accurate results in efficiency estimation although the underlying CPM temperature profile might be quite far from reality. The remaining 1–1.5% deviation of SpAv+TA_v averaging (CPM) from FEM is due to the above mentioned asymmetry[3, 5, 24, 38] of heat generation and distribution due to temperature dependent material properties, which is disregarded by CPM.

According to energy balance, in a temperature dependent case, Thomson heat would be $I(\alpha_h T_h - \alpha_c T_c - \alpha_{TA_v} \Delta T)$ (Thomson heat being the distributed Peltier heat). The difference between Peltier heat balance and thermoelectrically converted electrical power is dissipated (or delivered) across the element as Thomson heat -depending on temperature dependence and current direction. The Thomson part is always smaller than the according Peltier heat. As absorbed Peltier heat will transform into Thomson heat plus electric power, the released Thomson heat is lowered where the power production is higher. Thus, the compensation of the additionally absorbed Peltier heat at the hot side, compared to the CPM case is incomplete by the amount of produced electrical power in the warmer half of the sample above the average and the error in CPM would be proportional to this.

In summary, unless spatial averages are used, conventional averaging methods (like TA_v, FMT, MVBT, IWA_v) and any correction factors based on just the Thomson and Joule effect [12, 31] that could be added to CPM, would be insufficient to provide exact results for all material cases and/or for all temperature ranges. This is also evident from the results of Ryu *et al.* [24], where accurate performance estimation is obtained using spatial averages. Additionally, the explained importance of the effect of temperature profile due to $\kappa(T)$ can be seen from the accuracy of ‘One-shot approximation’ in [24] where $j = 0$ T profiles are used. This can be further emphasized by the $j = 0$ temperature profiles (where only $\kappa(T)$ contributes to the T profile shape) of the various materials under consideration here as shown in Figure 3-7. For a better comparison, normalized T profiles are plotted. For materials with stronger dependence of $\kappa(T)$ such as in SnSe and p-type Bi₂Te₃ the TA_v fails significantly in predicting the efficiency (see Figure 3-3a, 17% deviation for SnSe and 5.3% for Bi₂Te₃), while for materials with not much varying $\kappa(T)$ such as HMS (2.6 %), Mg₂Si (2.2 %), n-type and p-type

Mg₂(Si,Sn) (1.34 % and 0.48 % respectively), the TAv or IWA_v predict the performance better (Figure 3-3a).

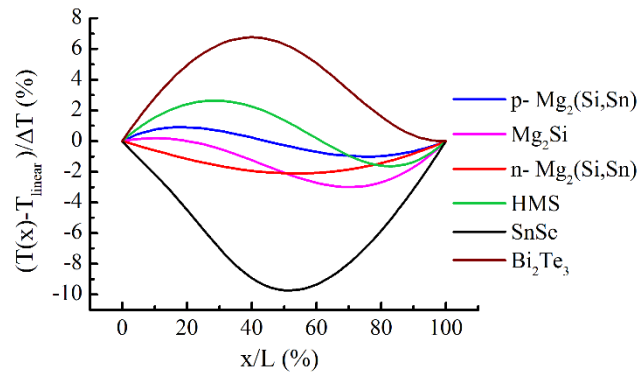


Figure 3-7: Normalised temperature profiles omitting the linear part ($T(x) - T_{lin}$) at zero current for Bi₂Te₃, SnSe, p-type Mg₂(Si,Sn), Mg₂Si, n-type Mg₂(Si,Sn) and HMS.

According to Tuley and Simpson [13], the average zT is more important for higher efficiency than the peak zT . For typical TE materials the best thermoelectric properties are obtained in the region where minority charge carrier effects start to become relevant. This leads to significant deviation of the thermoelectric properties vs. temperature curves from linearity and hence linear assumptions of T profiles or material properties [24,25] do not hold well anymore. This also implies that the use of temperature averages is not well justified anymore. As for the typical application scenarios, where this temperature region is included or even focused on, the difference between SpAv and TAv is relatively large, see e.g. the p-type Bi₂Te₃ case.

3.5 Conclusion

Efficiency estimation by CPM formulae shows that a combination of temperature average for Seebeck and spatial averages for thermal and electrical resistivities, as these represent thermovoltage, electrical resistance and thermal conductance of the leg physically appropriately, predicts the performance with less error compared to other modes of averaging proposed in the past. The remaining error (0.5–1.5%) is due to the asymmetry in heat generation and transport which is not accounted for in the CPM formulation. A detailed explanation of how the assumption of constant material properties affects the performance calculation and when and why CPM works well or fails was provided. By studying temperature profiles for a representative spectrum of dissimilar materials, a long standing issue of identifying the material specific uncertainty with CPM has been made clear. The $\kappa(T)$ dependence significantly contributes to the bending of the T profile and hence, unless T profiles are taken into account

while averaging (i.e. correct spatial averages are involved), the effective resistance values (electrical and thermal) would not be physically appropriate. Therefore, temperature averages which have always been considered to be the easiest method of averaging fail significantly for materials with strongly T dependent thermal conductivity. Neglect of Thomson heat in CPM is mostly compensated by a shift of the Peltier heat calculated at the hot and cold sides, keeping the overall balance of Peltier plus Thomson heat in the leg unchanged. Hence it is not a major issue in CPM as has been considered by previous literatures. Finally, it has to be kept in mind that even though CPM may provide quite accurate performance values with proper choice of averaged properties, the corresponding temperature profile might be inaccurate.

For spatial averages, the exact temperature profile is needed. A fast and simple way of obtaining the temperature profile based on integration by standard table calculation software was presented. By solving the 1D heat balance equation by an iterative numerical procedure, an estimate of individual contributions to the bending of the temperature profile is directly obtained. Visualizing the weight of individual contributions to the bow of the T profile can give an idea to experimentalists how to tune the thermoelectric material properties for better efficiency by manipulating the different heat contributions and their distribution (Joule, Thomson and Fourier heat).

Acknowledgements

We would like to gratefully acknowledge the endorsement from the DLR Executive Board Member for Space Research and Technology and the financial support from the Young Research Group Leader Program. PP would like to acknowledge the German Academic Exchange Service, DAAD (Fellowship No. 247/2017) for financial support.

APPENDIX

A. Material data and boundary conditions

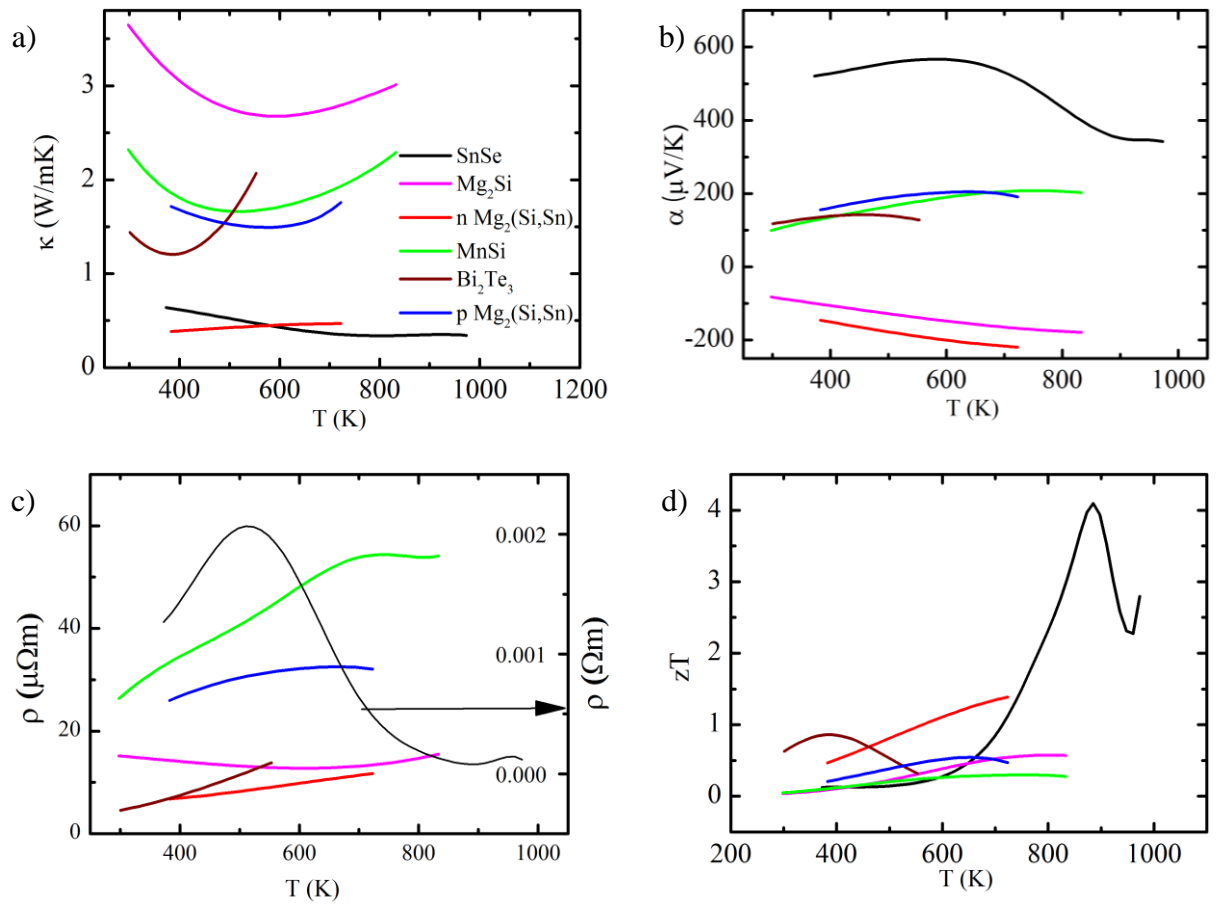


Figure A.1: Temperature dependent thermoelectric material properties of representative material classes
a) Thermal conductivity b) Seebeck coefficient c) Electrical resistivity d) the corresponding zT . Since SnSe has high resistivity the scale for it is given on the right y axis (indicated by an arrow).

Table A.1: Polynomial fit order used for material properties along with the temperature range of analysis for all materials of Fig. A.1

Material	Fitted Polynomial degree	Temperature of analysis
p-Mg₂(Si,Sn)	5	723 K to 383 K
n-Mg₂(Si,Sn)	3	723 K to 383 K
HMS	5	833 K to 298 K
Mg₂Si	3	833 K to 298 K

p- Bi₂Te₃	3	553 K to 301 K
SnSe	9	973 K to 373 K

B. Calculation of the exact temperature profile through integration

The solution procedure is based on the fact that (T) , Joule heat and Thomson heat can be considered as small perturbations contributing to the non-linearity of the temperature profile.

For a slender TEG leg or suitable (symmetrical) boundary conditions (BCs), with no convection or radiation losses, heat flow can be considered to be one-dimensional (1D) which shall be assumed in the following, and the thermoelectric heat balance equation (Eq. 44) in 1D is written as

$$\kappa(T) \frac{\partial^2 T}{\partial x^2} + \frac{d\kappa}{dT} \left(\frac{\partial T}{\partial x}\right)^2 - jT \frac{d\alpha}{dT} \frac{\partial T}{\partial x} = -\rho(T)j^2 \quad (\text{B.1})$$

Radiation and convection effects are relevant when a leg is operated at high temperature and open atmosphere and this will reduce the performance of the device significantly. In principle, they can be incorporated mathematically [39-41], although not mathematically strictly in a 1D model. However, these effects can be practically minimized by suitable thermal damping [5] and vacuum conditions, and so they are not considered here.

Assuming that the TE leg is divided mathematically into a large number of segments along the heat flow direction, the individual contributions to the thermal energy balance from each section of a length dx can be calculated according to Eq. (B.1) when the T -dependent data is known, provided that an approximated temperature profile $T(x)$ is known initially to deduce its derivatives. In our study, the solution is obtained by a self-consistent iterative procedure starting with a fair initial guess for $T(x)$. Hence, the calculation begins with a simple linear $T(x)$ and since any material property $p(x) = p(T(x))$, $p(x)$ is equivalent in shape to $p(T)$ for the starting iteration. At zero current, Joule heat and Thomson heat are absent and Eq.(B.1) reduces to

$$\frac{d}{dx} \left(-\kappa(x) \frac{dT}{dx} \right) = 0 \quad (\text{B.2})$$

Eq. (B.2) indicates that the divergence of Fourier heat flux $q_F (= -\kappa(x) \frac{dT}{dx})$ is zero, implying that no thermal power is converted into electrical power inside the leg and no irreversible or reversible heat is absorbed or released at zero current. The total Fourier heat flux q_F initially

can be approximated as $\kappa_{\text{eff}}\Delta T/L$ (κ_{eff} can be obtained as the reciprocal spatial average of $1/\kappa(T)$ and $\Delta T = T_h - T_c$). The temperature profile $T(x)$ can then be found from Eq. (B.2) by spatially integrating $q_F = \kappa_{\text{eff}}\Delta T/L$, *i.e.*,

$$T(x)_{j=0} = -\kappa_{\text{eff}}\Delta T/L \int_0^x \frac{dx}{\kappa(x)} + C \quad (\text{B.3})$$

Here, the constant of integration C is obtained with the boundary condition $T(x=0) = T_h$. With the $T(x)$ thus calculated, the $\kappa(T(x))$ for the next iteration is obtained and the calculation of Eq. (B.3) is repeated until the solution converges. By this, we have calculated the temperature profile for the open circuit condition ($j = 0$) which is a profile that is bowed only due to κ dependence on T .

When connected to an external load or current supply *i.e.*, when current flows through the TE leg, the open circuit temperature profile is taken as a first approximation for starting the iterative solution. Rewriting Eq.(B.1) as,

$$\kappa(T) \frac{\partial^2 T}{\partial x^2} = -\frac{d\kappa}{dT} \left(\frac{\partial T}{\partial x} \right)^2 + jT \frac{d\alpha}{dT} \frac{\partial T}{\partial x} - \rho(T)j^2, \quad (\text{B.4})$$

the right-hand side of Eq. (B.4) is calculated using the temperature profile from the previous step ($T(x)_{j=0}$ for the first step and the $T(x)$ obtained in the subsequent steps, respectively). The left side is solved by integrating spatially twice and solving for the two integration constants C_1 and C_2 using the BC $T(x=0) = T_h$ and $T(x=L) = T_c$. In summary, let

$$f(x) = -\frac{d\kappa}{dT} \left(\frac{\partial T}{\partial x} \right)^2 + jT \frac{d\alpha}{dT} \frac{\partial T}{\partial x} - \rho(T)j^2 \quad (\text{B.5})$$

$$\text{Hence, } \kappa(T(x)) \frac{\partial^2 T}{\partial x^2} = f(x),$$

$$\text{Therefore, } T(x)_{j \neq 0} = \int_0^x \int_0^x \frac{f(x)dx}{\kappa(x)} dx + C_1 + C_2$$

This process is repeated until convergence. By following the above procedure, T profiles have been calculated for some of the materials that were used in the CPM section above (Section 3.3.1). Figure B.1 shows the calculated temperature profiles for a TE leg length of 5 mm at $j = 0$ (a and c), $j = j_{\text{opt}}$ (optimum current; Fig. 3-4b and d) for p-type Bi_2Te_3 and for p-type SnSe . j_{opt} is obtained by calculating the efficiency for different current densities j , fitting a polynomial for η vs j and finding the point where $\frac{d\eta}{dj}$ becomes zero; *i.e.*, the current density

where the efficiency is maximum. Since the TE properties of SnSe have a complex temperature dependence, 8th and 9th order polynomial fits were used for fitting the material properties.

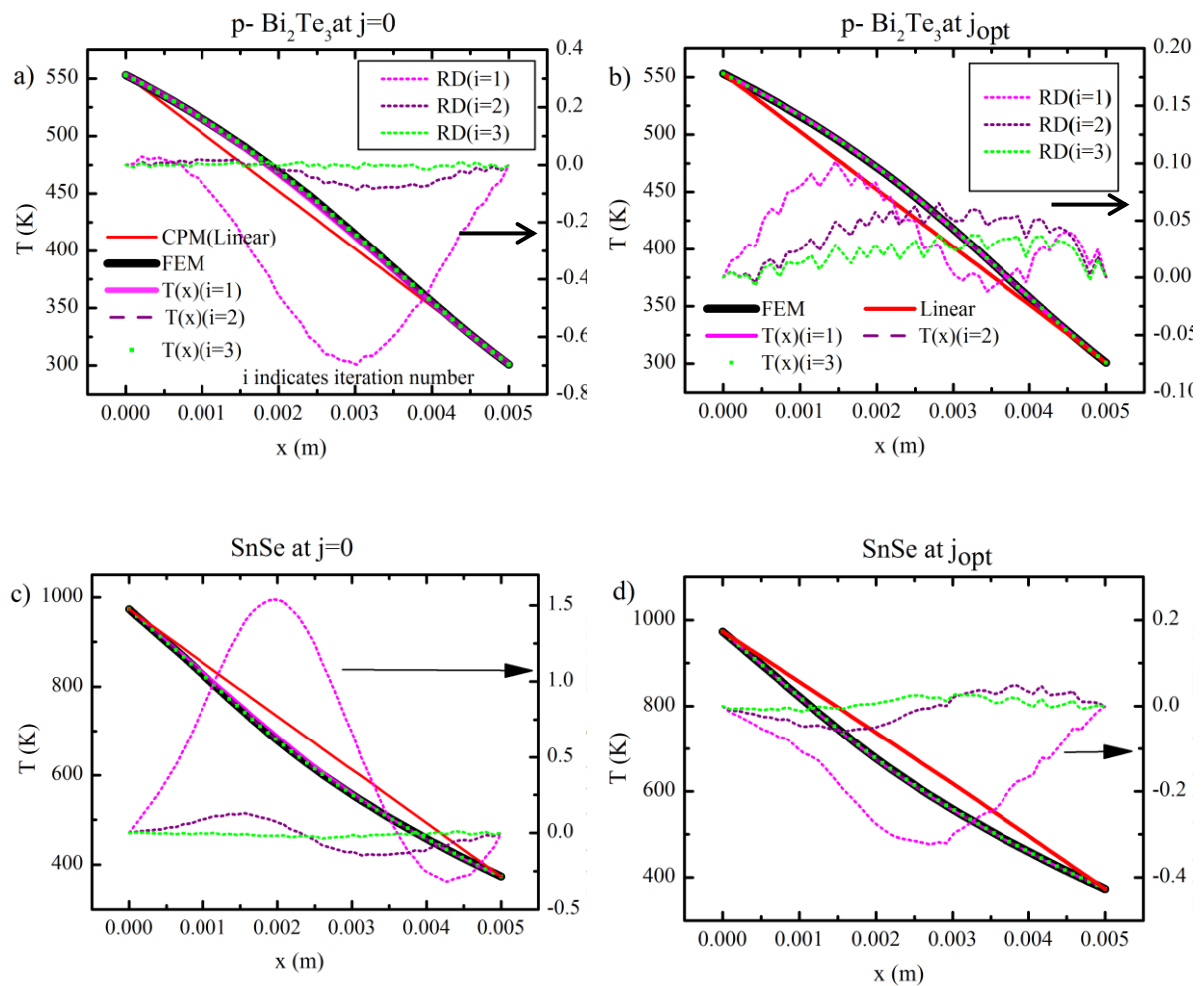


Figure B.1: Calculated T profiles for p-type Bi_2Te_3 at a) $j = 0$ and b) $j = j_{\text{opt}}$ and for p-type SnSe (legend same as that of Bi_2Te_3) at c) $j = 0$ and d) $j = j_{\text{opt}}$ for the first three iterations. The dashed lines represent the relative difference between FEM T profile and the T profiles calculated using the iterative method.

Conventionally, perturbation solution is obtained using Taylor or Maclaurin series [25-27] expansion and this very fact makes the solution convergent. Consequently, these traditional methods require parameterization and complicated analytical computation [38]. A brief mathematical description on the application of perturbation theory specifically to thermoelectrics can be found in Wee [25]. In this work, Wee assumes 2nd order polynomials for a particular material case and obtains the solution using series expansion. On a similar work, Ju *et al.* [26] derived analytical expressions for the temperature profile for another particular material case assuming parabolic functions for material properties. Later, Zhang [38] provided

a more generalized solution based on the Homotopy perturbation method in an effort to signify the importance of temperature dependence of material properties. Recently, Marchenko [27] provided a comparison between using quadratic and linear approximations in perturbation theory.

In our case, the convergence of the solution is ensured by spatial integration, which is mathematically equivalent to summing up the individual terms of the series. In this study, integration was done using trapezoidal rule in-built in the software Origin 8.5.1. In perturbation theory, the closer the starting function, the faster the convergence of the solution. Hence, the current method which inputs the temperature profile from previous step is convergent in two or three iterations as can be seen from the very low relative deviation (right side y axis) of the third iteration from the exact T profile (FEM) even for strongly T dependent materials as in Figure B.1. In doing so, the calculation times are reduced tremendously compared to FEM and individual heat contributions can be easily visualized by integrating the corresponding terms in the heat balance equation.

References for chapter 3 (paper 1)

1. Snyder, G.J. and E.S. Toberer, *Complex thermoelectric materials*, in *Materials For Sustainable Energy: A Collection of Peer-Reviewed Research and Review Articles from Nature Publishing Group*. 2011, World Scientific. p. 101-110.
2. Rowe, D.M., *Thermoelectrics handbook: macro to nano*. 2005, CRC press.
3. A.F. Ioffe. *Semiconductor thermoelements and thermoelectric cooling*. London, Infosearch, ltd., 1957.
4. Antonova, E.E. and D.C. Looman. *Finite elements for thermoelectric device analysis in ANSYS*. in *Thermoelectrics, 2005. ICT 2005. 24th International Conference on*. 2005. IEEE.
5. Goupil, C., *Continuum theory and modeling of thermoelectric elements*. 2015: John Wiley & Sons.
6. Kim, C.N., *Development of a numerical method for the performance analysis of thermoelectric generators with thermal and electric contact resistance*. Applied Thermal Engineering, 2018. **130**: p. 408-417.
7. Hogan, T. and T. Shih, *Modeling and characterization of power generation modules based on bulk materials*. Thermoelectrics Handbook: Macro to Nano, 2006: p. 12.1-12.23.
8. Oliveira, K.S., R.P. Cardoso, and C.J. Hermes, *Two-Dimensional Modeling of Thermoelectric Cells*. 2014.
9. Sherman, B., R. Heikes, and R. Ure Jr, *Calculation of efficiency of thermoelectric devices*. Journal of Applied Physics, 1960. **31**(1): p. 1-16.
10. Brandt, J.A., *Solutions to the differential equations describing the temperature distribution, thermal efficiency, and power output of a thermoelectric element with variable properties and cross sectional area*. Advanced Energy Conversion, 1962. **2**: p. 219-230.
11. Lee, H., et al., *Modeling and analysis of the effect of thermal losses on thermoelectric generator performance using effective properties*. Applied Energy, 2018. **211**: p. 987-996.
12. Kim, H.S., et al., *Relationship between thermoelectric figure of merit and energy conversion efficiency*. Proceedings of the National Academy of Sciences, 2015. **112**(27): p. 8205-8210.
13. Tuley, R. and K. Simpson, *ZT Optimization: An Application Focus*. Materials, 2017. **10**(3): p. 309.
14. Armstrong, H., et al., *Estimating Energy Conversion Efficiency of Thermoelectric Materials: Constant Property Versus Average Property Models*. Journal of Electronic Materials, 2017. **46**(1): p. 6-13.
15. Lau, P.G. and R.J. Buist. *Calculation of thermoelectric power generation performance using finite element analysis*. in *Thermoelectrics, 1997. Proceedings ICT'97. XVI International Conference on*. 1997. IEEE.

16. Mahan, G., *Inhomogeneous thermoelectrics*. Journal of Applied Physics, 1991. **70**(8): p. 4551-4554.
17. Fraisse, G., et al., *Comparison of different modeling approaches for thermoelectric elements*. Energy conversion and management, 2013. **65**: p. 351-356.
18. Chen, J., Z. Yan, and L. Wu, *The influence of Thomson effect on the maximum power output and maximum efficiency of a thermoelectric generator*. Journal of Applied Physics, 1996. **79**(11): p. 8823-8828.
19. Huang, M.-J., R.-H. Yen, and A.-B. Wang, *The influence of the Thomson effect on the performance of a thermoelectric cooler*. International Journal of Heat and Mass Transfer, 2005. **48**(2): p. 413-418.
20. Sandoz-Rosado, E.J., S.J. Weinstein, and R.J. Stevens, *On the Thomson effect in thermoelectric power devices*. International Journal of Thermal Sciences, 2013. **66**: p. 1-7.
21. Lee, H., *The Thomson effect and the ideal equation on thermoelectric coolers*. Energy, 2013. **56**: p. 61-69.
22. Yamashita, O., *Effect of linear temperature dependence of thermoelectric properties on energy conversion efficiency*. Energy conversion and management, 2008. **49**(11): p. 3163-3169.
23. Yamashita, O., *Effect of linear and non-linear components in the temperature dependences of thermoelectric properties on the cooling performance*. Applied Energy, 2009. **86**(9): p. 1746-1756.
24. Ryu, B., J. Chung, and S. Park, *Thermoelectric efficiency has three Degrees of Freedom*. arXiv preprint arXiv:1810.11148, 2018.
25. Wee, D., *Analysis of thermoelectric energy conversion efficiency with linear and nonlinear temperature dependence in material properties*. Energy conversion and management, 2011. **52**(12): p. 3383-3390.
26. Ju, C., et al., *Revisiting the temperature dependence in material properties and performance of thermoelectric materials*. Energy, 2017. **124**: p. 249-257.
27. Marchenko, O.V., *Performance modeling of thermoelectric devices by perturbation method*. International Journal of Thermal Sciences, 2018. **129**: p. 334-342.
28. Fraisse, G., et al., *Study of a thermoelement's behaviour through a modelling based on electrical analogy*. International Journal of Heat and Mass Transfer, 2010. **53**(17-18): p. 3503-3512.
29. Seifert, W., M. Ueltzen, and E. Müller, *One-dimensional modelling of thermoelectric cooling*. physica status solidi (a), 2002. **194**(1): p. 277-290.
30. Sunderland, J.E. and N.T. Burak, *The influence of the Thomson effect on the performance of a thermoelectric power generator*. Solid-State Electronics, 1964. **7**(6): p. 465-471.
31. Min, G., D.M. Rowe, and K. Kontostavlikis, *Thermoelectric figure-of-merit under large temperature differences*. Journal of Physics D: Applied Physics, 2004. **37**(8): p. 1301.

32. Kim, H.S., W. Liu, and Z. Ren, *The bridge between the materials and devices of thermoelectric power generators*. Energy & Environmental Science, 2017. **10**(1): p. 69-85.
33. Snyder, G.J. and T.S. Ursell, *Thermoelectric efficiency and compatibility*. Physical review letters, 2003. **91**(14): p. 148301.
34. Sankhla, A., et al., *Mechanical Alloying of Optimized Mg₂ (Si, Sn) Solid Solutions: Understanding Phase Evolution and Tuning Synthesis Parameters for Thermoelectric Applications*. ACS Applied Energy Materials, 2018. **1**(2): p. 531-542.
35. Kamila, H., et al., *Analyzing transport properties of p-type Mg₂Si–Mg₂Sn solid solutions: optimization of thermoelectric performance and insight into the electronic band structure*. Journal of Materials Chemistry A, 2019.
36. Kim, H.S., et al., *Design of segmented thermoelectric generator based on cost-effective and light-weight thermoelectric alloys*. Materials Science and Engineering: B, 2014. **185**: p. 45-52.
37. Zhao, L.-D., et al., *Ultralow thermal conductivity and high thermoelectric figure of merit in SnSe crystals*. Nature, 2014. **508**(7496): p. 373.
38. Zhang, T., *Effects of temperature-dependent material properties on temperature variation in a thermoelement*. Journal of Electronic Materials, 2015. **44**(10): p. 3612-3620.
39. Muto, A., et al., *Thermoelectric properties and efficiency measurements under large temperature differences*. Review of Scientific Instruments, 2009. **80**(9): p. 093901.
40. Meng, F., L. Chen, and F. Sun, *A numerical model and comparative investigation of a thermoelectric generator with multi-irreversibilities*. Energy, 2011. **36**(5): p. 3513-3522.
41. Li, T., et al., *Thermoelectric properties and performance of flexible reduced graphene oxide films up to 3,000 K*. Nature Energy, 2018. **3**(2): p. 148.

4 Discrepancies associated with the use of CPM (Publication 2)

This paper deals with discrepancies associated with the use of a CPM despite using the appropriate averaging technique. With the use of an entropy flow diagram based on $\alpha(T)$, it is explained that there is always a certain amount of Thomson heat unaccounted for in CPM. Additionally, an approximate correction for this uncompensated Thomson heat is suggested.

DOI: <https://doi.org/10.3390/e22101128>. This article was published on 4th October 2020 in Entropy journal (mdpi). Author contributions are specified in the published article as well as at the end of this thesis.

Article

Discrepancy between constant property model and temperature dependent material properties for performance estimation of thermoelectric generators

Prasanna Ponnusamy ^{1*}, Johannes deBoor ¹ and Eckhard Müller ^{1,2,*}

¹ German Aerospace Center (DLR), Institute of Materials Research, D-51170 Köln, Germany; Johannes.deBoor@dlr.de (J.dB)

² Justus Liebig University Gießen, Institute of Inorganic and Analytical Chemistry, D-35392 Gießen, Germany; e-mail@e-mail.com

* Correspondence: prasanna.ponnusamy@dlr.de (P.P); Tel.: +49 2203 601 3386; Eckhard.mueller@dlr.de (E.M); Tel.: +49 2203 601 3556

Received: date; Accepted: date; Published: date

Abstract: The efficiency of a thermoelectric (TE) generator for conversion of thermal energy into electrical energy can be easily but roughly estimated using a Constant Properties Model (CPM) developed by Ioffe. However, material properties are in general temperature (T) dependent and the CPM yields meaningful estimates only if physically appropriate averages, i.e. spatial averages for thermal and electrical resistivities and the temperature average (T_{AV}) for the Seebeck coefficient (α) are used. Even though the use of $\alpha_{T_{AV}}$ compensates for the absence of Thomson heat in CPM in the overall heat balance, we find that CPM still over-estimates performance (e.g. by up to 6% for PbTe) for many materials. The deviation originates from an asymmetric distribution of internally released Joule heat to either side of the TE leg and the distribution of internally released Thomson heat between the hot and cold side. The Thomson heat distribution differs from a complete compensation of the

according Peltier heat balance in CPM. Both effects are estimated quantitatively here, showing that both may reach the same order of magnitude but it varies from case to case, depending on the specific temperature characteristics of the thermoelectric properties, which one dominates. The role of the Thomson heat distribution is illustrated by a discussion of the transport entropy flow based on the $\alpha(T)$ plot. The changes in the lateral distribution of the internal heat lead to a difference in the heat input, of the optimum current and thus of the efficiency, respectively, of the CPM approximate from the real case, while the estimate of generated power at maximum efficiency remains less affected as it is bound to the deviation of the optimum current which is mostly $< 1\%$. This deviation can be corrected to a large extent by estimating the lateral Thomson heat distribution and the asymmetry of the Joule heat distribution. A simple guiding rule for the former is found.

Keywords: TEG performance, Device modeling, Temperature profile, Constant properties model, Fourier heat, Thomson heat, Joule heat.

4.1 Introduction

Thermoelectric generator (TEG) materials convert a certain fraction of the heat passed through them into useful electrical power, as the charge carriers (holes/electrons) absorb the thermal energy and move from the hot side to the cold side, carrying entropy [1, 2]. The transport entropy flux related to the convective heat transport is given by αj , with the Seebeck coefficient $\alpha(T)$ and current density j . Typically, a thermoelectric (TE) module consists of a series of pn leg pairs (thermocouples), electrically connected in series and thermally in parallel [3]. In steady-state, the exact performance of the TEG is obtained by solving the thermoelectric heat balance equation [4] for the temperature profile $T(x)$. In 1D, it reads

$$\kappa(T) \frac{\partial^2 T}{\partial x^2} + \frac{d\kappa}{dT} \left(\frac{\partial T}{\partial x} \right)^2 - jT \frac{d\alpha}{dT} \frac{\partial T}{\partial x} = -\rho(T) j^2, \quad (51)$$

where the thermal conductivity κ , the electrical resistivity ρ and α are the three main temperature dependent thermoelectric properties. Here, $\frac{\partial}{\partial x} \cdot \left\{ \kappa(T) \frac{\partial T}{\partial x} \right\} = \kappa(T) \frac{\partial^2 T}{\partial x^2} + \frac{d\kappa}{dT} \left(\frac{\partial T}{\partial x} \right)^2$ corresponds to the (negative) divergence of the Fourier heat flux, i.e. its local change; $jT \frac{d\alpha}{dT} \frac{\partial T}{\partial x}$ corresponds to the local Thomson heat absorption driven by the change of the convective entropy flux αj related to the temperature dependence of $\alpha(T)$, and $\rho(T) j^2$ corresponds to the local Joule heat dissipation. With a typical TE material, with $\kappa(T)$ falling with T and the amount of $\alpha(T)$ rising with T , Thomson heat will be released and Fourier heat flow will grow from hot to cold side along a TE leg in TEG operation, where the current flow is driven by the thermo-voltage generated by the leg. Eq. (51) is a second order non-linear partial differential equation, which can be solved using numerical methods like Finite Element Methods (FEM) [5, 6], Finite Volume Methods (FVM) [7-9] or Finite Difference Methods (FDM) [6]. However, these solution methods are costly and time consuming.

On the other hand, when assuming constant properties of the TE properties, an approximate solution can be found analytically as suggested by Ioffe [1]. This solution by the Constant Property Model (CPM) involves a discrepancy from exact results due to the underlying simplification. Moreover, the choice of the averaged constant properties to be obtained from the actual temperature dependent data is not straight-forward. As can be seen from Eq. (51), the Thomson heat vanishes when the Seebeck coefficient (and with that the convective entropy flux αj) remains constant. Various models on corrected CPM to compensate for this ‘missing Thomson heat’ [10-16] have been proposed. Meanwhile, Sandoz *et al.* [17] attempted to explain the use of the T -averaged Seebeck coefficient in predicting exact power in CPM mathematically, but did not recognise the importance of the asymmetry in heat distribution on the prediction of efficiency.

In a previous study [18], on the physically appropriate choice of averages in CPM we highlighted that spatial averages (SpAv) for resistivities (electrical and thermal) and temperature averaging (TA_v) for the Seebeck coefficient are essential for a meaningful CPM estimate. However, there is still a

remaining deviation due to unconsidered local redistribution of internal heat release or absorption and of thermal conduction in CPM which is linked to a change in the T profile $T(x)$ [1, 12, 18, 19]. Here, we will analyze the individual heat contributions exemplarily for six representative thermoelectric materials that we considered previously [18], plus PbTe [20] as this is one of the best TE materials in practice and shows an especially large deviation between CPM and exact results.

Initially, the effect of the T dependence of each of the TE properties, α , ρ and κ , leading to locally shifted heat release and transport over the TE element, for performance estimation is studied separately. Calculated maximum efficiency in the full temperature dependent case, η_{\max} , is compared with tailored model materials, in order to separate and quantify the individual contributions. Model materials are defined by setting one or two of the three TE properties constant at its respective average while keeping the other properties T -dependent. Next, we explain the physical origin of a relevant part of the discrepancy between CPM results and the real situation using a schematic plot of the convective entropy flux derived from a $\alpha(T)$ graph, alongside showing that the net Peltier/Thomson heat is correctly considered by CPM when appropriate temperature averaging is used for $\alpha(T)$. Marked areas in the entropy flux diagram quantify the exchange of Peltier and Thomson heat, and with that, a correction for the related deviation in CPM efficiency estimation, $d\eta_{\max} = \frac{\eta_{\max} - \eta_{\max}^{\text{CPM}}}{\eta_{\max}^{\text{CPM}}}$ is suggested and demonstrated.

4.2 Methods, results and discussion

4.2.1 Role of the T dependence of material properties in performance estimation

Since a generalized temperature dependence study for all types of T dependence is quite elaborate, a comparative study based on seven well-known and representative TE materials [20-24] was conducted. To understand the role of the T dependence of each of α , ρ and κ in performance estimation, the calculated maximum efficiencies when all properties are considered as T dependent (referred to as 'real case' or 'exact' from now on) were compared with the calculated efficiencies of model materials. These model materials have the same T dependence as the real materials for one or two of the three thermoelectric transport properties, while the remaining properties are kept constant; these materials are denoted as 2TD (two temperature dependent properties) materials and 1TD materials, respectively. The constants used to define the model materials were obtained using the spatial averages (SpAv; for electrical and thermal resistivity) at a current density corresponding to the maximum efficiency of the real material and the temperature average (TAvg; for the Seebeck coefficient). The SpAv and TAvg of a T -dependent quantity p for a hot-side temperature T_h and a cold side temperature T_c are given by [1, 12, 18, 25]

$$p_{\text{TAvg}} = \bar{p} = \frac{1}{\Delta T} \int_{T_c}^{T_h} p(T) dT, \quad (52)$$

$$p_{\text{SpAv}} = \langle p \rangle = \frac{1}{L} \int_0^L p(T(x)) dx, \quad (53)$$

where $\Delta T = T_h - T_c$ and L is the length of the TE leg. The exact efficiency using T dependent properties was obtained using the 1D solution algorithm developed in [18] by calculating

$$P = V \cdot I, \quad (54)$$

$$\text{where } V = V_o - R_{\text{in}} I, \quad V_o = \alpha \Delta T \text{ and}$$

$$\eta = P / Q_{\text{in}}. \quad (55)$$

Here, P is the output power, V is the net output voltage which is given by the Seebeck voltage generated, $V_o = \int_{T_c}^{T_h} \alpha(T) dT$, minus the voltage drop due to internal resistance $R_i = \frac{\rho_{\text{SpAv}} L}{A}$, where A is the area of the TE leg and $\rho_{\text{SpAv}} = \frac{1}{L} \int_0^L \rho(T(x)) dx$. $I = jA$ is the current passing through the TE material due to the generated voltage. The efficiency (η) is given by the ratio of output power to the input heat flow (Q_{in}) as in eq. (55) where Q_{in} is given by

$$Q_{\text{in}} = -\kappa_h \cdot A \cdot \frac{dT}{dx_h} + I \cdot \alpha_h \cdot T_h. \quad (56)$$

Q_{in} consists of the Fourier heat flow $-\kappa_{\text{h}} \cdot A \cdot \frac{dT}{dx_{\text{h}}}$ (including the fraction of Joule and Thomson heat contributions released in the leg which is flowing to the hot side) plus the Peltier heat absorbed at the hot side. The suffix h indicates the hot-side values, i.e. $\kappa_{\text{h}} = \kappa(T_{\text{h}})$ and $\alpha_{\text{h}} = \alpha(T_{\text{h}})$. As the spatial averages depend on $T(x)$ which in turn varies with current, they are formed pre-assuming the optimum current of the real materials, and for brevity, their efficiency was also calculated at the optimum current of the real material. The optimum current in the numerical calculation was obtained by finding the current where $\frac{d\eta}{dI}$ becomes zero.

The relative deviation (RD) of the calculated maximum efficiency between the 2TD model materials and the real materials, $\delta\eta_{\text{max}}^{\text{model}} = \frac{\eta_{\text{max}} - \eta_{\text{max}}^{\text{model}}}{\eta_{\text{max}}}$, is shown in Figure 4-1a. Here and in the following, for brevity we will use δ and d to denote a relative and absolute deviation, respectively. The comparison shows how strongly each of the contributing T dependences alone would shift efficiency. Obviously, the T dependence of ρ will affect the calculated efficiency to a lower extent than $\alpha(T)$ and $\kappa(T)$ will do for some materials (middle section of Fig. 1a); the asymmetry of Joule heat generation mostly plays a minor role. However, this does not hold for all materials and it does not mean that the RD between CPM and a real material due to asymmetric distribution of Joule heat, $\delta\eta_{\text{max}j} = \frac{d\eta_{\text{max}}}{d\dot{Q}_j^{\text{h}}} \delta\dot{Q}_j^{\text{h}}$, would be insignificant, as all of the three identified effects will act simultaneously when comparing CPM and the real case. Although the effects of the T dependence of $\alpha(T)$ and $\kappa(T)$ are much larger for some materials, they often partly cancel each other. A comparison of the real Joule heat partial T profiles in Figure 4-1b shows a considerable asymmetry, in correlation to the deviations in the $\rho(T) = \text{const.}$ case for SnSe and PbTe (Figure 4-1a, mid); however the RD contribution related to the profiles in Figure 4-1b is larger as they contain an asymmetry due to the asymmetry of axial heat conduction linked to $\kappa(T)$, in addition to the asymmetry of Joule heat generation which alone is represented by Figure 4-1a. Calculation of the partial T profiles is explained in the Appendix (Sect. 2). It should be noted that unlike for $\alpha(T)$ where the absence of the T dependence means an absence of Thomson heat, the absence of the T dependence of ρ just means that there is no local asymmetry in Joule heat generation whereas the amount of appearing Joule heat remains unchanged. Both symmetrically or asymmetrically released Joule heat will contribute, together with Thomson heat, to the effect of a T dependence of $\kappa(T)$ that consists in shifting the distribution of the inner reversible and irreversible heat towards the hot and cold sides. Accordingly, the magnitude of the effect of a T dependence of $\kappa(T)$ will scale with the total amount of inner heat.

When α or κ is kept constant, there can be large discrepancies as seen from the scatter in the left and right section of the Figure 4-1a. Switching off Thomson heat results in a change from non-constant to constant convective entropy flux linked to different partition of reversible (Peltier + Thomson-bound) heat to both sides of the leg. When setting $\kappa(T) = \text{const.}$, net Fourier heat transmitted does not change as the thermal resistance of the leg is fixed by the definition of the SpAv. Rather, the observed differences are merely due to changed lateral distribution of Thomson and Joule heat. Comparing to Figure 4-2a reveals that large RD for $\kappa(T) = \text{const.}$ correlates to strongly non-linear T profiles linked to $\kappa(T)$ (see T profiles for $j = 0$); see also Appendix, Figure A1a, where SnSe, Bi₂Te₃ and PbTe have significantly different κ_{h} and κ_{c} and Figure A2a showing that the weight of Joule and Thomson heat to Q_{in} is comparably large for these materials.

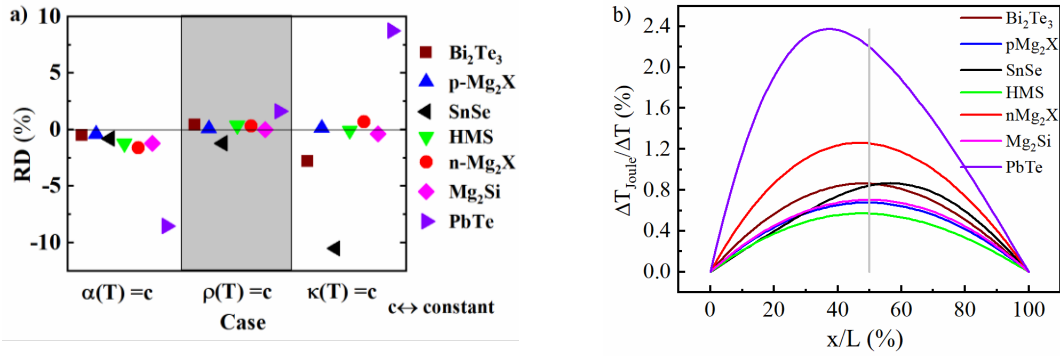


Figure 4-1: a) Comparison of the relative deviation of the calculated maximum efficiency of 2TD model materials (one of the TE properties kept constant,) from their real counterpart for the example materials, b) T profile bending caused by Joule heat for example materials. Distinct asymmetry is observed particularly for PbTe and SnSe, correlated to maximum offset values in the middle part of Fig a).

The dominating effect of the T dependence of κ and α on the estimated performance is also seen by comparing the T profiles of the model cases with the real temperature profile of n-type $\text{Mg}_2(\text{Si},\text{Sn})$ (shortly referred to as n- Mg_2X), Figure 4-2b. All profiles are calculated for the optimum current for maximum efficiency of the real material. Here, in addition to the 2TD materials, also 1TD materials were involved. $\alpha(T)$ and $\kappa(T)$ play a dominating role in the shaping of the temperature profile which is reflected by the closeness of the $\alpha(T) \neq \text{const.}$, $\kappa(T) \neq \text{const.}$ case to the real material.

The effects of the 2TD cases on the overall inflowing Fourier heat and thus on the efficiency of n- Mg_2X from Figure 4-1a (red dots) can be discussed in terms of the hot side slopes of the corresponding temperature profiles (red lines) in Figure 4-2b when comparing between cases with the same $\kappa(T)$. The downward $\frac{dT}{dx_h}$ for the 2TD material with $\alpha(T) = \text{const.}$ (red solid line) indicates an increase of the inflowing Fourier due to missing Thomson heat, compared to the actual case (dark green line). Simultaneously but only partly compensated in the Q_{in} balance by missing Thomson heat, less Peltier heat is absorbed at the hot side and therefore the efficiency is overestimated (Fig. 1a left side, red dot). The 2TD $\kappa(T) = \text{const.}$ (red dotted line) deforms the T profile considerably but does hardly increase the heat input (Eq. (56)) compared to the real material as the SpAv of $\kappa(T)$ maintains an unchanged thermal resistance of the TE leg. We can conclude that replacing the T dependence of $\alpha(T)$ and $\kappa(T)$ by adequate constants will, although significantly changing the T profile, influence the inflowing heat and thus efficiency to a much lower extent due to compensating effects. The RD of CPM efficiency in effect arises mainly from a redistribution of internal Joule and Thomson heat due to considerable deformation of the T profile by neglecting the T dependence of $\kappa(T)$ and $\alpha(T)$ and local redistribution of reversible heat generation as a consequence of neglect of the T dependence of the convective entropy flux.

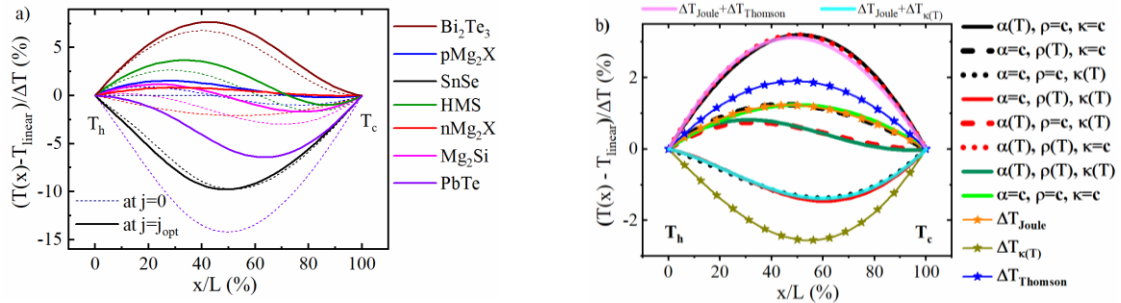


Figure 4-2: a) Bending of T profiles for the real materials at $j = 0$ (dotted lines) and $j = j_{\text{opt}}$ (solid lines), normalized to ΔT , b) T profile bending for the 1TD and 2TD model materials in comparison to the full T dependent case and the CPM case, along with the individual contributions to the fully T dependent profile for a n- $\text{Mg}_2(\text{Si},\text{Sn})$ TE leg with $T_h = 723$ K and $T_c = 383$ K.

For the comparison to 1TD and 2TD model materials additionally a shift of the SpAv values of ρ and κ as a consequence of different T profiles as well as coupling effects among the individual contributions play a role, but only to a very minor extent as proven by the close coincidence of their profiles to combinations of the individual partial T profiles of the real material, see Fig. 2b (pink and cyan lines). The latter represent the physical contributions to the real temperature profile, ΔT_{Joule} , $\Delta T_{\text{Thomson}}$ and $\Delta T_{\kappa(T)}$ and are plotted by symbols + lines in Fig. 2b. They sum up, together with the linear part, $T_{\text{lin}}(x) = T_{\text{h}} - x \frac{\Delta T}{L}$, to the total temperature profile,

$$T(x) = T_{\text{lin}}(x) + \Delta T_{\text{Joule}}(x) + \Delta T_{\text{Thomson}}(x) + \Delta T_{\kappa(T)}(x). \quad (57)$$

The procedure to calculate the partial profiles is described in Appendix 2.

From the close coincidence of combinations of the real partial T profiles to the T profiles of the 1TD and 2TD model materials as evident from Fig. 2b we can conclude that the contributions from each of the effects (Thomson heat, Joule heat, T dependence of κ) to the total $T(x)$ behave in good approximation independent and additive (A small note on this is given in the Appendix 0). The reason for the overall weak cross-coupling between the contributing effects is the small amplitude of the partial T profiles ΔT_{Joule} , $\Delta T_{\text{Thomson}}$, $\Delta T_{\kappa(T)}$ compared to the overall ΔT but also the fact that $\Delta T_{\text{Thomson}}$ and $\Delta T_{\kappa(T)}$ often partially compensate. Therefore, also the T profiles of a real material and CPM may be quite close to each other for some materials. It is evident that the shape of $\alpha(T)$ and $\kappa(T)$ affects the temperature profile much more than that of $\rho(T)$ but this does not mean that the asymmetry of Joule heat distribution between the hot and cold side would contribute insignificantly to the difference of the inflowing heat between the CPM case and a real material. Redistribution of Joule heat affects the maximum efficiency to a relevant extent along with the redistribution of Thomson heat. Thus we can split the RD of the maximum efficiency according to the physical origin – redistribution of Peltier-Thomson heat and Joule heat – as $\delta\eta_{\text{max}} = \frac{\eta_{\text{max}} - \eta_{\text{max}}^{\text{CPM}}}{\eta_{\text{max}}^{\text{CPM}}} = \delta\eta_{\text{max}\pi\tau} + \delta\eta_{\text{max}j}$.

Depending on the slope ratio of $\kappa(T)$ and $\alpha(T)$ the efficiency discrepancy due to Joule heat asymmetry, $\delta\eta_{\text{max}j}$, will vary considerably between different materials and may change sign from case to case, as observed in [18].

Now, let us proceed to understand in more detail how the absence of Thomson heat in CPM will affect the efficiency calculation. We will see that it is partially and usually not entirely compensated by the difference in Peltier heat between a real material and its CPM approximate.

4.2.2 Peltier-Thomson heat balance and the resulting uncertainty in CPM efficiency

Consider a TE material with constant κ and a linearly increasing $\alpha(T)$ curve (which is typical for a TE material below the peak zT temperature), as schematically shown in Figure 4-3. In a TE material under current flow, the convective entropy flux is given by $\dot{s}(T) = j\alpha(T)$. Hence, in a TE leg with a current flow I , the convective entropy flow $\dot{S}(T) = I\alpha(T)$ is directly linked to the temperature dependence of the Seebeck coefficient.

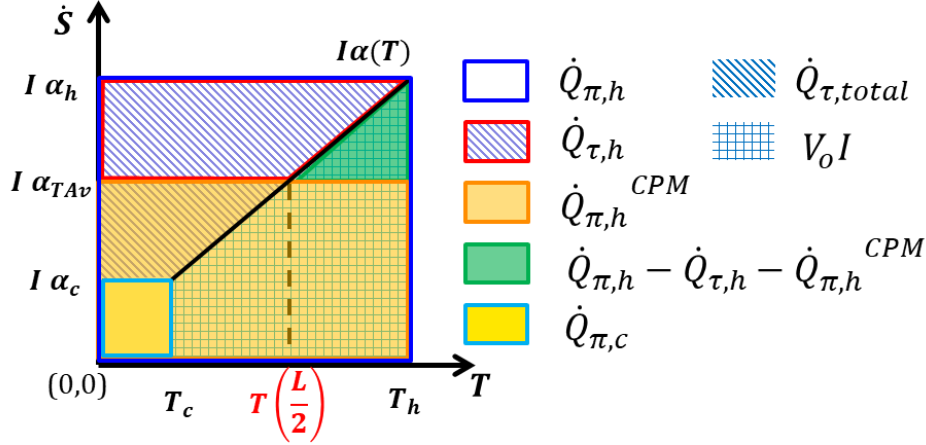


Figure 4-3: Schematic representation of reversible heat exchange in a TE leg for a linear $\alpha(T)$ curve (black line) in a plot of the convective 1D entropy flow with a constant current I . According to the relation $\dot{Q}_\pi = I\alpha T$ areas in the $\dot{S}(T)$ diagram represent certain amounts of (flowing or exchanged) Peltier (including Thomson) heat. The dark blue and light blue rectangles – in- and outflowing Peltier heat; trapezium above the $\dot{S}(T)$ curve – Thomson heat (marked with slant lines); trapezium below the $\dot{S}(T)$ curve (marked in checked lines) – gross electrical power generated ($V_0 I$); red trapezium – Thomson heat flowing to the hot side; orange rectangle – hot side Peltier heat (CPM). The green triangle indicates part of the difference amount of absorbed Peltier heat at the hot-side between the actual and the CPM cases) that is not compensated in the real material by backflowing Thomson heat $\dot{Q}_{\tau,h}$.

Peltier heat absorbed at the hot side (T_h) in the real case is given by $\dot{Q}_{\pi,h} = I\alpha_h T_h$, while at the cold side, it is $\dot{Q}_{\pi,c} = I\alpha_c T_c$. Areas in the diagram of Fig. 3 represent certain amounts of Peltier and Thomson heat but also generated electric power. This allows a schematic comparison of reversible heat exchange in a T -dependent material to its CPM approximate. The difference in the Peltier heat balance, $I(\alpha_h T_h - \alpha_c T_c)$, is given by the difference of the light and dark blue line marked areas. It is composed of the area below the $\dot{S}(T)$ curve (marked in checked lines) given by $P_0 = IV_0 = I \int_{T_c}^{T_h} \alpha(T) dT$, which is the gross produced electrical power (that includes Joule heat). The area to the left from the $\dot{S}(T)$ curve (indicated by slant lines) which is

$$\int_{I\alpha_c}^{I\alpha_h} T d\dot{S} = I \int_{T_c}^{T_h} T \frac{d\alpha}{dT} dT = I \int_{T_c}^{T_h} \tau dT = \dot{Q}_\tau \quad (58)$$

where $\tau = T \frac{d\alpha}{dT}$ is the Thomson coefficient. This area represents the net Thomson heat generated in the TE leg, \dot{Q}_τ , which is directly linked to the variation of the convective entropy flow over the leg. The reversible heat balance

$$\dot{Q}_{\pi,h} - \dot{Q}_{\pi,c} = \dot{Q}_\tau + P_0, \quad (59)$$

tells that the loss of Peltier heat in the sample equals released Thomson heat plus produced gross electrical power. \dot{Q}_τ and P_0 are counted here as positive when going out of the system. Part of the Thomson heat will flow back, as a contribution to the overall Fourier heat flow, to the hot side. For simplification we assume that Thomson heat that is released at any point in the leg will flow out to the closer side. This is physically not strict but sufficient to qualitatively illustrate the relevant effect of under-compensation of the difference in Peltier heat exchanged at the hot side in a real material compared to CPM by Thomson heat flowing back to the hot side, i.e, compensation of $d\dot{Q}_{\pi,h} = \dot{Q}_{\pi,h} - \dot{Q}_{\pi,c}^{CPM} = IT_h(\alpha_h - \bar{\alpha})$ by $\dot{Q}_{\tau,h} = I \int_{\alpha_{\tau,ex}}^{\alpha_h} T d\alpha$. The relevant question on the Seebeck value $\alpha_{\tau,ex}$ from which on the integration gives the correct amount of $\dot{Q}_{\tau,h}$ (and its corresponding temperature $T_{\tau,ex}$ with $\alpha_{\tau,ex} = \alpha(T_{\tau,ex})$) will be touched below.

In CPM, the Peltier heat at the hot side is given by $I\bar{\alpha}T_h$, while at the cold side it is $I\bar{\alpha}T_c$, where $\bar{\alpha} = \alpha_{TA_v}$ is the temperature average of $\alpha(T)$ (see Eq.(52)). Therefore, the following equation holds,

$$\dot{Q}_{\pi,h}^{\text{CPM}} - \dot{Q}_{\pi,c}^{\text{CPM}} = I\bar{\alpha}(T_h - T_c) = I \int_{T_c}^{T_h} \alpha(T) dT, \quad (60)$$

i.e. Peltier heat is completely balanced by electrical production.

From Eq. (59) and (60), it is obvious that globally the explicit absence of Thomson heat in CPM is taken care of correctly by the use of temperature averaged $\bar{\alpha}$ in the CPM, i.e.,

$$\dot{Q}_{\pi,h} - \dot{Q}_{\pi,c} - \dot{Q}_\tau = \dot{Q}_{\pi,h}^{\text{CPM}} - \dot{Q}_{\pi,c}^{\text{CPM}} = I\bar{\alpha}\Delta T = P_0. \quad (61)$$

With this choice of $\bar{\alpha}$ as the CPM value, the gross power generated is exactly the same in CPM as in the real material, at the same current. On the other hand, it implies that, typically, considerably less Peltier heat is absorbed at the hot side in the CPM case than actually, whereas back-flowing Thomson heat partly compensates the actually higher Peltier heat intake. Fig. 3 visualizes by the green triangle that this compensation is incomplete, i.e. $d\dot{Q}_{\pi\tau,h} = d\dot{Q}_{\pi,h} - \dot{Q}_{\tau,h} > 0$. Accordingly more Thomson heat is leaving at the cold side. It is evident, that this holds not only for a linear but also for a left- or right-hand bowed Seebeck curve.

In a less typical case with strongly asymmetric heat conduction, i.e. $\kappa(T)$ strongly increasing with T , or if $\alpha(T)$ forms a significant maximum, this typical tendency could reverse, but mostly it leads to underestimation of the inflowing heat in the CPM case $Q_{\text{in}}^{\text{CPM}}$ and hence to overestimation of the efficiency by CPM. With p-Mg₂X, a particular example is given in the Appendix (Figure A2c) where, with $\alpha(T)$ weakly changing between T_c and T_h but peaking inside, this compensation can also be almost perfect, or, as for SnSe (Figure 4-5b and Figure 4-6), even overcompensation may occur.

Overall, the efficiency deviation between the real and CPM cases would be negligible if $Q_{\text{in}} = Q_{\text{in}}^{\text{CPM}}$. For a rising $\alpha(T)$ curve, which is the typical case applying for most of the established TE materials, the Peltier-Thomson part, $\dot{Q}_{\pi\tau}^{\text{CPM}}$, of \dot{Q}_{in} will remain lower than the real $\dot{Q}_{\pi\tau}^h$. Thus the efficiency is often overestimated by CPM. Furthermore, a shift in $I_{\eta,\text{opt}}^{\text{CPM}}$ against the true $I_{\eta,\text{opt}}$ has to be taken into consideration due to a change in the current-dependent contributions to \dot{Q}_{in} . The usually higher intake of reversible heat at the hot side in the real case, $\dot{Q}_{\pi\tau}^h$, compared to CPM ($\delta\dot{Q}_{\pi\tau,h} > 0$) results in a steeper curve $\dot{Q}_{\text{in}}(I)$ than $\dot{Q}_{\text{in}}^{\text{CPM}}(I)$. Efficiency as defined by $\eta(I) = P/\dot{Q}_{\text{in}}$ will accordingly have a lower slope in reality than for CPM, equivalent to a lower maximum position $I_{\text{opt},\eta}$. Thus, usually, CPM will overestimate the optimum current, $\delta I_{\text{opt},\eta} = \frac{I_{\text{opt},\eta} - I_{\text{opt},\eta}^{\text{CPM}}}{I_{\text{opt},\eta}^{\text{CPM}}} < 0$, and hence will overestimate output power at maximum efficiency ($\delta P_{\eta,\text{max}} < 0$) which adds to the overestimate of maximum efficiency: $\delta\eta_{\text{max}} = \delta P_{\eta,\text{max}} - \delta\dot{Q}_{\text{in}}$, amplifying the effect of $\delta\dot{Q}_{\text{in}}$ (see Figure 4-4a). Hence, for a quantitative analysis, we have to consider three contributions to the (absolute) deviation of \dot{Q}_{in}

$$d\dot{Q}_{\text{in}} = d\dot{Q}_{\pi\tau}^h - d\dot{Q}_J^h = d\dot{Q}_{\pi\tau}^{h,I=\text{const}} - d\dot{Q}_J^{h,I=\text{const}} + \left. \frac{\partial \dot{Q}_{\text{in}}}{\partial I} \right|_{I_{\text{opt},\eta}} dI_{\text{opt},\eta}, \quad (62)$$

where, similar to the outflowing Thomson heat, also outflowing Joule heat is counted as positive and $d\dot{Q}_J^h$ is due to the Joule heat asymmetry at the hot side. Asymmetry of Joule heat distribution and heat conduction will, with falling $\kappa(T)$ as for PbTe and SnSe, favor heat release to the cold side. This will contribute to a higher \dot{Q}_{in} and steeper $\dot{Q}_{\text{in}}(I)$ likewise, amplifying the same trend as from reversible heat, or will counteract it with rising $\kappa(T)$. Thus, asymmetry of Joule heat distribution will add to the mispoint in $I_{\text{opt},\eta}^{\text{CPM}}$.

Figure 4-4a shows that for most materials, $I_{\text{opt},\eta}$ changes about 1% or less and consequently also the deviation of the output power remains small. However, for PbTe, $\delta I_{\text{opt},\eta}$ reaches 10%. Then the deviation of output power, $\delta P_{\eta,\text{max}}$, may grow in absolute amount as large as $\delta\dot{Q}_{\text{in}}$, doubling its effect. Whereas the contribution to $\delta\dot{Q}_{\text{in}}$, due to $\delta I_{\text{opt},\eta}$ usually remains insignificant, it becomes relevant for PbTe where it compensates half of $d\dot{Q}_{\text{in}}$ related to the distribution of inner heat at unchanged current, $d\dot{Q}_{\pi\tau}^h(I_{\text{opt},\eta}) - d\dot{Q}_J^h(I_{\text{opt},\eta})$, see Eq. (12), black stars in Figure 4-4a.

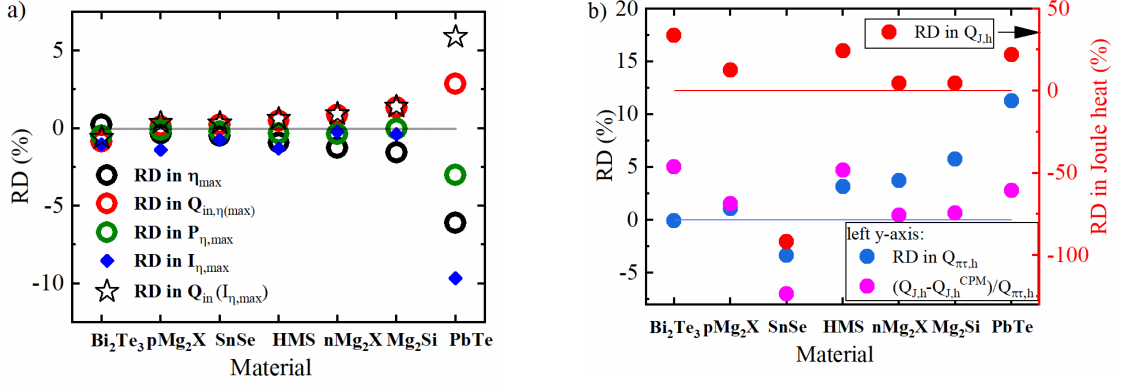


Figure 4-4: Calculated relative deviation (RD) of a) the maximum efficiency, $\delta\eta_{\max}$, heat input, δQ_{in} , power at maximum efficiency, $\delta P_{\eta,\max}$, and optimum current, $\delta I_{\text{opt},\eta}$; additionally, δQ_{in} when neglecting $\delta I_{\text{opt},\eta}$ (black stars), b) Joule heat, $\delta Q_{\pi\tau}^h$, reversible heat, δQ_J^h (see Eq. (12)) and, for direct comparison, also $dQ_J^h/Q_{\pi\tau}^h$

The RD of hot side Joule heat, δQ_J^h , and Peltier/Thomson heat, $\delta Q_{\pi\tau}^h$ with $Q_{\pi\tau}^h = Q_{\pi}^h - Q_{\tau}^h$, are shown in Fig. 4-4b. δQ_J^h reaches quite significant nominal values, mainly due to the low magnitude of Q_J^h itself. For direct comparison to $\delta Q_{\pi\tau}^h$, the (absolute) deviation dQ_J^h related to $Q_{\pi\tau}^h$ is plotted and shows that both effects reach the same order of magnitude. Typically, both contributions partly compensate. Furthermore, no general behavior can be observed in their mutual relation over the materials, in some cases clearly one effect dominates, in others the other.

As seen from Fig. 4-1b, usually, more Joule heat is released to the hot side than to the cold side in a real material whereas there are symmetric amounts in the CPM case. This contributes to an underestimation of the efficiency in the CPM case, $\delta\eta_{\max,j} > 0$. On the other hand, as explained, the Peltier-Thomson balance tends to an overestimation, $\delta\eta_{\max,\pi\tau} < 0$, thus both effects counteract and partially compensate. From Figure 4-4a can be seen that CPM overestimates the efficiency compared to the real case for all selected materials except Bi₂Te₃, which has an exceptionally higher κ_h compared to the cold-side (Figure A1a in the Appendix) together with high Joule release (Figure 4-4b) and almost compensation of the Peltier-Thomson balance. Thus the Joule contribution dominates, leading to a resulting underestimation of the efficiency. Also, SnSe behaves partly different from the general trend with a falling $\alpha(T)$ curve (Appendix Figure A1b) and the resistivity overweight at the cold side (Appendix Figure A1c). Moreover, κ_h is much lower than κ_c . As an effect, Joule heat is preferentially lead to the cold side; consequently hot side Joule heat is greatly overestimated in CPM (Fig. 4-4b), but as the relative contribution of Joule heat to Q_{in} is small (Figure A2a), the resulting trend towards overestimation of performance in CPM remains moderate. On the other hand, as seen from Appendix Figure A1b Thomson heat is absorbed in the leg as $\alpha(T)$ for SnSe is a falling curve and is mainly bound to the hot side. As seen from Fig. 4b, for SnSe, the hot side Peltier-Thomson heat will, unlike for most of the other materials, be overestimated by the CPM. However, the resulting underestimation of efficiency in CPM will be overcompensated by the counteracting Joule heat distribution.

The first four materials in our list (see Figure 4-4a) show a minor discrepancy of the CPM to reality. Although Joule heat asymmetry is contributing comparably, from case to case, mostly the dominating source of discrepancy is the uncompensated Peltier heat according to Eq.(61). It is particularly relevant in the cases of n-Mg₂X, Mg₂Si and PbTe, which have larger Thomson contributions (Figure A2a) leading to larger discrepancies of the CPM efficiency estimate.

4.2.3 Refining the CPM efficiency estimate

Having identified the effects causing a systematic uncertainty in the CPM efficiency estimation, they shall be accordingly corrected.

We want to analyze how this can be done practically for the Thomson contribution, $\delta\dot{Q}_{\pi\tau}^h$, by calculating the uncompensated Peltier heat at the hot side. Therefore we discuss the approach for example materials with dissimilar $\alpha(T)$ characteristics.

The values of $\dot{Q}_{\pi,h}$ and $\dot{Q}_{\pi,h}^{\text{CPM}}$ are known from T_h , α_h and $\bar{\alpha}$, for a given current, where as a first approximation $I_{\text{opt},\eta}^{\text{CPM}}$ is used. We have seen that the Thomson heat flowing to the hot side is strictly calculated from the partial T profile $\Delta T_{\text{Thomson}}(x)$ by $\dot{Q}_{\tau,h} = -\kappa_h \cdot \frac{d\Delta T_{\text{Thomson}}}{dx}_h$. We apply this route to form a reference for an approximate estimation to be developed because of which we shall omit a numerical calculation of exact T profiles. As derived from Eq. (10) we obtain the uncompensated Peltier-Thomson heat from $d\dot{Q}_{\pi\tau}^h = \dot{Q}_{\pi,h} + \dot{Q}_{\tau,h} - \dot{Q}_{\pi,h}^{\text{CPM}}$. Neglecting any deviation of current, this can be illustrated in the $\alpha(T)$ diagram based on our interpretation of areas by amounts of reversible heat, see Fig. 3. Thus we aim for a good approximate of the green marked area in Fig. 3 by a good and simple approximate. The problem splits into two aspects: finding the temperature $T_{\tau,\text{ex}}$ above which the inner Thomson heat is conducted to the hot side and finding a close approximate of the integral. As $\alpha(T)$ may be quite different (see Fig. A1b), we meet various situations, represented by different $\Delta T_{\text{Thomson}}(x)$ temperature profiles (Fig. A2b), among them typical ones with a single maximum according to Thomson heat flowing out to both sides, but also less typical ones with a single minimum (Thomson heat flowing in from both sides) or even two extrema (for Bi_2Te_3) where Thomson heat is released to the cold side but absorbed from the hot side. A rule to treat all of the cases likewise is needed. Fig. 5 a) and b) and Fig. A2 c) and d) show accordingly scenarios where $\alpha(T)$ contains almost linear intervals aside with strongly bowed ones / where $\alpha(T)$ is monotonous or contains a maximum / where α_h and $\bar{\alpha}$ are far from each other or close together / where $\alpha(T)$ is crossing the $\bar{\alpha}$ horizontal once or twice. The position of the extrema (maxima or minima) of $\Delta T_{\text{Thomson}}(x)$ was marked in each diagram by a brown line. Accordingly, the area corresponding to the uncompensated heat might be more complex than shown in Fig. 3, e.g. see Figure 4-5a. The area to the left from the $\alpha(T)$ curve to the α -axis from this point up to the hot side α_h (marked by a red border) represents $\dot{Q}_{\tau,h}$. Take into account that the respective area contains also negatively counting parts when $\alpha(T)$ goes through a maximum. Accordingly, the upper slim boat-shaped area in Fig. 5a counts negative; symbolically, it was mirrored into the green area.

However, in such a case the integration can be simplified switching from the hot to the cold side, as $\dot{Q}_{\tau,h} = \dot{Q}_{\tau} - \dot{Q}_{\tau,c}$ and with Eq. (10), $\dot{Q}_{\tau} = \dot{Q}_{\pi,h} - \dot{Q}_{\pi,c} - P_0$. Note that if there are two extrema of $\Delta T_{\text{Thomson}}(x)$, then we have two $T_{\tau,\text{ex}}$ values where the Thomson heat between both can be neglected as it cancels completely. Only the intervals outside, $(T_c; T_{\tau,\text{ex}})$ or $(T_{\tau,\text{ex}}; T_h)$ has to be considered. Among both intervals, the side has to be chosen where $\alpha(T)$ is a monotonous function in the relevant temperature interval, where it is closer to linearity, and possibly where $T_{\tau,\text{ex}}$ is closer to T_h or T_c .

Applying Eq.(11) accordingly to the chosen interval, the integration for \dot{Q}_{τ} can be substituted by one for P_0 , e.g. for the cold side: $\dot{Q}_{\tau,c} = \dot{Q}_{\pi,T_{\tau,\text{ex}}} - \dot{Q}_{\pi,c} - \int_{T_c}^{T_{\tau,\text{ex}}} \alpha dT$.

This is facilitating practical execution as mostly $\alpha(T)$ is known as a low-order polynomial, thus integration could be done analytically.

If the Thomson T profile is not known, half of the leg length, $\frac{L}{2}$ can be taken as a first guess of the position for the calculation of $\dot{Q}_{\tau,h}$. The according temperature is marked in the diagrams. This can be a quite good estimate when the Thomson T profile is close to symmetric as for PbTe (see Figure A2b) but may fail greatly when Thomson heat is strongly asymmetric as for SnSe. On the contrary, an entropy consideration of Thomson heat in the TE leg (see Appendix A3) leads to a thumb rule for $T_{\tau,\text{ex}}$ that is $\alpha(T_{\tau,\text{ex}}) \approx \bar{\alpha}$.

Indeed, it applies well for all example materials involved here. With this rule, approximation of $\dot{Q}_{\tau,h}$ facilitates considerably, as just a crossing point of $\alpha(T)$ with its TAV has to be found.

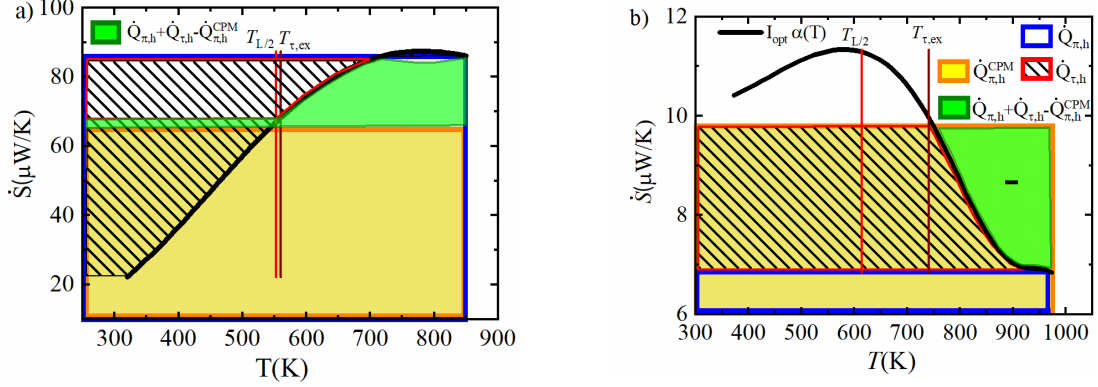


Figure 4-5: Plot of the convective 1D entropy flow at constant current I for a) PbTe and b) SnSe. Relevant areas are marked to determine the uncompensated Peltier-Thomson heat $d\dot{Q}_{\pi\tau}^h$ (green area). Note that the $\frac{L}{2}$ temperature and the temperature $T_{\tau,ex}$ according to the extremum of $\Delta T_{Thomson}(x)$ may be located quite apart (b) whereas $T_{\tau,ex}$ is very close to the crossing point of $\alpha(T)$ to $\bar{\alpha}$.

Figure 4-6 shows the remaining efficiency deviation, $\delta\eta_{max}^{corr}$, corrected by the uncompensated Peltier-Thomson heat calculated from the $\alpha(T)$ graph using the $\frac{L}{2}$ position, using $T_{\tau,ex}$ according to the extremum (maximum) position of $\Delta T_{Thomson}(x)$ but neglecting the current deviation $\delta I_{opt,\eta}$, as well as corrected by the exact deviation $d\dot{Q}_{\pi\tau}^h = \dot{Q}_{\pi,h} - \dot{Q}_{\tau,h} - \dot{Q}_{\pi,h}^{CPM}$. The efficiency estimate by CPM is greatly improved when the $\Delta T_{Thomson}(x)$ extremum position is used.

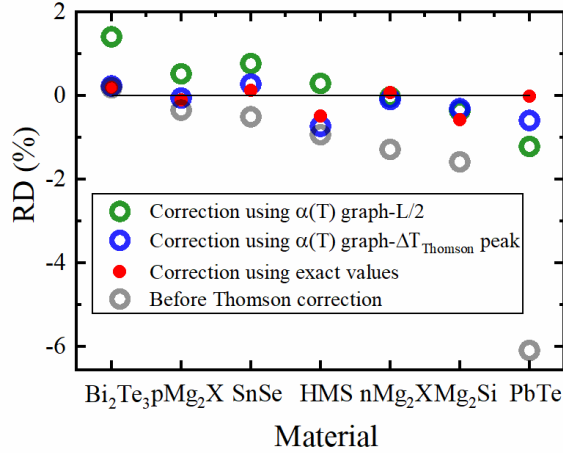


Figure 4-6: RD in maximum efficiency, $\delta\eta_{max}^{corr}$, corrected with respect to $d\dot{Q}_{\pi\tau}^{h,I=const}$ ($T_{\tau,ex}$ according to the peak of the exact Thomson profile; blue), $d\dot{Q}_{\pi\tau}^h$ (exact numerical calculation; red; cmp. also Eq. 12) and a first guess by the $\frac{L}{2}$ position.

Only occasionally, e.g. when $\alpha(T)$ is close to linear, the $\frac{L}{2}$ position works well for correction but fails for most materials as it does not take into account the asymmetry of heat sources and heat conduction. Similarly, models suggesting half of the Thomson heat on either side for correcting the CPM results [14-16, 26, 27] will mostly not work sufficiently. The correction employing the $\Delta T_{Thomson}(x)$ peak position is close to the exact numerical correction for most materials as this position considers the asymmetry exactly. The difference between both cases is merely due to the change of the optimum current which is yet unconsidered by the graphical correction. The remaining discrepancy is due to Joule heat asymmetry.

Whereas we have used exact numerical calculations to demonstrate the principle of the Thomson correction method and to show that the rule $\alpha(T_{\tau,\text{ex}}) \approx \bar{\alpha}$ holds well, the suggested practical procedure for correction of $d\dot{Q}_{\tau\tau}^{h,l=\text{const}}$ described here which is based on an analysis of the physical effects behind the deviation of CPM performance estimates is limited to basic algebraic operations which can be instantaneously be calculated by any table calculation software.

4.3 Conclusion

From the study on 2TD and 1TD model materials with one or two selected properties among α , ρ and κ set as constant, which results in both redistribution of heat between the hot and cold side of the element and the change of spatial averages, we see that in some examples large deviations in efficiency $\delta\eta_{\text{max}}^{\text{model}}$ arise as a consequence of considerable modification of the T profile. In comparison to the efficiency deviation between CPM and real materials $\delta\eta_{\text{max}}$ which conserve the spatial property averages and are mostly below 2%, this shows that a change of spatial averages due to an arbitrary modification of the T profile may contribute a strong shift to the efficiency estimate. Thus, conservation of the leg's thermal and electrical resistance is essential for a valid efficiency estimate. However, the shift remains mainly low if solely $\rho(T)$ is switched to constant. Nevertheless, it cannot be concluded from this that the temperature dependence of the electrical resistivity plays a minor role in the efficiency estimation by CPM. The 2TD and 1TD model materials lead to quite good approximates of the partial T profiles $\Delta T_{\text{Joule}}(x)$, $\Delta T_{\text{Thomson}}(x)$ and $\Delta T_{\kappa(T)}(x)$.

It is shown that the deviation of a CPM-based efficiency estimate, $\delta\eta_{\text{max}}$, is not just due to the absence of Thomson heat in CPM, as the choice of the temperature average of $\alpha(T)$ as a CPM parameter mainly compensates for the absence of Thomson heat. Rather, the discrepancy in efficiency determination in CPM is shown to be, to a major extent, due to the excess unaccounted heat at the hot-side in CPM $\delta\dot{Q}_{\text{in}}$ which usually leads to overestimation of performance (but may vary up to change of sign in less typical cases), and to a minor extent, due to a shift of the optimum current $\delta I_{\text{opt},\eta}$ and, consequently, of the produced electrical power at maximum efficiency, $\delta P_{\eta_{\text{max}}}$. In most cases, the change of the optimum current is merely small. In materials with rising $\alpha(T)$, less of the released Thomson heat flows back to the hot side than would compensate for the reduced hot-side Peltier heat absorption assumed by CPM. This systematic undercompensation tends towards an actually higher heat intake at the hot side compared to CPM, thus overestimating efficiency by using CPM. Asymmetry of Joule heat usually has an opposite influence but is overcompensated in most cases.

In order to correct for the Peltier-Thomson heat-related deviation $\delta\dot{Q}_{\tau\tau}^h$, a graphical illustration in terms over convective entropy flow based on the $\alpha(T)$ curve is given. It confirms that die rule for the splitting of Thomson heat to the sides $\alpha(T_{\tau,\text{ex}}) \approx \bar{\alpha}$ which results from an entropy consideration holds well. This enables a valid approximation of $\delta\dot{Q}_{\tau\tau}^h$ with a simple algebraic procedure, omitting the exact numerical calculation of the temperature profile. Although a considerable deformation of the T profile caused by the T dependence of $\kappa(T)$ is observed, it will affect the deviation between the real situation and its CPM approximation merely via a local shift of the thermal and electrical resistivity but will not explicitly contribute to the inflowing heat balance \dot{Q}_{in} .

In summary, the performance of a TE material does not only depend on its averaged material parameters but also on local asymmetry of Thomson and Joule heat, driven by the T dependence of the TE properties. Particularly Thomson heat can show highly asymmetric distribution. Thus, TE device efficiency can be varied beyond the averaged properties, represented by a figure of merit.

Author Contributions: Conceptualization, E.M. and P.P.; methodology, E.M and P.P.; software, P.P.; validation, P.P., E.M. and J.dB.; formal analysis and investigation, P.P., E.M. and J.dB.; resources, P.P.; data curation, P.P.; writing—original draft preparation, P.P.; writing—review and editing, P.P., E.M. and J.dB.; visualization, P.P and E.M.; supervision, E.M. and J.dB.; project administration and funding acquisition, E.M. and J.dB. All authors have read and agreed to the published version of the manuscript.

Funding: This research received no external funding.

Acknowledgments: We would like to gratefully acknowledge the endorsement from the DLR Executive Board Member for Space Research and Technology and the financial support from the Young Research Group Leader Program. P.P would like to acknowledge the German Academic Exchange Service, DAAD (Fellowship No. 247/2017) for financial support.

Conflicts of Interest: The authors declare no conflict of interest.

Appendix A

0. Note from section 2.1

A very good approximate of the actual T profile and hence the SpAv of ρ and κ in accordance to a real material can be calculated straight forward from the T dependent properties without using iterative solution [18] for $T(x)$. This may considerably simplify estimation of appropriate SpAvs as CPM property values. $\Delta T_{\text{Joule}}(x)$ can be obtained analytically from the CPM case, $\Delta T_{\kappa(T)}$ from a integration of the Fourier equation and $\Delta T_{\text{Thomson}}$ from and a 1TD $\alpha(T)$ model by a single integration.

1. Material data and boundary conditions

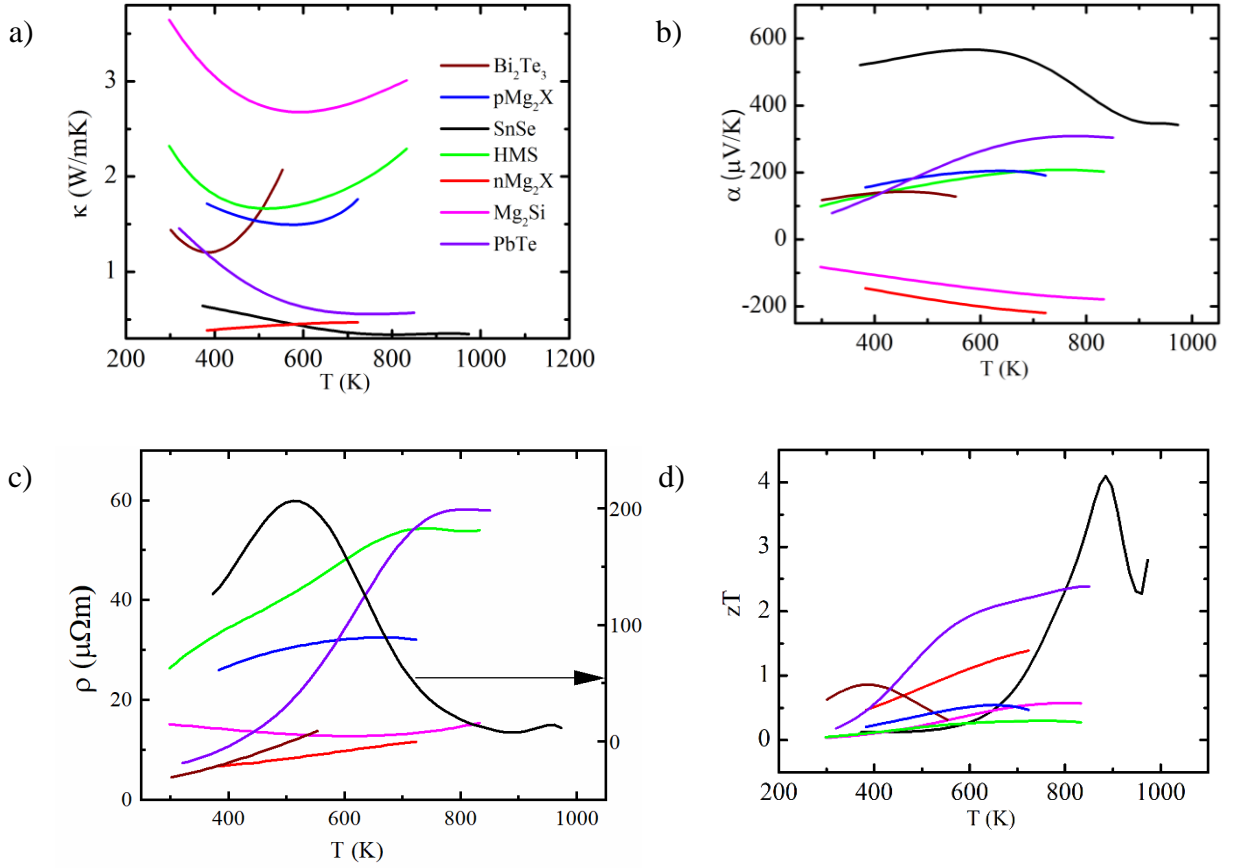


Figure A1: Temperature dependent thermoelectric material properties of representative material classes: a) thermal conductivity b) Seebeck coefficient c) electrical resistivity d) figure of merit. Since SnSe has much higher resistivity, the scale for it is given on the right y axis. All the raw experimental data taken from the literature [20-24] were fitted with appropriate polynomials (usually 3rd or 4th order). For SnSe , a 9th order polynomial fit was used owing to the complex T dependence and hence shows an unusual very high zT_{max} . However, this does not affect the physics discussed and hence this fitted data was used throughout the manuscript.

Table A1: Temperature range of analysis for all materials of Fig. A1

Material	Temperature range of analysis
----------	-------------------------------

p-Mg ₂ (Si,Sn)	723 K to 383 K
n-Mg ₂ (Si,Sn)	723 K to 383 K
HMS	833 K to 298 K
Mg ₂ Si	833 K to 298 K
p- Bi ₂ Te ₃	553 K to 301 K
SnSe	973 K to 373 K
PbTe	850 K to 320 K

1. Additional information

a. Finding individual contributions to the total T profile

The partial T profiles are found, each, by equating $\kappa(T) \frac{\partial^2 T}{\partial x^2}$ in Eq. (51) to each of the other corresponding term assuming isothermal boundary conditions and fixing all coefficients in the equation according to the total T profile $T(x)$. Thus, solving for the respective partial T profile reduces to a double integration, where the first step provides the total amount of each partial heat contributing to the thermal balance.

As the partial T profiles can have opposite sign in amplitude and partially compensate for many of the common TE materials (however, not always), the T profiles of a real material and CPM may be quite close, as in the example of n-type Mg₂X, Fig. 2b.

b. Contributions to \dot{Q}_{in}

As both Joule and Thomson heat, after appearing inside the leg will flow out, physically, as Fourier heat, we have to consider in this discussion the pure Fourier heat $Q_{F,h} = K\Delta T$ (with $K = \langle \kappa^{-1} \rangle^{-1} A/L$) which is merely related to the thermal resistance of the leg and is constant along the leg, separately from the Joule- and Thomson-related contributions. Accordingly, Q_{in} is composed of

$$\dot{Q}_{in} = \dot{Q}_{F,h} + \dot{Q}_{\pi,h} - \dot{Q}_{\tau,h} - \dot{Q}_{J,h} \quad (\text{A1.63})$$

The real Joule- and Thomson-related contributions $-\dot{Q}_{\tau,h}$ and $-\dot{Q}_{J,h}$ to the inflowing hot side heat are calculated by splitting the overall temperature profile $T(x)$ into additive partial T profiles, each related to one of the individual physical contributions. Partial Thomson T profiles of example materials are plotted in Figure A2b. Evaluating $-\kappa_h \cdot \left(\frac{d}{dx} \Delta T_{\text{Thomson}} \right)_h$ and $-\kappa_h \cdot \left(\frac{d}{dx} \Delta T_{\text{Joule}} \right)_h$ from the partial T profiles gives $\dot{Q}_{\tau,h}$ and $\dot{Q}_{J,h}$, respectively.

Figure A2a shows the relative contribution of each heat to \dot{Q}_{in} : $\frac{\dot{Q}_{F,h}}{\dot{Q}_{in}}, \frac{\dot{Q}_{\pi,h}}{\dot{Q}_{in}}, -\frac{\dot{Q}_{J,h}}{\dot{Q}_{in}}, -\frac{\dot{Q}_{\tau,h}}{\dot{Q}_{in}}$. This comparison reveals that Joule and Thomson heat contribute about 1–5% to \dot{Q}_{in} , usually flowing out, with their contributions being roughly of the same order. Figure A2a also shows the fraction of Thomson heat and Joule heat distributed to the hot side ($\frac{\dot{Q}_{\tau,h}}{\dot{Q}_{\tau}}$ and $\frac{\dot{Q}_{J,h}}{\dot{Q}_{J}}$).

In order to illustrate example situations of distribution of Peltier and Thomson heat along the leg, $\alpha(T)$ graphs for p-Mg₂X and Bi₂Te₃ are given in Figure A2c and Figure A2d respectively. Due to the bowed shape of the $\alpha(T)$ graph and relatively close α_h to α_c values for p-Mg₂X, the difference between $\dot{Q}_{\pi,h}$ and $\dot{Q}_{\pi,h}^{\text{CPM}}$ is almost negligible, but $\dot{Q}_{\tau,h}$ amounts to more than twice the amount of $\dot{Q}_{\pi,h} - \dot{Q}_{\pi,h}^{\text{CPM}}$. Nevertheless, this did not affect the efficiency deviation $\delta\eta_{\text{max}}$ too much as $\dot{Q}_{\tau,h}$ is quite small, absolutely. In the case of Bi₂Te₃, $\dot{Q}_{\pi,h}^{\text{CPM}}$ is even higher than $\dot{Q}_{\pi,h}$ again due to the curved shape of $\alpha(T)$ affecting the position of $\alpha_{T_{AV}}$. However, $\dot{Q}_{\tau,h}$ almost completely compensates this Peltier heat difference keeping the influence on the efficiency deviation negligible.

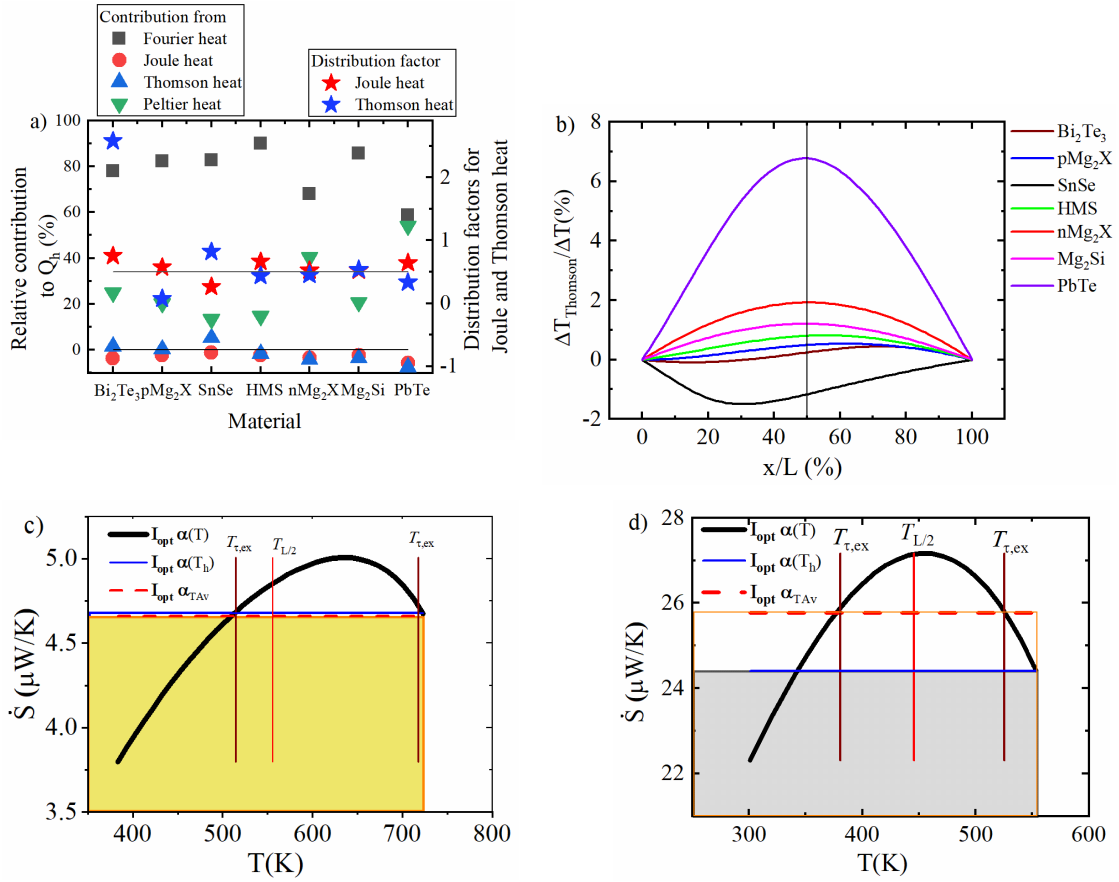


Figure A2: a) Ratio of individual heat contributions to \dot{Q}_{in} (Eq. A1.1) calculated from the corresponding partial temperature profiles) (for comparison, all quantities are accounted positive when flowing into the element) (left y -axis), and distribution factors (right y -axis) for Thomson and Joule heat. b) Thomson T profiles for all example materials c) $\dot{S}(T)$ diagram for p-Mg₂X showing the area between $I\alpha(T_h)$ and $I\alpha_{T_{\text{Av}}}$ (corresponding to the Peltier heat difference between CPM and real case) being very small due to the shape of $\alpha(T)$. The position of the first peak in the Thomson partial T profile is marked as a brown vertical line. d) $\dot{S}(T)$ diagram for Bi₂Te₃ where $\alpha_{T_{\text{Av}}} > \alpha(T_h)$. Hence $\dot{Q}_{\pi, h}^{\text{CPM}}$ is higher than $\dot{Q}_{\pi, h}$.

A3. Thomson heat distribution and entropy

With the TEG leg, we discuss the entropy flow in a reversible system of Peltier heat transport and Thomson heat exchange which is running on a non-equilibrium temperature background mainly fixed by the continuous flow of Fourier heat. As released Thomson heat will be transported as Fourier heat but is small in relation to the Fourier heat background (see Fig. A2 a) which is driven by the temperature difference and the thermal resistance of the TE leg, we will treat the variation of the temperature profile by the conducted Thomson heat as insignificant for the following consideration.

In the steady state, the entropy of the system remains constant; there is a continuous entropy production by the dissipative heat transport from hot to cold and the balancing continuous entropy export by

transmitted Fourier heat (plus negligible fraction arising from outflowing Joule heat). Assuming ideal outer current leads with $\alpha = 0$, there is no other entropy exchange at the hot and cold sides.

In the CPM, we have a constant convective entropy flow $\bar{\alpha}I$ throughout the element, equal to the absorbed and released entropy rate $\bar{\alpha}I$ by absorption and release of Peltier heat at the terminals. In a real material, the absorbed entropy rate $\alpha_h I$ equals the convective entropy flow at the hot side, and likewise, at the amount of $\alpha_c I$ at the cold side. The variation of α along the leg drives local Thomson heat production $d\dot{Q}_\tau = T \frac{d\alpha}{dT} IdT = TId\alpha$, contributing an entropy flow increment $d\dot{S} = Id\alpha$. Thomson heat is flowing to the hot and cold sides, the related total entropy exchange is $(\alpha_h - \alpha_c)I = \Delta\alpha I$. It distributes by the fraction x_h to the hot and cold sides;

$$\Delta\dot{S}_{\tau,h} = x_h(\alpha_h - \alpha_c)I \text{ and } \Delta\dot{S}_{\tau,c} = (1 - x_h)(\alpha_h - \alpha_c)I. \quad (\text{A3.1})$$

Driven by the gradient of the partial Thomson temperature profile, all Thomson heat released at one side of a maximum (or minimum) of this profile will be exchanged to this side of the leg. With the temperature $T_{\tau,\text{ex}}$ of this position and its Seebeck coefficient $\alpha_{\tau,\text{ex}} = \alpha(T_{\tau,\text{ex}})$, the shares of the entropy exchange which are bound to each of the sides are

$$\Delta\dot{S}_{\tau,h} = (\alpha_h - \alpha_{\tau,\text{ex}})I \text{ and } \Delta\dot{S}_{\tau,c} = (\alpha_{\tau,\text{ex}} - \alpha_c)I. \quad (\text{A3.2})$$

Multiplying both by the respective temperature of the side yields total Thomson heat:

$$\dot{Q}_\tau = T_h(\alpha_h - \alpha_{\tau,\text{ex}})I + T_c(\alpha_{\tau,\text{ex}} - \alpha_c)I = \{T_h\alpha_h - T_c\alpha_c - \alpha_{\tau,\text{ex}}(T_h - T_c)\}I = \Delta\dot{Q}_\pi - I\alpha_{\tau,\text{ex}}\Delta T. \quad (\text{A3.3})$$

Comparing (A3.3) with the energy balance of reversible heat $\dot{Q}_\tau = \Delta\dot{Q}_\pi - IV_0$ we can conclude that

$$\alpha_{\tau,\text{ex}}\Delta T = V_0 = \bar{\alpha}\Delta T, \text{ thus } \alpha_{\tau,\text{ex}} = \bar{\alpha}. \quad (\text{A3.4})$$

This gives us a rule on the temperature intervals over which the Thomson heat is flowing to either side of the leg. Consequently, Thomson heat has to be integrated from the crossing point of the curve of the Seebeck coefficient $\alpha(T)$ with its temperature average $\bar{\alpha}$. As a reversible approximation, this result is approximate and not strict as we have neglected here that dissipative processes are involved when Thomson heat is conducted to the leg sides. Below we will analyze these changes and find that these are small, thus the rule stated here on the position of $\alpha_{\tau,\text{ex}}$, although not strict, is a good guide for estimates of the distribution of Thomson heat. Indeed, as observed by comparison to exact numerical calculations this rule is almost perfectly fulfilled for all the example materials.

Within this reversible approximation, the Thomson heat flowing to the hot side is obtained as $\dot{Q}_{\tau,h} = T_h(\alpha_h - \bar{\alpha})I$. This would be equivalent to a complete compensation of the Peltier heat difference between reality and CPM, i.e. vanishing axial redistribution of reversible heat which is consistent to the simplifying assumption that the Thomson heat flowing to the outside is transmitted free of dissipation, i.e. equivalent to reversible heat. Here, the (additional) T gradient related to the flow of Thomson heat is neglected whereas an underlying T profile related to an independent heat flow (here the background of Fourier heat transfer) does, in effect, not contribute to its dissipation. We will see below that this happens as Thomson heat flowing to different sides will contribute almost compensating shares to the entropy balance. What was neglected here is that the Thomson heat itself when flowing to the ends of the leg will dissipate, according to the slight shift of the inner T profile it is causing. Above, this T offset was separated and called the partial T profile due to Thomson heat, $\Delta T_{\text{Thomson}}(x)$. Also this omission will contribute to a weak deviation from the position rule $\alpha_{\tau,\text{ex}} = \bar{\alpha}$.

The dissipative part of the entropy transport to the sides of the leg is related to the T drop or step-up between the location where an increment of Thomson heat $d\dot{Q}_\tau$ is released and the side temperature, T_h or T_c . The entropy increment released over a segment of the leg with the T increment dT is $d\dot{S} = I d\alpha = \frac{d\dot{Q}_\tau}{T}$. With the transfer to the, e.g. cold side, the transmitted increment of Thomson heat $d\dot{Q}_\tau$ increases its entropy up to $d\dot{S}_c = \frac{d\dot{Q}_\tau}{T_c}$, the according entropy gain is

$$d\Delta\dot{S}_c = d\dot{S}_c - d\dot{S} = \frac{d\dot{Q}_\tau}{T_c} - \frac{d\dot{Q}_\tau}{T} = \frac{d\dot{Q}_\tau}{TT_c} (T - T_c) = d\dot{S} \frac{T - T_c}{T_c}. \quad (\text{A3.5})$$

Summing over all Thomson heat flowing to that side we have

$$\Delta\dot{S}_c = \frac{1}{T_c} \int_{I\bar{\alpha}_c}^{I\bar{\alpha}} (T - T_c) d\dot{S} = \frac{I}{T_c} \int_{\alpha_c}^{\bar{\alpha}} (T - T_c) d\alpha = \frac{I}{T_c} \int_{T_c}^{T_{\bar{\alpha}}} T \frac{d\alpha}{dT} dT - I(\bar{\alpha} - \alpha_c). \quad (\text{A3.6})$$

Multiplying with the cold side temperature, $\Delta\dot{Q}_{\tau,c} = T_c \Delta\dot{S}_c = \int_{T_c}^{T_{\bar{\alpha}}} T \frac{d\alpha}{dT} dT - I(\bar{\alpha} - \alpha_c)T_c$ gives us the amount of Thomson heat that is just the difference to the Peltier-Thomson heat balance of CPM, $\Delta\dot{Q}_{\tau,c} = \dot{Q}_{\tau,c} - (\dot{Q}_{\pi,c}^{\text{CPM}} - \dot{Q}_{\pi,c})$, i.e. the part that we have identified as uncompensated Peltier-Thomson heat in a real material. Note that $\dot{Q}_{\pi,c}^{\text{CPM}}$ contains merely completely reversible exchange of Peltier heat. Thus, the incomplete compensation of the Peltier-Thomson heat balance can be understood as an effect of the partly dissipative character of the exchange of the Thomson heat in a real system when conducted to the side. Accordingly, with the same consideration for the hot side, with $d\dot{S}_h = \frac{d\dot{Q}_\tau}{T_h}$ we obtain

$$\Delta\dot{S}_h = d\dot{S}_h - d\dot{S} = \frac{d\dot{Q}_\tau}{T_h} - \frac{d\dot{Q}_\tau}{T} = \frac{I}{T_h} \int_{\bar{\alpha}}^{\alpha_h} (T - T_h) d\alpha = \frac{I}{T_h} \int_{T_{\bar{\alpha}}}^{T_h} T \frac{d\alpha}{dT} dT - I(\alpha_h - \bar{\alpha}), \quad (\text{A3.7})$$

i.e. $\Delta\dot{S}_h$ gives a negative contribution to the entropy balance. This sounds contradictory to the second law of thermodynamics but is not as the Thomson heat is not really flowing from lower to higher temperature but, when released, reduces the T gradient of the underlying background of flowing Fourier heat thus reducing the Fourier heat flow by the amount of “upstreaming” Thomson heat.

Both the hot and cold side entropy change together gives

$$\Delta\dot{S} = \Delta\dot{S}_h + \Delta\dot{S}_c = \frac{I}{T_h} \int_{\bar{\alpha}}^{\alpha_h} (T - T_h) d\alpha + \frac{I}{T_c} \int_{\alpha_c}^{\bar{\alpha}} (T - T_c) d\alpha =$$

(A3.8)

$$= \frac{I}{T_c} \int_{T_c}^{T_{\bar{\alpha}}} T \frac{d\alpha}{dT} dT + \frac{I}{T_h} \int_{T_h}^{T_{\bar{\alpha}}} T \frac{d\alpha}{dT} dT - I(\alpha_h - \alpha_c).$$

With $\frac{1}{T_c} \int_{\alpha_c}^{\bar{\alpha}} T d\alpha \gtrsim \bar{\alpha} - \alpha_c$ and $\frac{1}{T_h} \int_{\bar{\alpha}}^{\alpha_h} T d\alpha \lesssim \alpha_h - \bar{\alpha}$ we get

$$\frac{I}{T_c} \int_{T_c}^{T_{\bar{\alpha}}} T \frac{d\alpha}{dT} dT + \frac{I}{T_h} \int_{T_h}^{T_{\bar{\alpha}}} T \frac{d\alpha}{dT} dT \approx I(\alpha_h - \alpha_c) \text{ and thus } \Delta\dot{S} \approx 0. \text{ Hence, assuming } \alpha_{\tau,ex} = \bar{\alpha}, \text{ the entropy}$$

balance of the inner Thomson heat transfer as an offset of a much larger background Fourier heat flow is almost zero. This indeed confirms our approach to deduce a rule for the local distribution of Thomson heat based on a reversible approximation, i.e. assuming $\Delta\dot{S} \approx 0$ but also shows that the rule is not completely strict.

References for chapter 4 (paper 2):

1. Min, G. and D. Rowe, *Cooling performance of integrated thermoelectric microcooler*. Solid-State Electronics, 1999. **43**(5): p. 923-929.
2. Goupil, C., et al., *Thermodynamics of thermoelectric phenomena and applications*. 2011. **13**(8): p. 1481-1517.
3. Snyder, G.J. and E.S. Toberer, *Complex thermoelectric materials*, in *Materials For Sustainable Energy: A Collection of Peer-Reviewed Research and Review Articles from Nature Publishing Group*. 2011, World Scientific. p. 101-110.
4. Rowe, D.M., *Thermoelectrics handbook: macro to nano*. 2005, CRC press.
5. Antonova, E.E. and D.C. Looman. *Finite elements for thermoelectric device analysis in ANSYS*. in *Thermoelectrics, 2005. ICT 2005. 24th International Conference on*. 2005. IEEE.
6. Goupil, C., *Continuum theory and modeling of thermoelectric elements*. 2015: John Wiley & Sons.
7. Kim, C.N., *Development of a numerical method for the performance analysis of thermoelectric generators with thermal and electric contact resistance*. Applied Thermal Engineering, 2018. **130**: p. 408-417.

8. Hogan, T. and T. Shih, *Modeling and characterization of power generation modules based on bulk materials*. Thermoelectrics Handbook: Macro to Nano, 2006: p. 12.1-12.23.
9. Oliveira, K.S., R.P. Cardoso, and C.J. Hermes, *Two-Dimensional Modeling of Thermoelectric Cells*. 2014.
10. Kim, H.S., W. Liu, and Z. Ren, *The bridge between the materials and devices of thermoelectric power generators*. Energy & Environmental Science, 2017. **10**(1): p. 69-85.
11. Kim, H.S., W. Liu, and Z.J.J.o.A.P. Ren, *Efficiency and output power of thermoelectric module by taking into account corrected Joule and Thomson heat*. 2015. **118**(11): p. 115103.
12. Ryu, B., J. Chung, and S. Park, *Thermoelectric efficiency has three Degrees of Freedom*. arXiv preprint arXiv:1810.11148, 2018.
13. Sunderland, J.E. and N.T. Burak, *The influence of the Thomson effect on the performance of a thermoelectric power generator*. Solid-State Electronics, 1964. **7**(6): p. 465-471.
14. Min, G., D.M. Rowe, and K. Kontostavlikis, *Thermoelectric figure-of-merit under large temperature differences*. Journal of Physics D: Applied Physics, 2004. **37**(8): p. 1301.
15. Chen, J., Z. Yan, and L. Wu, *The influence of Thomson effect on the maximum power output and maximum efficiency of a thermoelectric generator*. Journal of Applied Physics, 1996. **79**(11): p. 8823-8828.
16. Fraisse, G., et al., *Comparison of different modeling approaches for thermoelectric elements*. Energy conversion and management, 2013. **65**: p. 351-356.
17. Sandoz-Rosado, E.J., S.J. Weinstein, and R.J. Stevens, *On the Thomson effect in thermoelectric power devices*. International Journal of Thermal Sciences, 2013. **66**: p. 1-7.
18. Ponnusamy, P., J. de Boor, and E. Müller, *Using the constant properties model for accurate performance estimation of thermoelectric generator elements*. Applied Energy, 2020. **262**: p. 114587.
19. Zhang, T., *Effects of temperature-dependent material properties on temperature variation in a thermoelement*. Journal of Electronic Materials, 2015. **44**(10): p. 3612-3620.
20. Wu, H., et al., *Broad temperature plateau for thermoelectric figure of merit $ZT > 2$ in phase-separated PbTe 0.7 S 0.3*. Nature communications, 2014. **5**(1): p. 1-9.
21. Sankhla, A., et al., *Mechanical Alloying of Optimized Mg₂ (Si, Sn) Solid Solutions: Understanding Phase Evolution and Tuning Synthesis Parameters for Thermoelectric Applications*. ACS Applied Energy Materials, 2018. **1**(2): p. 531-542.
22. Kamila, H., et al., *Analyzing transport properties of p-type Mg₂ Si–Mg₂ Sn solid solutions: optimization of thermoelectric performance and insight into the electronic band structure*. Journal of Materials Chemistry A, 2019.

23. Kim, H.S., et al., *Design of segmented thermoelectric generator based on cost-effective and light-weight thermoelectric alloys*. Materials Science and Engineering: B, 2014. **185**: p. 45-52.
24. Zhao, L.-D., et al., *Ultralow thermal conductivity and high thermoelectric figure of merit in SnSe crystals*. Nature, 2014. **508**(7496): p. 373.
25. Seifert, W., M. Ueltzen, and E. Müller, *One-dimensional modelling of thermoelectric cooling*. physica status solidi (a), 2002. **194**(1): p. 277-290.
26. Lamba, R. and S. Kaushik, *Thermodynamic analysis of thermoelectric generator including influence of Thomson effect and leg geometry configuration*. Journal of Energy Conversion and Management, 2017. **144**: p. 388-398.
27. Garrido, J., A. Casanovas, and J.A. Manzanares, *Thomson Power in the Model of Constant Transport Coefficients for Thermoelectric Elements*. J Journal of Electronic Materials, 2019. **48**(9): p. 5821-5826.



© 2020 by the authors. Submitted for possible open access publication under the terms and conditions of the Creative Commons Attribution (CC BY) license (<http://creativecommons.org/licenses/by/4.0/>).

5 Material optimization using exact efficiency (Publication 3)

This paper deals with the problems associated with using zT as a parameter for optimizing the carrier concentration of TE modules. zT is used typically for optimizing n at each temperature, however, a module operates within a range of temperature. Therefore, efficiency is considered as a parameter for such an optimization. SPB model is used for modelling the material properties of $Mg_2(Si,Sn)$ solid solutions and it is shown that efficiency and zT_{TAV} are suitable parameters to be used for optimization of material parameters.

DOI : [10.1088/2515-7655/ac293e](https://doi.org/10.1088/2515-7655/ac293e). This article was published on 13th October 2021 in Journal of Physics-Energy journal (IoP Publishing). Author contributions are specified in the published article as well as at the end of this thesis.

Efficiency as a performance metric for material optimization in thermoelectric generators

P. Ponnusamy¹, H. Kamila¹, E. Müller^{1,2,4} and J. de Boor^{1,3}

¹ German Aerospace Center (DLR), Institute of Materials Research, D–51170 Köln, Germany

² Justus Liebig University Gießen, Institute of Inorganic and Analytical Chemistry, D–35392 Gießen, Germany

³ Faculty of Engineering, Institute of Technology for Nanostructures (NST), University of Duisburg-Essen, Building BA, Bismarckstr. 81, 47057 Duisburg, Germany

⁴ Center for Materials Research/LaMa, Justus Liebig University, Giessen, D–35392 Giessen, Germany

Abstract

The optimization of thermoelectric (TE) materials with respect to carrier concentration, chemical composition, microstructure, etc. is inevitable for maximizing the performance of thermoelectric devices. Theoretical performance prediction can speed up this process dramatically as the synthesis and experimental characterization of all relevant combinations is practically impossible. Conventionally, the dimensionless figure of merit (zT) is considered as a measure of TE energy conversion capability. However, zT could mislead the search for optimized materials as it is only an intermediate parameter. To resolve this issue, we combined a device performance calculation routine (one-dimensional continuum theory-based, with fully temperature dependent TE properties) with a band structure-based material model. As an example, a study was conducted on p-type $\text{Mg}_2\text{Si}_{1-x}\text{Sn}_x$ solid solutions for which optimization of carrier concentration (n) and composition (x) is required. Here, according to previous findings, a single parabolic band (SPB) model was assumed, with an effective mass linearly dependent on composition and carrier concentration, and acoustic phonon and alloy scattering of the charge carriers. It was found that for a cold side temperature of 300 K and a hot side temperature of 500 K (which is well within the validity limits of a SPB model), the optimum n for $\text{Mg}_2\text{Si}_{1-x}\text{Sn}_x$ based on efficiency was found to be at $4.5 \times 10^{19} \text{ cm}^{-3}$, while based on zT_{max} it was found to be about 20% higher. Additionally, the usage of the temperature average of zT (zT_{TAV}) for finding the optimum parameters is also analyzed. For p- $\text{Mg}_2(\text{Si},\text{Sn})$ zT_{TAV} predicts the optimum composition and carrier concentration close to the exact efficiency calculation, despite the fact that the efficiency predicted by zT_{TAV} can be quite off from exact efficiency. The usage of zT_{TAV} was further tested for common TE material examples such as n-type $\text{Mg}_2\text{Si}_{1-x}\text{Sn}_x$ and PbTe and a similar conclusion is obtained. Finally, the reason for this closeness and the importance of using exact efficiency plots is discussed.

Keywords: TEG performance, Device modelling, Material modelling, Single Parabolic Band (SPB) model, Material optimisation, Carrier concentration.

5.1 Introduction

Devices made of thermoelectric (TE) materials convert a certain fraction of the heat passed through them into useful electrical power or, vice versa, can pump heat from cold to hot, driven by an electric current (1). A good thermoelectric generator material needs to be able to maintain the temperature (T) difference (i.e. should have low thermal conductivity κ) while being able to transport the generated electric power to the external load at low internal loss (high electrical conductivity σ). The Seebeck coefficient (α), which is proportional to the output voltage, is inversely related to electrical conductivity (more specifically to the number of charge carriers) (2). Due to this inherent, partially reverse coupling, an optimum between these TE properties has to be found for best performance (2). Materials have to be engineered to meet this optimum, resulting in exploration of several adjustable parameters such as base composition, ratios of the constituting elements, doping level, dopants species, etc., affecting the electronic band structure and thermal transport. For example, tuning the doping species and concentrations in Skutterudites (3), Mg_3Sb_2 (4, 5) or tuning of x in $\text{PbTe}_{1-x}\text{Se}$ (6), $\text{Bi}_{2-x}\text{Sb}_x\text{Te}_3$ (7), Sn_{1-x}Se (8), $\text{Mg}_2\text{Si}_{1-x}\text{Sn}_x$ (9) and changing the Zr or Hf concentration in half-Heuslers (10, 11) are some strategies to optimize performance.

In order to reduce time-consuming experimental efforts to study the effect of each of the free parameters, modelling material properties and thereby predicting TE device performance is a convenient approach. Conventionally, a dimensionless figure of merit (zT) defined as $\frac{\alpha^2 \sigma}{\kappa} \cdot T$ is used as a measure of performance, guiding the development of thermoelectric materials (1). However, zT as a measure of efficiency originates from the maximum efficiency expression $\eta_{\max} = \frac{\Delta T}{T_h} \frac{(-1 + \sqrt{1 + zT_m})}{\left(\frac{T_c}{T_h} + \sqrt{1 + zT_m}\right)}$ derived under the Constant Property Model (CPM) assumptions, whereas in reality, the material properties are temperature dependent. Constant averaged material properties entering the CPM model (obtained by averaging the temperature dependent data) must be chosen such that they reflect the actual material behaviour in the device as good as possible. Despite the use of appropriate averages, the efficiency prediction is inaccurate due to asymmetry in distribution of Joule heat to the hot and cold side of the device and assumption of magnitude and distribution of Peltier-Thomson heat in CPM compared to reality (12-17). Additionally, the Carnot efficiency (16, 18, 19) is not taken into account when considering just the figure of merit z . Therefore, zT alone can be quite misleading for performance estimation (16-20).

To overcome this, here, we analyse the device efficiency (for temperature dependent properties) directly to estimate the optimum parameters. This is done by a custom-made 1D performance calculation tool (based on the solution of the 1D heat balance) that was developed in (17). The material properties can be obtained from electronic band structure models such as the single parabolic band (SPB) model (21, 22), a multiband model (23-25) or similar models which give simplified expressions for material properties based on the solution of the Boltzmann transport equation (BTE). The 1D device performance routine is combined with the BTE-based models in a single calculation routine such that the fundamental material parameters are directly coupled to the predicted device efficiency.

As an example for the implementation of the technique, p-type $\text{Mg}_2\text{Si}_{1-x}\text{Sn}_x$ has been chosen as $\text{Mg}_2(\text{Si},\text{Sn})$ solid solutions have gained popularity due to the high performance of the n-type materials (26, 27), availability, low cost and progress in contact development (28, 29). However, the p-type suffers from still limited performance with a maximum reported zT of about 0.5 (9, 30) and hence, the performance needs to be improved. Previously, several authors (9, 31-34) have shown the capability of an SPB model to closely describe the behaviour of p-type $\text{Mg}_2\text{Si}_{1-x}\text{Sn}_x$. In a recent study (31), the SPB model was successfully applied to the whole compositional range of p-type $\text{Mg}_2\text{Si}_{1-x}\text{Sn}_x$, involving acoustic phonon and alloy scattering as dominant scattering mechanisms. This allowed for an approximate identification of the optimum carrier concentration n_{opt} and optimum composition x_{opt} . However, the optimum was determined based on zT_{max} which is not exact. Here, we would like to identify refined optimum parameters for p- $\text{Mg}_2\text{Si}_{1-x}\text{Sn}_x$ using the actual efficiency and compare the results with those obtained using averaged zT_{TAV} as an indicator of optimum parameters.

5.2 Method

The basic SPB model equations describing the three main TE transport properties (α , σ and κ) are given below (22)

$$|\alpha| = \frac{k_B}{e} \left(2 \frac{F_1(\eta_c)}{F_0(\eta_c)} - \eta_c \right) \quad (64)$$

$$\sigma = ne\mu \quad (65)$$

$$\kappa = \kappa_L + L \sigma T \quad (66)$$

$$n = 4\pi \left(\frac{2m_D^* k_B T}{h^2} \right)^{1.5} F_{0.5}(\eta_c) \quad (67)$$

where $F_i = \int_0^\infty \frac{e^{i\epsilon} d\epsilon}{1+e^{[\epsilon-\eta_c]}}$ is the Fermi integral of the order i , k_B is the Boltzmann constant, e is the electronic charge, $\eta_c = \frac{E_F}{k_B T}$ is the reduced chemical potential of the charge carriers and E_F is the Fermi energy. n is the charge carrier concentration given by eq. (67) where m_D^* is the density of states effective mass, h is Planck's constant, and μ is the mobility. In contrast to the original publication where the experimental data is discussed and a linear fit for m_D^* is used (31) we have introduced here a bilinear equation for m_D^* with a dependence both on n and x . The additional weak dependence on n improves the agreement between experimental data and model as discussed in (31); the best fit is given by $m_D^*(x, n) = (2.14 - 1.39x + 0.16 * 10^{-20} \text{ cm}^3 n)m_0$, where m_0 is the electron rest mass. The fitted 2D plot and the comparison of a purely linear fit of $m_D^*(x)$ and $m_D^*(x, n)$ with m_D^* obtained by comparing the SPB model with experimental data is given in the Supplementary information (SI) in Figure S1. In p-type $\text{Mg}_2\text{Si}_{1-x}\text{Sn}_x$, the mobility is assumed to be governed by acoustic phonon and alloy scattering mechanisms (31). The exact equations for these scattering mechanisms and the scattering potentials used (from (31) which were obtained by comparing the SPB model with experimental data) are given in the SI.

For predicting the properties using the SPB model, for each n (taken as a free parameter), the chemical potential is calculated from the Fermi integral and with this, $\alpha(T)$ is calculated. The electrical conductivity $\sigma(T)$ is calculated according to eq. (65). The thermal conductivity κ consists of the lattice thermal conductivity κ_L and the conductivity associated with the charge transport given by $L \sigma T$, where L is the Lorenz number ($L = \left(\frac{k_B}{e}\right)^2 \frac{3F_0(\eta)F_2(\eta) - 4F_1(\eta)^2}{F_0(\eta)^2}$)(35). $\kappa_L(T)$ is an input parameter for an SPB model and, for the considered case, it is obtained from experimental data as in (31). A 2D polynomial fit function $\kappa_L(x, T)$ covering the whole compositional range as described in (31) was used.

From all of these temperature dependent parameters the TE properties are obtained. Employing x and n as independent variables matches the experimental reality as a change in x corresponds to an isovalent substitution of Si by Sn and n is adjusted by adding small amounts of dopants (Li substituting Mg in this case); hence x and n can be adjusted basically independent of each other [Mila]. While applying the SPB model, the validity of the assumptions should be discussed. The SPB assumption fails above the temperature at which bipolar conduction becomes relevant *i.e.*, where more than one band contributes significantly to conduction.

Conventionally, the validity range of the SPB model can be judged by visual examination of the Pisarenko plot (21) or by comparing experimental results and calculated SPB model output. Here we have used the shape of the $zT(T)$ curve as a criterion to estimate the validity range as it is related to efficiency. An example zT curve calculated using the SPB model (solid lines) for a composition of $x = 1$, and $n[10^{20} \text{ cm}^{-3}] = 1.51, 2.47$ and 2.68 is compared to the experimental data (dotted lines) in Figure 5-1. For simplicity, the zT maximum, i.e. the point where $\frac{d(zT_{\text{exp}})}{dT} = 0$ was chosen as the validity limit of the SPB model. $\frac{d\alpha}{dT}$ was analyzed for comparison and it was found that the results are very similar, with $\frac{d(zT_{\text{exp}})}{dT}$ being the more conservative limit on average, see Figure S2 in SI. Such data were obtained for a number of samples available from literature (31, 36-38) and the validity limit was interpolated over the whole compositional range. In order to avoid unphysical extrapolation, the maximum validity limit outside the known experimental points was set to 700 K.

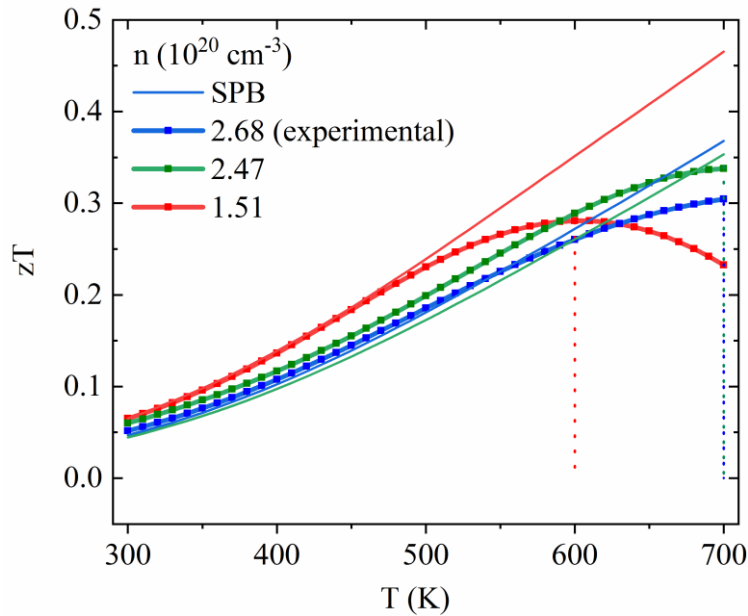


Figure 5-1: Comparison of the interpolated experimental figure of merit and the figure of merit calculated by the SPB model for different carrier concentrations $n=1.51, 2.47$, and $2.68 \times 10^{20} [\text{ cm}^{-3}]$ in p-type Mg_2Sn . The temperature corresponding to the peak (marked) of the experimental zT curves is taken as the validity limit of the SPB model.

Considering a single TE leg with a hot side temperature T_h and a cold side temperature T_c , the device performance, i.e. efficiency and power output, is calculated (17, 35) using the material properties obtained employing the SPB. In the steady-state, the exact temperature profile $T(x)$ obtained by solving the thermoelectric heat balance equation (39, 40) (eq. (68)) is used for

accurate performance calculation of the TEG. In 1D, the heat balance equation is written as (35),

$$\frac{d}{dx} \left(\kappa \frac{dT}{dx} \right) - jT \frac{d\alpha}{dT} \frac{dT}{dx} = -\rho(T)j^2 \quad (68)$$

where j is the current density. The term $\frac{d}{dx} \left(\kappa \frac{dT}{dx} \right)$ corresponds to the Fourier heat flux which also compensates for the locally appearing Joule heat $\rho(T)j^2$ and Peltier-Thomson heat $T \frac{d\alpha}{dT} \frac{dT}{dx}$. The exact solution of eq. (51) is obtained using the iterative procedure described in . From the temperature profile, the exact power and efficiency are obtained as follows:

$$p = V \cdot j \quad (69)$$

where $V = V_o - R_i I$, and $V_o = \int_{T_c}^{T_h} \alpha(T) dT$. Here, p is the electrical output power density given by the product of output voltage V and the current density $j (= \frac{I}{A})$. V consists of the generated Seebeck voltage V_o and the voltage drop due to the internal resistance $R_i = \frac{1}{A} \int_0^l \rho(T(x)) dx$ where A is the cross-sectional area, l the length of the TE leg and $\rho(T)$ the resistivity of the TE material. The efficiency (η) is the ratio of output power density to the inflowing heat flux at the hot side of the TEG leg (q_{in} ; Eq. (55)), where q_{in} is given by (Eq. (56))

$$\eta = p/q_{in} \quad (70)$$

$$q_{in} = -\kappa_h \cdot \frac{dT}{dx_h} + j \cdot \alpha_h \cdot T_h . \quad (71)$$

Here, $-\kappa_h \cdot \frac{dT}{dx_h}$ is the Fourier heat flux into the leg and $j \cdot \alpha_h \cdot T_h$ is the Peltier heat flux absorbed at the hot side. The suffix h indicates the properties at the hot side, i.e., $\kappa_h = \kappa(T_h)$ and $\alpha_h = \alpha(T_h)$. The maximum efficiency or power is obtained by building the η vs. j or p vs. j characteristics, respectively, and finding the maximum (first derivative being zero). This calculation is done for the entire range of composition of p-Mg₂Si_{1-x}Sn_x and carrier concentrations based on the interpolated microscopic parameters $m_D^*(x, n)$ and $\kappa_L(x, T)$.

5.3 Results

The validity limit was obtained as explained in section 5.2 (Figure 5-1) using the experimental data available in literature (31, 36, 38). The full data used is given in Table S1 in the Supplementary info. The data was interpolated using the Thin Plate Spline (TPS) algorithm

available in the Origin software (41) and is shown in Figure 5-2. As expected, as we move from Mg_2Si to Mg_2Sn , the maximum temperature up to which the SPB model is valid reduces for a fixed n , due to the decreasing band gap, and as we move from lower carrier concentrations to higher, the validity limit increases as the contribution of the minority carriers decreases (31, 42). The partially wavy form of the temperature contour lines is due to the input data, which was obtained from different sources and shows the usual experimental scatter.

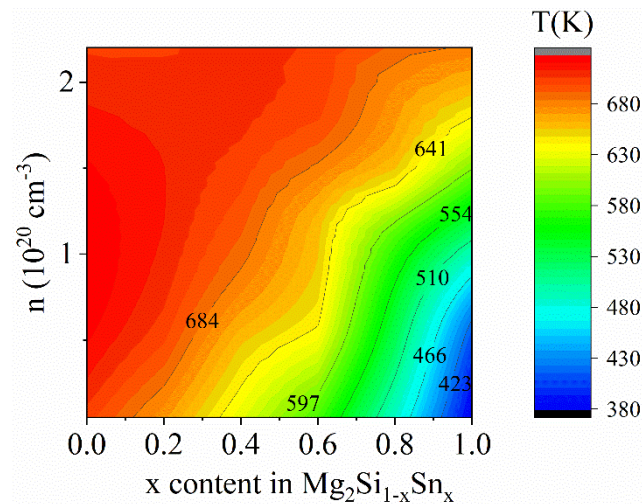


Figure 5-2: Contour plot indicating the temperatures up to which the SPB was applied as function of x and carrier concentration n for p-type $\text{Mg}_2\text{Si}_{1-x}\text{Sn}_x$.

5.3.1 Optimum carrier concentration

Contour plots showing the calculated maximum efficiency for a hot side temperature (T_h) of 500 K and a cold side temperature (T_c) of 300 K as a function of x and n are shown in Figure 5-3a. For comparison to zT_{\max} (Figure 5-3b), zT_{TAV} contours are also plotted in Figure 5-3c, where $zT_{\text{TAV}} = \frac{1}{\Delta T} \int_{T_c}^{T_h} zT(T) dT$ (a physically appropriate temperature average for Seebeck coefficient (but not σ, κ) suggested by Ioffe) (1). Since minority carrier effects are not considered in an SPB model, zT increases monotonously with T and therefore zT_{\max} is the result of the SPB model at the considered hot side temperature (here 500 K). The line for the chosen T_h of 500 K from the validity plot in Figure 5-2 is superimposed onto these plots (the area with SPB valid only up to less than 500 K indicated by the dimmed region) to clarify what part of the modelling results is physically interpretable. Note that the performance maximum near $x = 1$ is thus not accessible. It arises due to the low m_D^* for low n and high x and overcompensates the effect of increasing lattice thermal conductivity for $x \rightarrow 1$, but is outside

the validity range for the SPB model; practically zT is lower here than predicted by the SPB model due to the influence of minority carriers.

As can be seen from Figure 5-3d, the optimum carrier density n_{opt} differs between the calculated efficiency and zT_{max} plots, while n_{opt} from the zT_{TAV} plot coincides approximately with that from the efficiency plot. For efficiency, the maximum is found at $n = 0.44 \times 10^{20} \text{ cm}^{-3}$ for zT_{TAV} , while for zT_{max} , the maximum occurs at $n = 0.54 \times 10^{20} \text{ cm}^{-3}$.

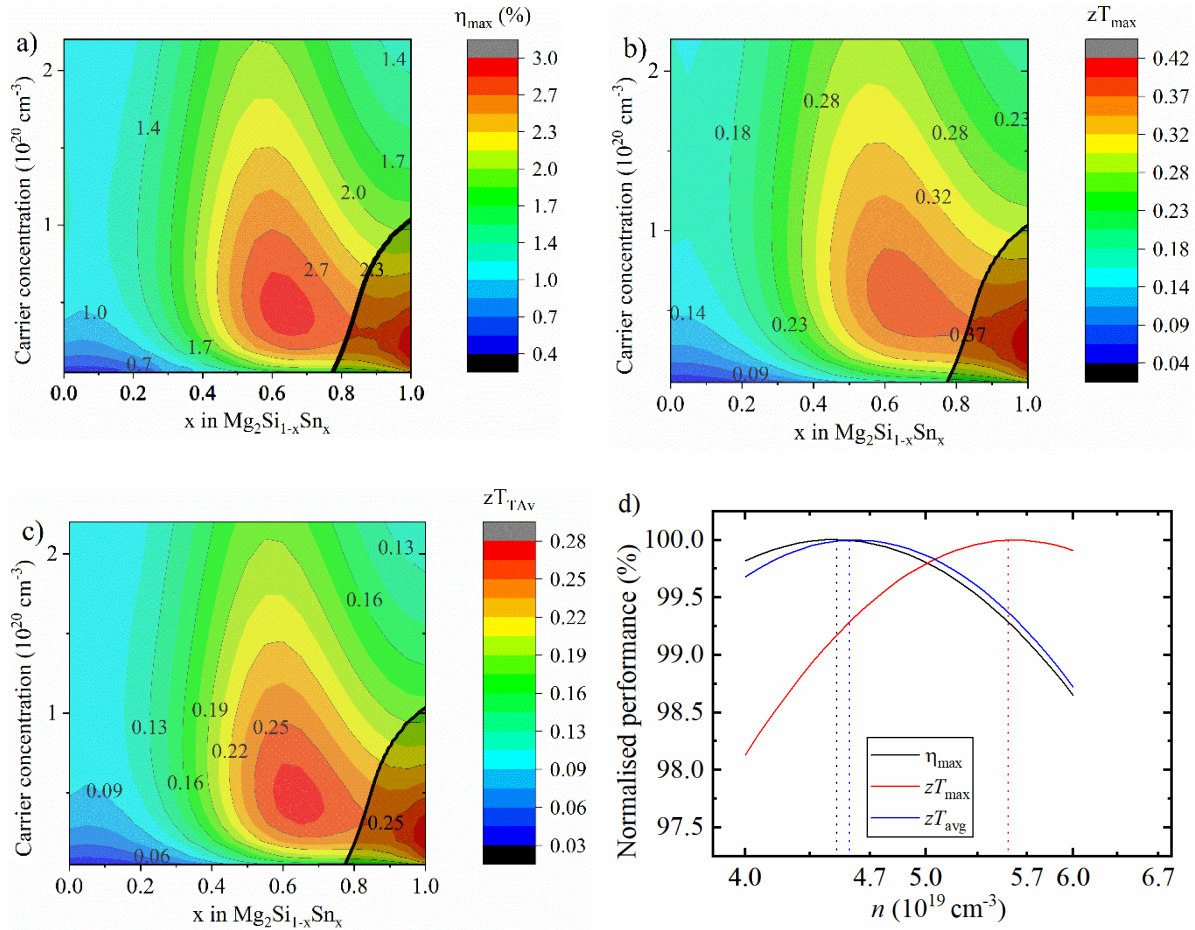


Figure 5-3: a) Maximum calculated efficiency for $T_h = 500 \text{ K}$ and $T_c = 300 \text{ K}$; b) zT at 500 K ; c) zT_{TAV} for $T_h = 500 \text{ K}$ and $T_c = 300 \text{ K}$, for different n and x for p-type $\text{Mg}_2\text{Si}_{1-x}\text{Sn}_x$; the SPB approximation does not hold in the shaded region on the graphs as discussed by Fig 2. d) optimum n with respect to the calculated maximum efficiency ($x = 0.64$), zT_{max} ($x = 0.65$), and zT_{TAV} ($x = 0.64$), all curves normalized to their maximum values.

5.4 Discussion

The necessity to define a validity range is due to employing an SPB model for the efficiency calculation, which naturally fails at higher temperatures due to bipolar contributions. This could be overcome by a multiband description, but so far no multiband model with a good agreement of experimental and modelling data has been published. To date, most modelling approaches were focused on n-type $\text{Mg}_2\text{Si}_{0.4}\text{Sn}_{0.6}$ for which the SPB model is usually valid for a larger temperature range, partially because of the higher mobility of the electrons compared to the holes (4, 43-45). Previous approaches to estimate the validity range of an SPB were based on the analysis of the temperature dependence of the calculated electrochemical potential (31) or approximate two-band modelling (46); using $\frac{d(zT)}{dT}$ as a criterion is a more pragmatic approach. As $\frac{d(zT)}{dT}$ decreases towards higher T , the zT of the model will usually be higher than that of the real sample; hence the efficiency from the SPB model will be too high if the chosen temperature interval includes a range close to the experimental zT_{max} . However, we estimate this maximum relative difference in efficiency to about 10%. From Figure 5-4, it can be seen that the possibility to predict n_{opt} , x_{opt} and the efficiency at the optimum fails beyond a hot side temperature of 610 K, since for higher T_{h} the optimum lies outside the valid region of the employed SPB model. Nevertheless, with an expected maximum application T_{h} of ≈ 700 K, the SPB model can be applied to a significant fraction of the relevant temperature range and the modelling results are of practical relevance.

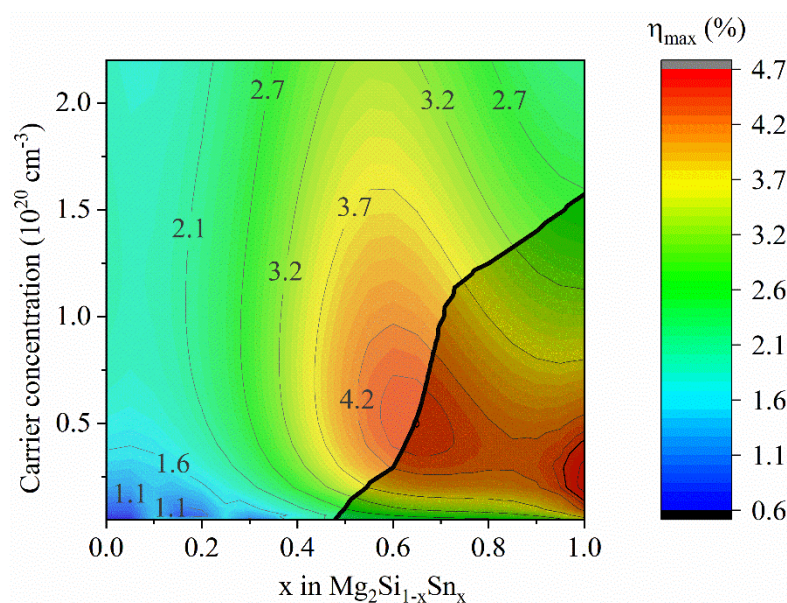


Figure 5-4: Calculated maximum efficiency contours for a cold side temperature of $T_c = 300$ K and hot side temperature T_h of 610 K with the black line showing the validity limit of the SPB model. With increasing distance from the black line into the dimmed region the predicted efficiency is increasingly overestimated as the (detrimental) influence of the minority carriers is not taken into account by the employed SPB model.

From Figure 5-3, it can be seen that the maximum efficiency plot and the zT_{\max} (zT at 500 K) plot do not result in the same optimum region. This is because zT_{\max} is one of the less suitable methods of representing the performance of the TE material (17, 20, 47) and overestimates performance (12). For $T_h = 500$ K, the optimum n determined by zT_{\max} is off from the efficiency prediction by 21% as seen from Figure 5-3.

Figure 5-5a and Figure 5-5b shows the changes in optimum n and x respectively, for $T_h = 400$ K, 500 K, 600 K with $T_c = 300$ K. It can be seen that the optimum n using zT_{\max} is always overestimated and that the discrepancy can be $> 20\%$. Also, as expected, the discrepancy reduces as the temperature interval gets smaller, i.e. tending towards the constant properties model. A similar trend but much weaker in magnitude is observed in the case of zT_{TAV} . There is no significant difference in optimum x with respect to the exact efficiency and zT_{TAV} and zT_{\max} as seen from Figure 5-4b. Analyzing Figure 5-5a and Figure 5-3d it can be concluded that the shift in the optimum n with T_h is for p-Mg₂Si_{1-x}Sn_x of minor practical relevance. The maximum of $\eta(n)$ is wide, and hence a deviation from n_{opt} by even 20% will mean a performance loss of only about 1.5%. Similar for $\eta(x)$, a mean composition near 0.635 would be suitable for all T_h for p-Mg₂Si_{1-x}Sn_x.

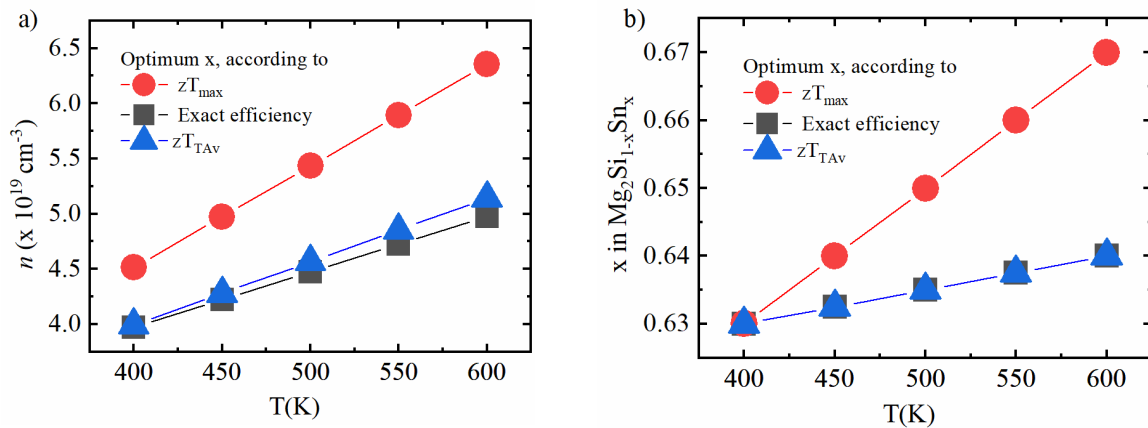


Figure 5-5: a) Change in optimum carrier density n and b) optimum composition x , estimated using zT_{\max} , zT_{TAV} and exact efficiency.

The optimum parameters obtained with zT_{TAV} plots almost coincide with those from the efficiency plots. This is because the basic input SPB parameters (m_D^* , deformation potential constant (E_{Def}), κ_L) do not vary erratically with x and n for the considered material. However, to see if the optimum position (x, n) predicted by CPM (using zT_{TAV} or zT_{max} in the efficiency formula) is different from that of exact efficiency, it is important to see how the parameters that determine this discrepancy between CPM and exact calculation vary with n and x , rather than considering the discrepancy in the obtained efficiency value between CPM and the exact calculation. This is because even though the discrepancy between the CPM and exact efficiency might be quite large, the change of the factors that determine this discrepancy, for different n and x , might be constant or negligibly varying, leading to the same optimum position (x, n) in both cases, i.e., the parameters to be optimized (n and x in our case) can often nevertheless be obtained with high accuracy using CPM. A large discrepancy might be expected if the difference between CPM and exact efficiency is itself a strong function of n and x .

Additionally, as a comparison, the optimum parameters obtained for n-type $Mg_2Si_{1-x}Sn_x$ (48) and PbTe (49) using zT_{TAV} and exact efficiency are shown along with p-type $Mg_2Si_{1-x}Sn_x$ in Figure S3 of the SI (normalized efficiency and zT_{TAV} are presented). As can be seen, the width of the η and zT_{TAV} curves vs n varies from case to case, and zT_{TAV} predicts the optimum n very similar to exact efficiency in all cases.

If an SPB model is employed to describe the thermoelectric properties, it is presumably rare to see a material case where zT_{TAV} cannot be used to predict optimum parameters since it doesn't include any intrinsic carrier effects. The accuracy of efficiency prediction by CPM varies with a qualitative change in the slope and curvature of the TE properties on T . In particular, these vary with the relative relevance of bipolar effects (12, 16, 17). With constant or moderately changing parameters of a SPB model there won't be qualitative changes in the curve shape of the TE properties: $\alpha(T)$ and $\rho(T)$ will rise approximately linearly and $\kappa(T)$ will decrease approximately as $\kappa \propto \frac{c_1}{T} + c_2$ (22, 50). The relation between the chosen mode of zT definition and the physically justified Ioffe ZT (from the adequate averages of Seebeck and resistivities) will be quite stable under these conditions and also the distribution of Joule and Thomson heat, as discussed, will not vary a lot, as it is more the change of slope of the properties with T rather than their absolute magnitude which makes the effects here. With that there is good reason to trust in that if zT_{TAV} gives a very good match in two examples it would do so for many more

materials; zT_{TAV} can thus be a convenient alternative if the SPB model can be employed. However, in order to achieve higher efficiency, higher temperatures where bipolar conduction occurs are usually employed for applications and hence the SPB assumption and therefore zT_{TAV} can prove to be ineffective due to the stronger change of temperature dependence of the transport properties. Note also, that even though zT_{TAV} apparently can be used to identify the optimum carrier concentration, it can show quite some inaccuracy for the calculation of efficiency itself (12, 16, 17). Finally, the approach shown here can relatively easily be upgraded to a p-n couple (22) and electrical and thermal contact resistances can be implemented. Then the approach shown here helps for an accurate estimation of device efficiency and optimized material properties under realistic application conditions. Employing the efficiency derived from the temperature dependent properties (Eq 8??) allows for an optimization with respect to n in scenarios when the area adjustment (18) to accommodate for different currents in p and n leg cannot be done for some practical reason or when contact resistances play a large role.

5.4.1 Summary and outlook

A simple and efficient tool to predict the exact optimum composition of the solid solution and optimum carrier density has been shown using p-Mg₂Si_{1-x}Sn_x as an example. This approach is applicable to any material for which a description of the thermoelectric properties is given. This is demonstrated exemplarily by Figure.S3 in the supporting material, where the efficiency (normalized) vs n curves for PbTe and n-Mg₂Si_{0.4}Sn_{0.6} has been provided. The difference in optimum carrier concentration obtained using commonly used indicators such as zT_{max} or zT_{TAV} vs the optimum obtained considering the locally varying thermoelectric properties for p-Mg₂X has been discussed. Even though the discrepancy in calculated efficiency between CPM and exact calculations exists, for some materials like the one considered here, zT_{TAV} can be used to find optimum carrier concentration and composition with good accuracy for practical use.

In practice, to reach maximum efficiency, hot side temperatures entering the range of bipolar conduction are important, and to model such cases, multi band models are necessary. With the shown TEG calculation routine, the effect of having metal contacts and its effect on optimum parameters can be easily implemented and studied. The combination of a semiconductor physics model such as SPB and continuum theoretical efficiency calculation can also be employed to optimize material grading or segmentation for further performance enhancement.

Acknowledgements

We would like to gratefully acknowledge the endorsement from the DLR Executive Board Member for Space Research and Technology and the financial support from the Young Research Group Leader Program. PP would like to acknowledge the German Academic Exchange Service, DAAD (Fellowship No. 247/2017) for financial support.

Bibliography for chapter 5 (paper 3)

1. Ioffe AF, Stil'Bans L, Iordanishvili E, Stavitskaya T, Gelbtuch A, Vineyard GJP. Semiconductor thermoelements and thermoelectric cooling. 1959;12(5):42.
2. Snyder GJ, Toberer ES. Complex thermoelectric materials. *Materials For Sustainable Energy: A Collection of Peer-Reviewed Research and Review Articles from Nature Publishing Group*; World Scientific; 2011. p. 101-10.
3. Rogl G, Rogl P. Skutterudites, a most promising group of thermoelectric materials. *Curr Opin Green Sust.* 2017;4:50-7.
4. Mao J, Wu YX, Song SW, Zhu Q, Shuai J, Liu ZH, et al. Defect Engineering for Realizing High Thermoelectric Performance in n-Type Mg₃Sb₂-Based Materials. *ACS Energy Lett.* 2017;2(10):2245-50.
5. Wang Y, Zhang X, Liu YQ, Wang YZ, Zhang JX, Yue M. Optimizing the thermoelectric performance of p-type Mg₃Sb₂ by Sn doping. *Vacuum.* 2020;177:109388.
6. Pei Y, Shi X, LaLonde A, Wang H, Chen L, Snyder GJ. Convergence of electronic bands for high performance bulk thermoelectrics. *Nature.* 2011;473(7345):66-9.
7. Goldsmid HJ. Bismuth Telluride and Its Alloys as Materials for Thermoelectric Generation. *Materials (Basel).* 2014;7(4):2577-92.
8. Chen ZG, Shi XL, Zhao LD, Zou J. High-performance SnSe thermoelectric materials: Progress and future challenge. *Prog Mater Sci.* 2018;97:283-346.
9. de Boor J, Dasgupta T, Müller E. Thermoelectric properties of magnesium silicide based solid solutions and higher manganese silicides: CRC Press, Taylor & Francis Group Boca Raton, NW, USA; 2016.
10. Hu C, Xia K, Chen X, Zhao X, Zhu T. Transport mechanisms and property optimization of p-type (Zr, Hf) CoSb half-Heusler thermoelectric materials. *Mater Today Phys.* 2018;7:69-76.
11. Zeier WG, Schmitt J, Hautier G, Aydemir U, Gibbs ZM, Felser C, et al. Engineering half-Heusler thermoelectric materials using Zintl chemistry. *Nat Rev Mater.* 2016;1(6):1-10.
12. Ponnusamy P, de Boor J, Muller E. Discrepancy between Constant Properties Model and Temperature-Dependent Material Properties for Performance Estimation of Thermoelectric Generators. *Entropy-Switz.* 2020;22(10):1128.
13. Sherman B, Heikes R, Ure Jr R. Calculation of efficiency of thermoelectric devices. *J Journal of Applied Physics.* 1960;31(1):1-16.
14. Sunderland JE, Burak NT. The influence of the Thomson effect on the performance of a thermoelectric power generator. *J Solid-State Electronics.* 1964;7(6):465-71.
15. Wee D. Analysis of thermoelectric energy conversion efficiency with linear and nonlinear temperature dependence in material properties. *Energ Convers Manage.* 2011;52(12):3383-90.

16. Ryu B, Chung J, Park S. Thermoelectric efficiency has three Degrees of Freedom. J arXiv preprint arXiv:11148. 2018.
17. Ponnusamy P, de Boor J, Müller E. Using the constant properties model for accurate performance estimation of thermoelectric generator elements. *Applied Energy*. 2020;262:114587.
18. Goupil C. *Continuum theory and modeling of thermoelectric elements*: John Wiley & Sons; 2015.
19. Kim HS, Liu WS, Ren ZF. The bridge between the materials and devices of thermoelectric power generators. *Energ Environ Sci*. 2017;10(1):69-85.
20. Lau PG, Buist RJ, editors. *Calculation of thermoelectric power generation performance using finite element analysis*. XVI ICT'97 Proceedings ICT'97 16th International Conference on Thermoelectrics (Cat No 97TH8291); 1997: IEEE.
21. Naithani H, Dasgupta T. Critical Analysis of Single Band Modeling of Thermoelectric Materials. *ACS Applied Energy Materials*. 2019;3(3):2200-13.
22. Rowe DM. *Thermoelectrics and its Energy Harvesting, 2-Volume Set*: CRC press; 2018.
23. Bulusu A, Walker DG. Review of electronic transport models for thermoelectric materials. *Superlattice Microst*. 2008;44(1):1-36.
24. Zhang L, Xiao P, Shi L, Henkelman G, Goodenough JB, Zhou J. Suppressing the bipolar contribution to the thermoelectric properties of $\text{Mg}_2\text{Si}_{0.4}\text{Sn}_{0.6}$ by Ge substitution. *Journal of Applied Physics*. 2015;117(15):155103.
25. Mao J, Liu W, Ren Z. Carrier distribution in multi-band materials and its effect on thermoelectric properties. *Journal of Materiomics*. 2016;2(2):203-11.
26. Sankhla A, Patil A, Kamila H, Yasseri M, Farahi N, Mueller E, et al. Mechanical alloying of optimized $\text{Mg}_2(\text{Si}, \text{Sn})$ solid solutions: understanding phase evolution and tuning synthesis parameters for thermoelectric applications. *ACS Applied Energy Materials*. 2018;1(2):531-42.
27. Goyal GK, Mukherjee S, Mallik RC, Vitta S, Samajdar I, Dasgupta T. High Thermoelectric Performance in $\text{Mg}_2(\text{Si}_{0.3}\text{Sn}_{0.7})$ by Enhanced Phonon Scattering. *J ACS Applied Energy Materials*. 2019;2(3):2129-37.
28. Pham NH, Farahi N, Kamila H, Sankhla A, Ayachi S, Muller E, et al. Ni and Ag electrodes for magnesium silicide based thermoelectric generators. *Mater Today Energy*. 2019;11:97-105.
29. Ayachi S, Deshpande R, Ponnusamy P, Park S, Chung J, Park S, et al. On the Relevance of Point Defects for the Selection of Contacting Electrodes: Ag as an Example for $\text{Mg}_2(\text{Si}, \text{Sn})$ -based Thermoelectric Generators. *Mater Today Phys*. 2020:100309.
30. Kamila H, Sankhla A, Yasseri M, Hoang N, Farahi N, Mueller E, et al. Synthesis of p-type $\text{Mg}_2\text{Si}_{1-x}\text{Sn}_x$ with $x = 0-1$ and optimization of the synthesis parameters. *Materials Today: Proceedings*. 2019;8:546-55.
31. Kamila H, Sahu P, Sankhla A, Yasseri M, Pham H-N, Dasgupta T, et al. Analyzing transport properties of p-type $\text{Mg}_2\text{Si}-\text{Mg}_2\text{Sn}$ solid solutions: optimization of thermoelectric

performance and insight into the electronic band structure. *Journal of Materials Chemistry A*. 2019.

32. Bux SK, Yeung MT, Toberer ES, Snyder GJ, Kaner RB, Fleurial JP. Mechanochemical synthesis and thermoelectric properties of high quality magnesium silicide. *J Mater Chem*. 2011;21(33):12259-66.

33. Liu W, Chi H, Sun H, Zhang Q, Yin K, Tang X, et al. Advanced thermoelectrics governed by a single parabolic band: $\text{Mg}_{2-x}\text{Si}_{0.3}\text{Sn}_{0.7}$, a canonical example. *Physical Chemistry Chemical Physics*. 2014;16(15):6893-7.

34. de Boor J, Dasgupta T, Saparamadu U, Müller E, Ren Z. Recent progress in p-type thermoelectric magnesium silicide based solid solutions. *Mater Today Energy*. 2017;4:105-21.

35. Rowe DM. *Thermoelectrics handbook: macro to nano*. CRC press; 2005.

36. Liu W, Yin K, Su X, Li H, Yan Y, Tang X, et al. Enhanced hole concentration through Ga doping and excess of Mg and thermoelectric properties of p-type $\text{Mg}_{2(1+z)}(\text{Si}_{0.3}\text{Sn}_{0.7})_{1-y}\text{Ga}_y$. *Intermetallics*. 2013;32:352-61.

37. Isoda Y, Tada S, Nagai T, Fujiu H, Shinohara Y. Thermoelectric properties of p-type $\text{Mg}_{2.00}\text{Si}_{0.25}\text{Sn}_{0.75}$ with Li and Ag double doping. *Journal of Electronic Materials*. 2010;39(9):1531-5.

38. Isachenko G, Samunin AY, Gurieva E, Fedorov M, Pshenay-Severin D, Konstantinov P, et al. Thermoelectric Properties of Nanostructured p- $\text{Mg}_{2-x}\text{Si}_x\text{Sn}_{1-x}$ ($x=0.2$ to 0.4) Solid Solutions. *Journal of Electronic Materials*. 2016;45(3):1982-6.

39. Domenicali CA. Stationary temperature distribution in an electrically heated conductor. *Journal of Applied Physics*. 1954;25(10):1310-1.

40. Domenicali CA. Irreversible thermodynamics of thermoelectric effects in inhomogeneous, anisotropic media. *J Physical Review*. 1953;92(4):877.

41. Donato G, Belongie SJ. *Approximation methods for thin plate spline mappings and principal warps*: Citeseer; 2003.

42. Zhang Q, Cheng L, Liu W, Zheng Y, Su X, Chi H, et al. Low effective mass and carrier concentration optimization for high performance p-type $\text{Mg}_{2(1-x)}\text{Li}_{2x}\text{Si}_{0.3}\text{Sn}_{0.7}$ solid solutions. *Physical Chemistry Chemical Physics*. 2014;16(43):23576-83.

43. Bahk JH, Bian ZX, Shakouri A. Electron transport modeling and energy filtering for efficient thermoelectric $\text{Mg}_2\text{Si}_{1-x}\text{Sn}_x$ solid solutions. *Phys Rev B*. 2014;89(7):075204.

44. Satyala N, Vashaee D. Modeling of Thermoelectric Properties of Magnesium Silicide (Mg_2Si). *J Electron Mater*. 2012;41:1785-91.

45. Zhang L, Xiao P, Shi L, Henkelman G, Goodenough JB, Zhou J. Suppressing the bipolar contribution to the thermoelectric properties of $\text{Mg}_2\text{Si}_{0.4}\text{Sn}_{0.6}$ by Ge substitution. *Journal of Applied Physics*. 2015;117(15):155103.

46. de Boor J, Berche A, Jund P. Density of States Effective Mass for p-Type $\text{Mg}_2\text{Si-Mg}_2\text{Sn}$ Solid Solutions: Comparison between Experiments and First Principles Calculations. *The Journal of Physical Chemistry C*. 2020.

47. Kim HS, Liu W, Ren Z. The bridge between the materials and devices of thermoelectric power generators. *Energy & Environmental Science*. 2017;10(1):69-85.

48. Sankhla A, Kamila H, Kelm K, Mueller E, de Boor JJAM. Analyzing thermoelectric transport in n-type $\text{Mg}_2\text{Si}_{0.4}\text{Sn}_{0.6}$ and correlation with microstructural effects: An insight on the role of Mg. 2020;199:85-95.
49. Pei Y, LaLonde A, Iwanaga S, Snyder GJ. High thermoelectric figure of merit in heavy hole dominated PbTe. *Energy and Environmental Science*. 2011;4(6):2085-9.
50. Uher C. *Materials aspect of thermoelectricity*: CRC press; 2016.
51. Fistul VI. *Heavily doped semiconductors*: Springer Science & Business Media; 2012.
52. Liu W, Tan X, Yin K, Liu H, Tang X, Shi J, et al. Convergence of conduction bands as a means of enhancing thermoelectric performance of n-type $\text{Mg}_2\text{Si}_{1-x}\text{Sn}_x$ solid solutions. *Physical review letters*. 2012;108(16):166601.
53. Kaviany M. *Heat transfer physics*: Cambridge University Press; 2014.
54. Kim S, Wiendlocha B, Jin H, Tobola J, Heremans JP. Electronic structure and thermoelectric properties of p-type Ag-doped Mg_2Sn and $\text{Mg}_2\text{Sn}_{1-x}\text{Six}$ ($x=0.05, 0.1$). *Journal of Applied Physics*. 2014;116(15):153706.

Supplementary Information (SI)

SPB relevant quantities

The mobility due to acoustic phonon scattering (μ_0^{AP}) (51) and alloy scattering (μ_0^{AS}) (52) are given as follows,

$$\mu_0^{AP} = \frac{\pi\sqrt{8}e\hbar^4\rho v_1^2}{4E_{Def}^2(m_s)^{2.5}(k_B T)^{1.5}} \quad \text{and} \quad \mu_0^{AS} = \frac{16e\hbar^4 N_0}{3(2)^{1.5}\pi x(1-x)E_{AS}^2(m_s)^{2.5}(k_B T)^{0.5}}$$

where ρ is the theoretical (mass) density, v_1 is the longitudinal sound velocity both assumed to vary linearly from Mg₂Si to Mg₂Sn as in (31). N_0 is the number of atoms per unit volume, m_s is the single valley effective mass, E_{Def} is the deformation potential constant, E_{AS} is the alloy scattering parameter. These constants were taken exactly as in (31).

According to Matthiessen's rule (33, 53), the total mobility when the contributing scattering mechanisms are considered to be independent of each other is given by

$$\frac{1}{\mu_0} = \frac{1}{\mu_0^{AP}} + \frac{1}{\mu_0^{AS}}, \quad \text{where } \mu_H = \mu_0 \frac{F-0.5}{2F_0}, \quad \mu_H \text{ is the Hall mobility.}$$

Fitting of the effective mass:

Table S2: Data that was used for fitting m_D^* and the fitted results: linear fit with x , as well as bilinear fit with x and n along with the error %.

For the bilinear fit, a goodness of fit value of 92.9% was obtained and for a linear fit it was 82.5%.

x	n (10^{20} cm^{-3})	Raw data (31)	Fitted (bilinear)	Relative deviation (%)- bilinear fit	Fitted (linear)	Relative deviation (%)-linear fit
Equation:			$(2.14 - 1.39 x + 0.16 \times 10^{-20} \text{ cm}^3 n) m_0$		$(2.2 - 1.1 x) m_0$	
0	0	2.2	2.14	-2.85	2.2	0.00
0.6	0.57	1.45	1.39	-4.07	1.54	6.21
0.6	0.95	1.42	1.45	2.23	1.54	8.45
0.6	1.2	1.53	1.49	-2.55	1.54	0.65
0.8	1.24	1.01	1.22	17.21	1.32	30.69
0.8	1.45	1.18	1.25	5.82	1.32	11.86
0.8	1.93	1.26	1.33	5.22	1.32	4.76
0.8	0.4	1.01	1.09	7.11	1.32	30.69
1	0.73	0.95	0.86	-13.57	1.1	-1.79

1	1.52	1.12	0.99	-3.05	1.1	-5.98
1	2.47	1.17	1.14	-4.05	1.1	-9.84
1	2.7	1.22	1.17	-10.48	1.1	15.79

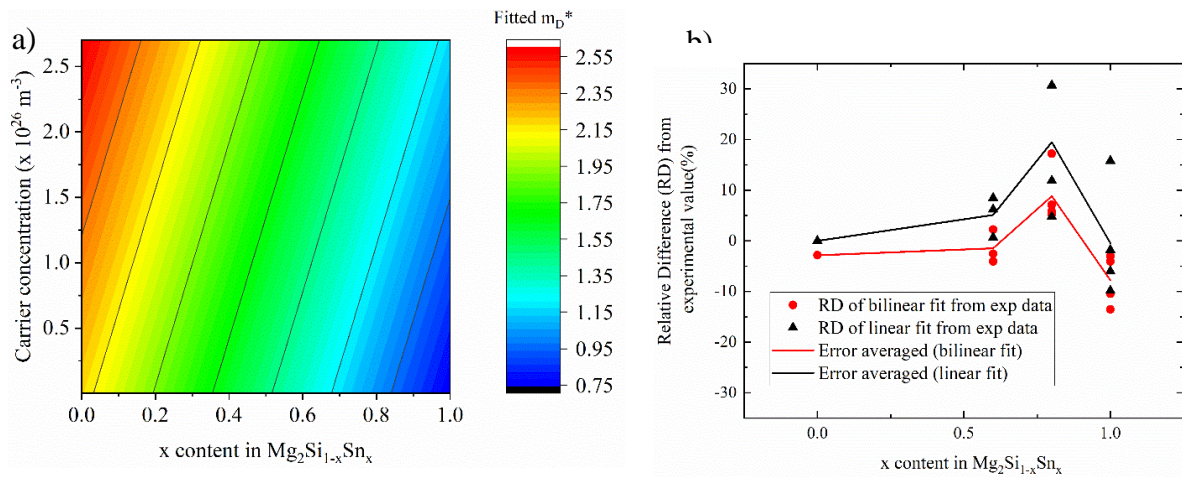


Figure S1: a) Bilinear fit for m_D^* with x and n . b) Relative difference (RD) of the linearly and bilinearly fitted m_D^* from experimental data. Different points for each x indicate different samples. Bilinear fit has considerably lower deviation from experimental m_D^* .

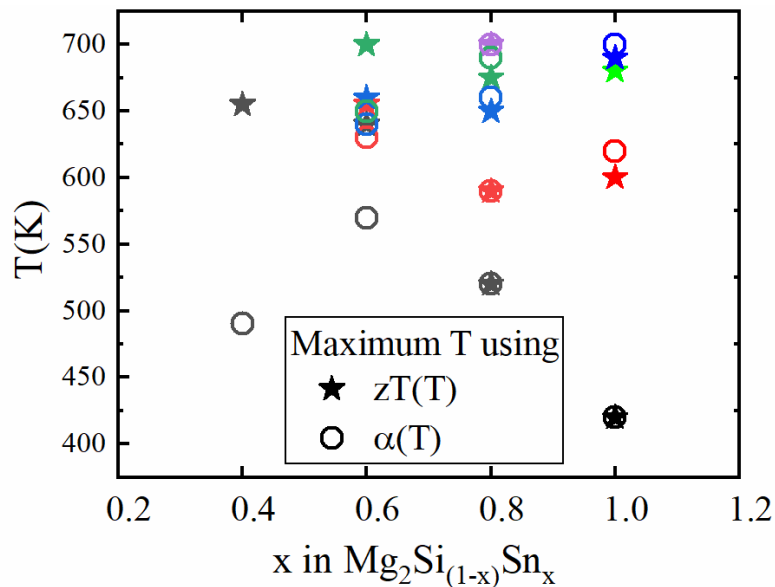


Figure S2: Validity limits calculated using the experimental zT curve and the experimental Seebeck coefficient curve, the markers correspond to $\frac{dzT(T)}{dT} = 0$ and $dS/dT=0$, respectively. The colours indicate different samples (with different carrier concentrations that are listed in Table 3 below). At higher x

values $d(zT)/dT$ gives a lower validity limit than the Seebeck curve and hence zT is considered as the more conservative validity limit.

Table S4: Experimental data used for interpolation of the validity range of the employed SPB model. T corresponds to $dzT/dT = 0$ and indicates the maximum temperature up to which SPB can be employed for that sample.

x	Reference	n (10^{20} cm^{-3})	T (K)
0		2.5	700
0.2		0.5	700
0.4	(31)	0.47	655
0.6		0.57	640
0.6		0.95	655
0.6		1.20	660
0.6	(38)	1.80	700
0.8	(31)	0.40	520
0.8		1.15	590
0.8		1.45	650
0.8		1.93	675
0.8	(38)	3.20	700
1	(54)	0.60	420
1	(31)	1.51	600
1		2.47	700
1		2.68	700

These temperatures are obtained by finding the temperature corresponding to zT_{max} . As we move along an increasing n the validity limit would be higher and higher as seen. Similarly, as we move along the x grid for a fixed n , the validity limit decreases from Mg_2Si to Mg_2Sn due to decreasing band gap along x .

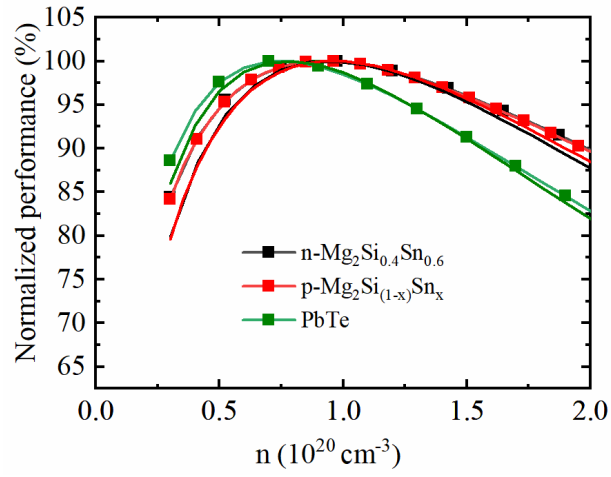


Figure S3: Normalized η (symbol + line) and zT_{TAV} (solid line) vs n for $T_h=600 \text{ K}, T_c=300\text{K}$ for p-type $\text{Mg}_2\text{Si}_{1-x}\text{Sn}_x$, n-type $\text{Mg}_2\text{Si}_{0.4}\text{Sn}_{0.6}$ (48) and PbTe (6).

6 Discussion

So far, we have seen the problems involved with the use of CPM in assessing module performance as well as in material optimisation. Even though a correction for considering the Thomson heat in CPM was suggested, the error associated with the asymmetry in heat distribution still exists and it could be high for strongly temperature dependent materials. Therefore, it is suggested to stick with the quick fully temperature dependent 1D iterative solution for exact performance estimation and for material optimisation.

Previously in Chapter 5 we employed the TE leg efficiency (based on temperature dependent material properties) directly as a parameter for n optimisation using a combined material-device model [13, 14, 18]. The methodology was shown using $\text{Mg}_2(\text{Si},\text{Sn})$ solid solutions as an example. An SPB model was used to model the material properties and it was confirmed that $n_{\text{opt},zT}$ at e.g. the hot side temperature is significantly different from the optimum n determined by maximizing efficiency over the temperature range of application $n_{\text{opt},\eta}(= \max_n (\eta(n, T_c, T_h)))$ and the differences were quantified.

Usually, the zT of a thermoelectric material approaches its maximum in the temperature curve $zT(T)$ when minority carriers start to become excited to a significant extent and influence the transport properties visibly and hence a SPB model as used in Chapter 5 becomes unreliable here. To overcome this, at least a two-band model is required, one band to account for majority and minority carriers, each. Since most of the n optimization studies use $zT_{\text{max},n}$ at fixed temperatures to optimize n [78, 80, 102-109], we again analyze the use $zT_{\text{max},n}$ at fixed temperatures and also the temperature averaged zT ($zT_{\text{Tav}} = \frac{1}{T_h - T_c} \int_{T_c}^{T_h} z(T)T dT$, over the temperature range of application of the device) and compare with the results from using efficiency, using a realistic two band model.

In addition, the advantage of this combined material-device model is demonstrated by studying the effect of material grading. Functional material grading involves tuning the material properties spatially along the arbitrary length (x) of the TE leg, to achieve a gain in functionality, power or efficiency [28, 110-113]. There have been some models to predict the gain in thermoelectric performance of such functionally graded materials [114-119], as well as several advanced experimental techniques that have practically made them feasible [110, 111,

120-123]. While more complex grading is in principle feasible, the practically easiest is a mere optimization of the $n(x)$ profile as this can be achieved by tailoring the dopant concentration profile of the material. This leaves the material chemically quite homogeneous and also does not affect the lattice thermal conductivity a lot (if neglecting a minor effect due to point defect scattering). Here, grading is done using $n_{\text{opt},zT}(T)$ for each temperature (or position) along the length of the TE leg, and the corresponding local properties based on this $n_{\text{opt},zT}(T)$. In order to verify if such a graded material has the highest possible efficiency, the compatibility criterion as explained in the introduction (Section 1.5.1) [18, 99, 101, 124] is checked.

We have chosen n-type Mg_2Sn as an example material since it is an end member of the Mg_2Si - Mg_2Sn solid solution series, a promising class of TE materials [125-127], and has received interest as a potential TE material due to its relatively high power factor for both n- and p-type material [127-130]. Even though the method is presented here for Mg_2Sn , it can be applied to any material system using suitable physical models to predict TE properties.

The basic methodology of a combined material-device model was established in Chapter 5 [131] using a SPB model. For a more realistic modeling of the material properties including bipolar effects at high temperatures the SPB model was replaced by a two-parabolic-band model to adequately describe the thermoelectric properties $\alpha(T, n)$, $\sigma(T, n)$, $\kappa(T, n)$ of Mg_2Sn . Using this model, it is straightforward to study the effects of different spatial profiles of n i.e., $n(x)$ profiles along the length of the TE leg. The two-band model developed by H. Naithani *et al.* [132] is used here. The relevant material parameters and equations are given below.

For each carrier type [88], $|\alpha|$, σ , κ , μ_{0AP} and n are calculated according to the equations given in Chapter 5. These constants were taken exactly as in [132].

For a two-band model, $n_A + n = n_D + p$, where n_A denotes the ionized acceptor impurity concentration and n_D is the ionized donor impurity concentration, n and p correspond to the charge carrier concentration for n and p type respectively.

$$\alpha = \frac{\alpha_{\text{CB}}\sigma_{\text{CB}} + \alpha_{\text{VB}}\sigma_{\text{VB}}}{\sigma_{\text{CB}} + \sigma_{\text{VB}}} \quad (72)$$

$$\sigma = \sigma_{\text{CB}} + \sigma_{\text{VB}} \quad (73)$$

$$R_H = \frac{R_{H,\text{CB}}\sigma_{\text{CB}}^2 + R_{H,\text{VB}}\sigma_{\text{VB}}^2}{(\sigma_{\text{CB}} + \sigma_{\text{VB}})^2} \quad (74)$$

$$\kappa_e = \kappa_{e,CB} + \kappa_{e,CB} + \frac{\sigma_{CB}\sigma_{VB}}{\sigma_{CB} + \sigma_{VB}} (\alpha_{CB} - \alpha_{VB})^2 T \quad (75)$$

Here, CB-conduction Band, VB-Valence Band, κ_e -electronic part of thermal conductivity, R_H - Hall coefficient.

The basic idea of segmenting and material grading (continuous segmentation) is presented schematically in Figure 6-2 as introduced in chapter 1. A TE leg of length L connected to an external load resistor R_L is shown. When a temperature difference is applied, a temperature profile ($T(x)$) develops over the TE leg [28, 133]. This $T(x)$ is in principle non-linear due to the temperature dependence of κ as well as the Joule and Thomson effects as discussed in the previous Chapters [28, 133], but as discussed later and shown in Figure 6-1, the deviation from linearity is relatively small.

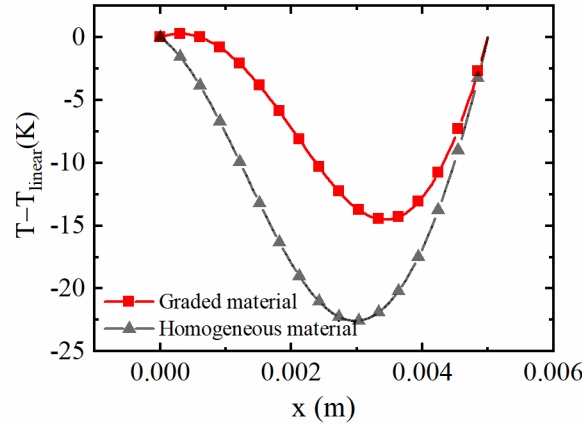


Figure 6-1: T profile bending beyond linearity for graded and homogenous material. Since the maximum possible deviation is only about 22 K, the $n_{opt}(T)$ was found simply for a linear T profile instead of iterating the procedure with the actual T profile. It should also be pointed out that for the considered case the $T(x)$ of the graded sample is more linear than that of the optimum homogeneous material.

Since $n_{opt,zT}$ varies with temperature, a gain in efficiency is possible when the *a priori* unknown optimum n is set along the length of the TE leg according to the temperature at each position in the leg. As η is a monotonous function of zT , choosing $n(x)$ according to the n that maximizes zT locally is a plausible strategy. Since $T(x)$ is not far from linearity in a TEG, the temperature dependence in $n_{opt}(T)$ can be translated directly into the required spatial dependence, i.e. $n(x) = \max_n (zT(n, T(x))) =: n_{opt,zT}(T)$ assuming a linear $T(x)$. For better accuracy, it is possible to find the $n_{opt,zT}$ according to the exact $T(x)$ of the TE leg i.e., $n_{opt,zT}(T(x))$, by iterating the calculation routine [134], required for materials with highly bent

temperature profiles [135], however it is avoided here to minimize the computation time. For segmentation, the TE leg is divided into a number of sections along the length of the TE leg and $n_{\text{opt},\eta}$ is obtained for each section considering the hot and cold side temperatures of that section.

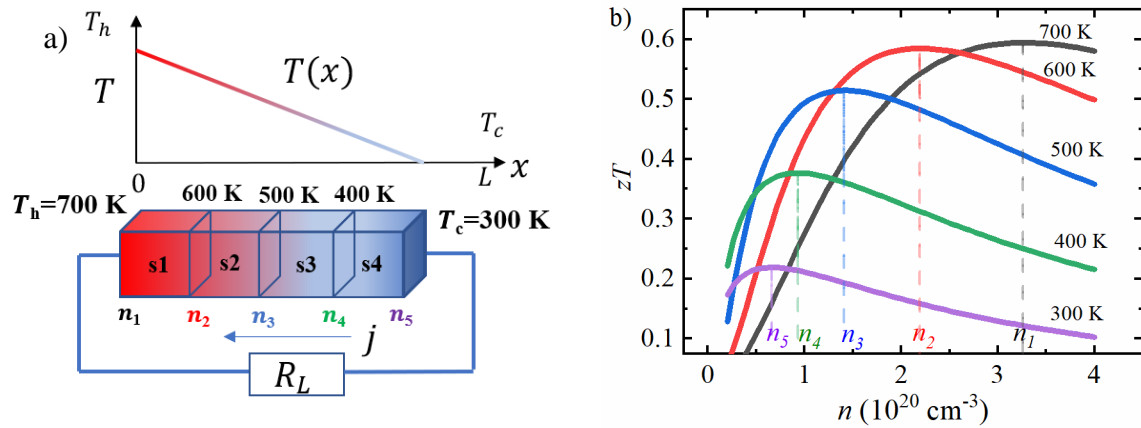


Figure 6-2: a) Schematic of a TE leg connected to an external load resistor R_L with an applied temperature difference $\Delta T = T_h - T_c$. Taking the shown linear $T(x)$ as a starting point, the $n(x)$ for a graded sample is chosen according to the $n_{\text{opt},zT}$ (optimum n based on $zT_{\text{max},n}$). For segmentation, $n_{\text{opt},\eta}$ for each section i (e.g., $T_{h,s1}=700\text{K}-T_{c,s1}=T_{h,s2}=600$ K and so on) is used, b) Optimum n according to zT ($n_{\text{opt},zT}$) is found for each T and the properties corresponding to $n_{\text{opt},zT}(T)$ are set at each temperature point, dashed vertical lines indicate the corresponding optimum n .

For grading Mg_2Sn , zT vs. n characteristics at different temperatures are shown in Figure 6-1b. The obtained $n_{\text{opt},zT}(T)$ profile is superimposed over the TE leg spatially and the properties corresponding to n_{opt} at each temperature then make up the spatially dependent properties of the graded material. For example, if $n_{\text{opt},zT}$ is n_1 at 700 K as shown in Figure 6-1a, then $\alpha(700 \text{ K}) = \alpha(n_1)$ at 700 K and similarly $\alpha(n_2)$ at 600 K and so on, forming the temperature dependent properties of the graded TE leg. For segmentation, the material properties corresponding to $n_{\text{opt},\eta}$ for each section are set. For example, if n_{s1} is the optimum n for a section 700 K- 500 K, then α for the temperatures between 700 - 500 K is given by $\alpha(T, n_{s1})$. Here again, a linear $T(x)$ is assumed for calculation of the n_s values and hence, for this particular example, 500 K corresponds to the mid-point of the TE leg.

Then, the efficiency and/or power output for this graded or segmented material is calculated using the iterative procedure described in Chapter 3 [133], and compared with the

homogeneous material. The maximum efficiency and power output are obtained as explained in the previous Chapters.

6.1 Optimum carrier concentration

The pink curve in Figure 6-2 shows $n_{\text{opt},zT}(T)$ obtained based on the results shown in Figure 6-1b. As a comparison, the $n_{\text{opt},\eta}$ for a homogeneous material [131, 133] (black curve) and zT_{TAV} (i.e. $n_{\text{opt},zT_{\text{TAV}}} = \max_n (zT_{\text{TAV}}(n, T_c, T_h))$, blue curve) for the considered temperatures as T_h with a T_c of 300 K is also shown. It can be seen that $n_{\text{opt},\eta}(T_c, T_h)$ is quite different from $n_{\text{opt},zT}(T_h)$ with a maximum relative overestimation of about 86% for $T_h = 700$ K; employing this $n_{\text{opt},zT}$ in a homogeneous material would then lead to a reduction of the efficiency by 9%. For the same temperature interval, comparing $n_{\text{opt},zT_{\text{TAV}}}$ with that of $n_{\text{opt},\eta}$, the relative difference is about 5%, which translates, however, only to a relative difference in efficiency of about 0.2%, showing that zT_{TAV} is useful as a parameter for optimization for this material. This has been found previously for this and other materials, but only in the temperature range where the SPB model can be employed [131].

It can also be seen from Figure 6-1b that the $n_{\text{opt},zT}(T)$ varies quite a lot with T , providing us the opportunity to explore the potential of performance improvement by grading.

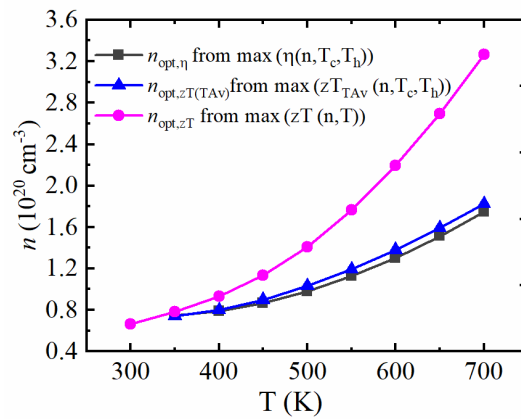


Figure 6-3: Optimum n according to different optimization parameters: $n_{\text{opt},zT}(T)$, $n_{\text{opt},\eta}(T_h = T, T_c)$ and $n_{\text{opt},zT_{\text{TAV}}}(T_h = T, T_c)$ (for $T_c = 300$ K).

1.1 Material grading

A graded material is formed from $n_{\text{opt},zT}(T)$ having the material properties corresponding to n_{opt} at that particular T as shown in Figure 6-3. The background lines correspond to the $n_{\text{opt},zT}$ for $T = 300$ K to 700 K (in 50 K intervals). The points of intersection of the red curve (graded)

and the background lines correspond to the $n_{\text{opt},zT}(T)$ at the respective T . For comparison, the material properties of a homogeneous material with $n = 1.75 \times 10^{20} \text{ cm}^{-3}$ (corresponding to $n_{\text{opt},\eta}$ for $T_h = 700 \text{ K}$ and $T_c = 300 \text{ K}$) is also shown (black curve with symbols). Figure 6-3d also shows a comparison of the spatially averaged zT , $zT_{\text{SpAv}} = \frac{1}{L} \int_0^L zT(x) dx$, for homogeneous and graded material. To obtain the spatial averages, the exact temperature profiles obtained from the shown material properties are used. As might be expected, the largest differences in zT are observed towards the lower and upper temperature limit and zT_{SpAv} is 9% larger for the graded material. Consequently, a gain in efficiency of 7.3% can be obtained by such a material grading over the highest efficiency possible from a non-graded material (Table 5).

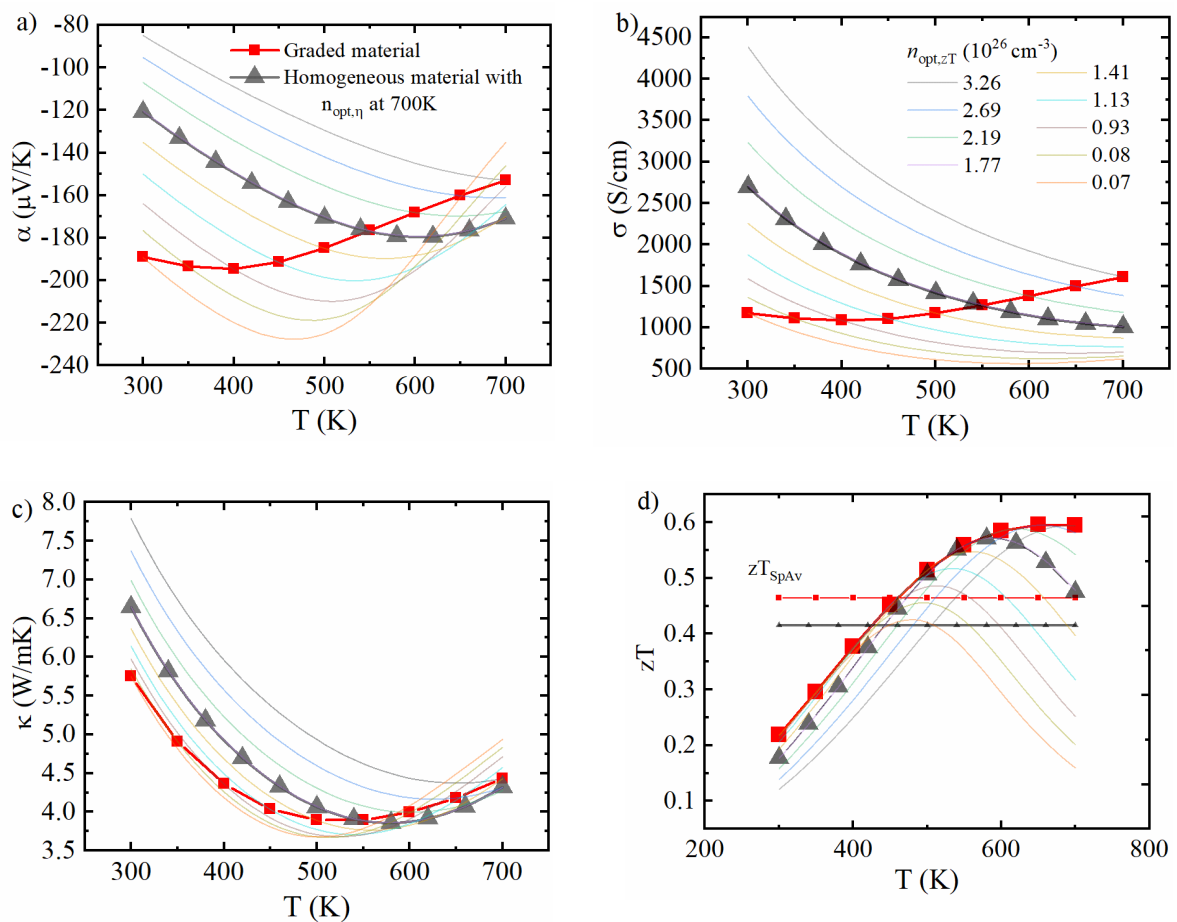


Figure 6-4: a) Seebeck coefficient; b) electrical conductivity; c) thermal conductivity and d) zT , for a graded material with $n_{\text{opt},zT}(T)$ and the homogenous material with the optimum constant n for the full T range based on efficiency. The material properties of the graded material are obtained at each T from the $n_{\text{opt},zT}$ at that T .

It was shown previously that a graded material with a maximized $zT(T)$ does not necessarily give the highest possible efficiency [99] due to the limited self-compatibility of materials, i.e., due to incompatible heat vs. current flow. A strict optimization of $n(x)$ with respect to efficiency can be done mathematically as shown e.g. in [28, 114, 118, 119]. Here, we analyze the impact of compatibility on the material with the grading as obtained from $n_{\text{opt},zT}(T)$ following the approach from Snyder and Ursell [101], explained in the introduction chapter (Section 1.5.1). For $T_c = 300$ K and $T_h = 700$ K, the reduced current density $u = \frac{j}{\kappa(T) \frac{dT}{dx}}$ is calculated as function of T . The current density j and $T(x)$ correspond to the maximum efficiency obtained for the graded material. In compatibility approach, the $u(T)$ is compared with the compatibility factor $s(T) = \frac{(-1+\sqrt{1+zT})}{\alpha T}$ [18]. If $u = s$ holds at any temperature, full self-compatibility of the leg is reached, i.e. the material contributes with its full potential to the efficiency of the device. Differing u and s correspond to a lower compatibility, limiting device efficiency. As shown in Figure 6-5a, u and s are not identical over the whole temperature range, but they are closer for the graded material compared to the homogenous material. We have calculated the reduced efficiency η_r , (for given hot and cold side temperature $\eta = \eta_r \eta_{\text{carnot}}$) given by eq. (38) [18, 112]. The η_r corresponding to u and s (maximum reduced efficiency) are shown in Figure 6-5b, showing almost perfect coincidence for the graded material. The integral average of the relative difference in reduced efficiency i.e., $\frac{1}{\Delta T} \int_{T_c}^{T_h} (|\eta_{r,u}| - |\eta_{r,s}|) / |\eta_{r,u}| dT$ is a qualitative indicator for how close the employed $n_{\text{opt},zT}(T)$ matches to the ideal (unknown) $n(x)$ giving maximum efficiency. This relative difference calculated with u and s is about 0.8% for the graded material indicating that the $n_{\text{opt}}(T)$ profile based on zT_{max} is very close, for this material and temperature conditions, to the maximum possible efficiency that can be obtained by $n(x)$ grading. For the homogeneous material, this difference amounts to about 2.9%, indicating that in addition to an increased overall zT in the graded material, the compatibility also improved. Considering a CPM TEG module made of materials with zT corresponding to graded and homogeneous TE leg, a gain in efficiency of 6.44 % is predicted. Therefore, overall gain in efficiency in graded leg is mainly due to the increase in the effective zT of the graded leg, but an additional 0.82% gain in efficiency is due to increased compatibility. Unlike previous studies on functional grading [28, 114, 118, 119] where compatibility criterion has not been considered for such grading studies,

our study shows that the chosen $n_{\text{opt},zT}(T)$ gives a close to maximum gain in efficiency based on self-compatibility for the considered material.

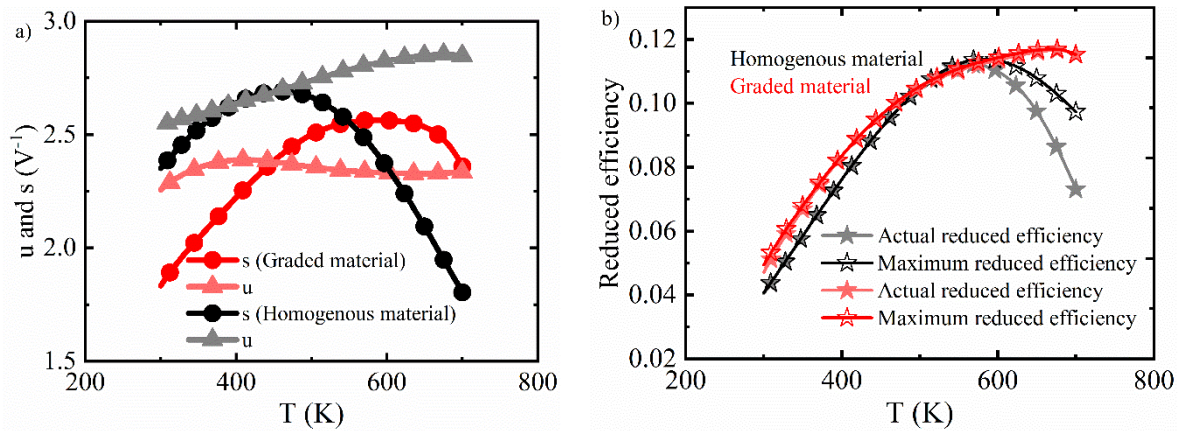


Figure 6-5: a) Variation of u and s with T for the graded and homogenous material. Maximum η_r is obtained locally when $u = s$. b) Actual η_r and maximum η_r for the graded and homogenous material. It can be seen that at higher temperatures, actual η_r is quite deviant from maximum η_r for homogenous material.

The combined material–device model derived in this thesis offers flexibility to check the effect of arbitrarily chosen $n(x)$ profiles on efficiency or power output. For example, the same study when performed with a linear grading following the equation $n = (-1.02985 \times 10^{26} + 5.64 \times 10^{23} \text{K}^{-1} * T(x)) \text{m}^{-3}$ (obtained using the endpoints with respect to temperature of $n_{\text{opt},zT}(T(x))$), results in a relative increase in efficiency of 5.3% compared to the homogeneous sample. Hence, if a material grading according to $zT_{\text{max},n}$ is not possible, a simple linear $n(T)$ grading can already give quite a gain in efficiency. Additionally, the possibility of segmentation can be easily explored as well with such a model. For a Mg_2Sn leg with segments for the temperature intervals 700 K – 500 K and 500 K – 300 K, the $n_{\text{opt},\eta}$ is found to be $n = 2.27 \times 10^{20} \text{cm}^{-3}$ and $0.98 \times 10^{20} \text{cm}^{-3}$ respectively. The material properties corresponding to such a segmented TE leg are shown in the Figure 6-6. As our model is based on the iterative integration method (Chapter 3) [133], it is straightforward to find the efficiency of such segmented leg. A gain in efficiency of 5.1% compared to the homogenous material is observed in such a TE leg which can be easily realized experimentally. The integral average of the relative difference in reduced efficiency $\frac{1}{\Delta T} \int_{T_c}^{T_h} (|\eta_{r,u}| - |\eta_{r,s}|) / |\eta_{r,u}| dT$ for the segmented leg amounts to be about 0.67% indicating higher compatibility compared to the locally graded

material based on zT . The graphs corresponding to u and s and the corresponding reduced efficiencies are given in Figure 6-6e and f.

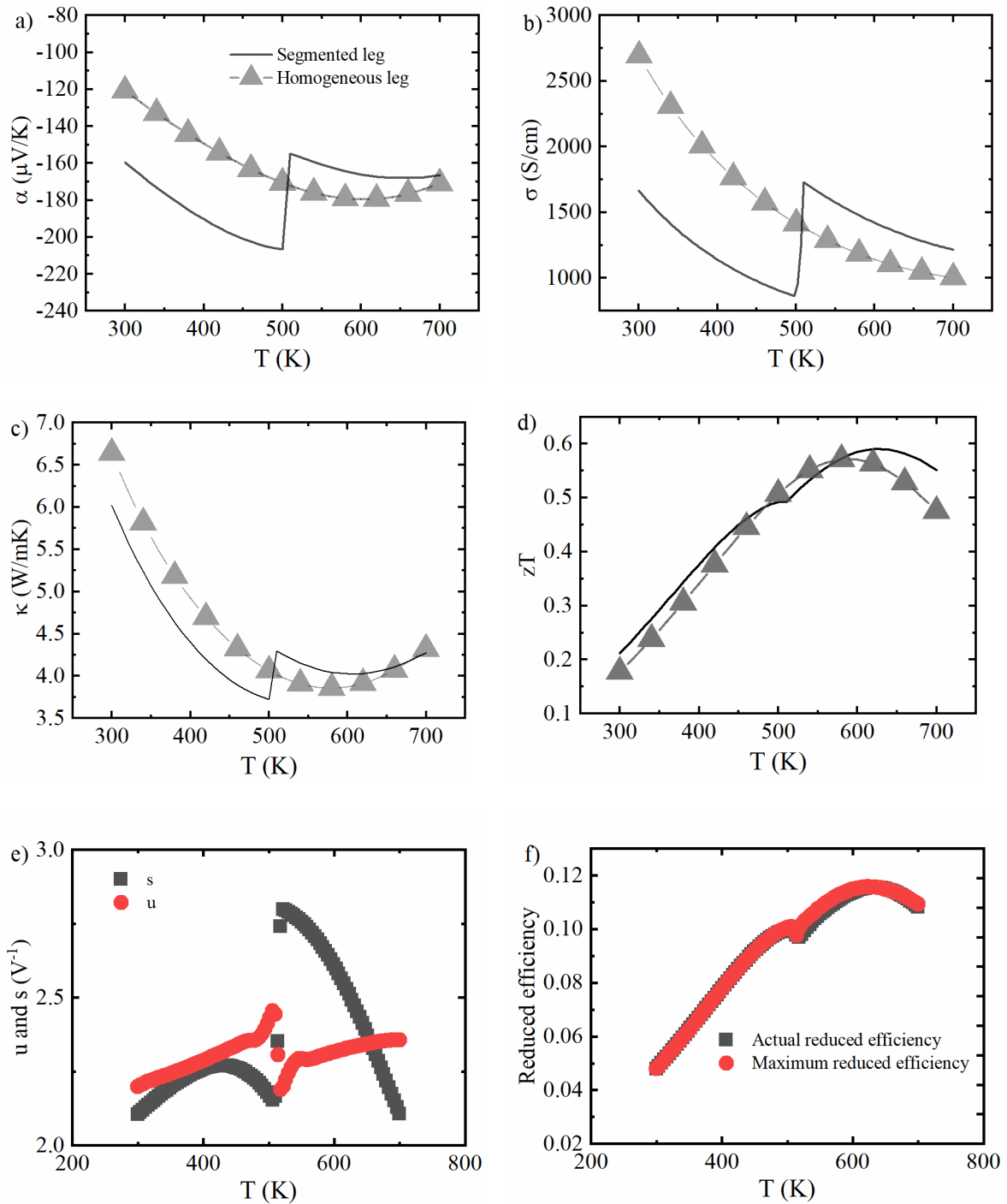


Figure 6-6: Material properties of segmented Mg_2Sn leg a) Seebeck coefficient b) Electrical conductivity c) Thermal conductivity d) zT . For the segment 700 K-500 K $n = 2.27 \times 10^{20} \text{ cm}^{-3}$ and for the second segment 500 K-300 K $n = 9.87 \times 10^{19} \text{ cm}^{-3}$, e) u and s e) Actual η_r and maximum η_r .

Table 5 summarizes the gain in efficiency of grading based on $n_{\text{opt},zT}(T)$, linear grading and two segmented leg, over the homogeneous leg.

Table 5: Efficiency and relative gain for differently graded legs for $T_c=300$ K and $T_h=700$ K.

	Homogeneous leg	Graded ($n_{\text{opt},zT}(T)$)	Linear grading $n = (-1.02985 * 10^{26} + 5.64 * 10^{23} \text{ K}^{-1} * T(x)) \text{ m}^{-3}$	Two segmented leg with $n_1 = 2.27 * 10^{20} \text{ cm}^{-3}$ and $n_2 = 0.98 * 10^{20} \text{ cm}^{-3}$
$\eta_{\text{max}} (\%)$	6.85	7.35	7.21	7.20
Relative gain in efficiency	-	7.3	5.3	5.1

In summary, the advantages of using a simple and efficient combined material-device tool in optimizing performance has been discussed using n-type Mg_2Sn as an example. Using a two band model the thermoelectric transport properties can be described over the full application temperature range and the effect of a locally varying $n(x)$ profile on the predicted conversion efficiency can easily be studied. Assuming a linear $T(x)$ and adjusting $n(x)$ such that zT is maximized at each position x , a gain in efficiency of 7.3% can be achieved in n-type Mg_2Sn , compared to the best homogeneous material with constant n . We furthermore show that an increase of about 5% can be achieved by using a simple linear $n(x)$ or by using a leg with two segments, which would be practically much easier to fabricate than a linearly graded or even non-linear $n(x)$. We not only show possibilities to obtain gain in efficiency by material grading or segmentation but also consider the obtained results based on compatibility criterion. For Mg_2Sn , we find that grading according to the local zT also improves the self-compatibility of the material, increasing efficiency beyond the gain of the average zT . As the general temperature dependencies and interrelations between α, σ, κ are similar within the whole $\text{Mg}_2(\text{Si},\text{Sn})$ family it is plausible that the suggested approach is fruitful for that material class. Therefore, materials with such drastic variation in optimum n vs T as well as materials with highly bent temperature profiles such as PbTe [135] are potential candidates to check for any improvement in performance through grading. According to Chapter 5 (Figure 5-5), grading or segmentation with $\text{Mg}_2\text{Si}_{1-x}\text{Sn}_x$ would not yield much gain as the variation of n_{opt} vs T is much less compared to the one shown here. However, the comparability is limited as only an SPB

model was employed there. If an accurate two band model is employed like in chapter 6, it is likely that gain in efficiency through grading is possible. Similar studies on other material systems can give a hint of the achievable gain in efficiency through such simple engineering.

Supporting Information:

In the discussion above, we have restricted ourselves order to linear temperature variation for grading to reduce computation time. In order to further prove the feasibility of this simplification, an iteration of $T(x)$ was done and the optimum n and the subsequent temperature profile are shown as overlaps to Figure 6-3 and Figure 6-1 in Figure 6-7. There is no significant change in the gain in efficiency nor the compatibility in the iteratively graded material as can be seen, with a very slight change in optimum n at the low temperature side (350 K to 450 K in Figure 6-7a) of the TE leg where the temperature profile is slightly bent. This amounts to 0.01% change in efficiency between the iterated and non-iterated graded material and hence negligible.

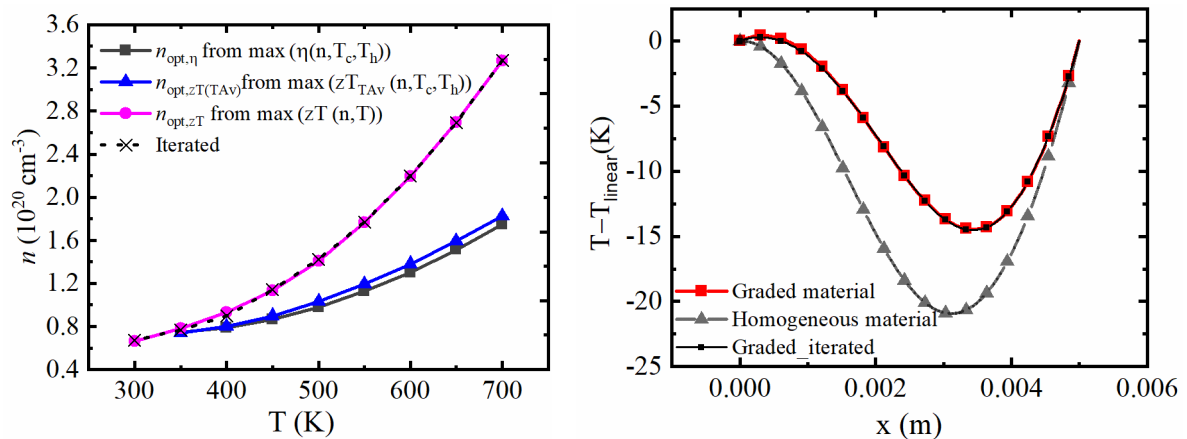


Figure 6-7: a) $n_{\text{opt},zT}(T(x))$ where $T(x)$ is the temperature profile of the graded material (red curve in b)Figure 6-7) formed assuming a linear $T(x)$. The temperature profile of the graded material obtained after setting the $n_{\text{opt},zT}(T(x))$ according to the red curve. The red and black curves (with square symbols) coincide as can be seen.

7 Conclusion and outlook

Beginning with the problems involved in CPM, this thesis not only highlights the importance of using fully temperature dependent calculation on the module level, but also provides a complete tool connecting module to materials, highlighting the importance of efficiency as a parameter for material optimization instead of using the local material parameter zT . In the process, a faster and simpler tool for performance calculation has been created.

In Chapter 3, it was explained that a combination of temperature average for Seebeck coefficient and spatial averages for thermal and electrical resistivities are physically appropriate averages as these represent the Seebeck voltage, electrical resistance and thermal conductance of the leg correctly. In order to obtain the exact temperature profile needed to calculate spatial averages, an iterative procedure for obtaining the T profile was developed and employed. With such a procedure it is also possible to determine the separate individual contributions to the bending of the T profile. The importance of the influence of the temperature dependence of $\kappa(T)$ on the bending of the T profile is shown and unless spatial averages are employed, the effective material properties for electrical and thermal resistivities would not be physically appropriate. Therefore, the temperature averages which are commonly used with CPM calculations can fail significantly in performance prediction for materials with strong $\kappa(T)$ dependence. The error in CPM remaining even when the physically appropriate averages are used was identified to be due to the asymmetry in the local distribution of the Joule heat and the incomplete compensation of the neglect of Thomson heat by the estimate of inflowing Peltier heat in CPM, and it is shown and discussed that the absence of Thomson heat in CPM does not affect the power prediction.

The neglected Thomson heat is mainly compensated by a simultaneously different estimate of Peltier heat in CPM, as α_h (and α_c) assumed in CPM are considerably different from the real ones, due to the assumption of a constant α . This covers the main fraction of the neglect of Thomson heat, even, depending on the characteristics of the T dependence of α , it might be an over- or under-compensation. The uncompensated Thomson heat not only affects the calculation of Q_h but also the optimum current for efficiency in CPM. The remaining, non-compensated part can be easily estimated based on the entropy flow diagram.

Illustrated by an entropy flow diagram of a TE leg, it is shown that a portion of Thomson heat appearing in a real device but neglected by the CPM assumption of a constant Seebeck coefficient always remains uncompensated at the hot side in CPM and a correction using the $\alpha(T)$ diagram is suggested. Such a correction is simple due to the essential finding that the crossing of the temperature-averaged Seebeck coefficient with that of the Seebeck curve physically represents the zero point of Thomson heat reflowing within the TE leg. The remaining minor error in CPM is due to the asymmetry in heat distribution.

With this work we have identified the best averaging mode for CPM and provided a correction for one of the major sources of remaining error, providing a way to use CPM with higher accuracy than before. The fact that we still need the T -dependent calculation to do so, limits the practical usability, but does not nullify the argument.

Based on the CPM efficiency expression, zT is usually considered as the main indicator of performance of the material and is therefore almost generally used as a parameter for optimising material specific parameters such as the carrier concentration. Such an optimization does not consider the fact that the TE leg operates over a temperature range and hence optimizing zT for a specific temperature can be misleading. On the contrary, usually, maximum zT values of materials are ranked. Therefore, a combined material-device model was devised here to signify the importance of using leg efficiency directly as a measure for optimizing n . Using an SPB approach for modelling the properties of p-Mg₂Si_{1-x}Sn_x as an example, the differences in optimum n obtained using zT_{\max} or zT_{TAV} vs the optimum n obtained considering the efficiency was shown. It was concluded that zT_{TAV} can be used practically with good accuracy to find optimum carrier concentration and composition even though the predicted efficiency with zT_{TAV} can be, in principle, different from reality. Using zT_{\max} as a parameter for optimizing n at 600 K leads to an error as high as 20% in n_{opt} for p-Mg₂Si_{1-x}Sn_x compared to using efficiency as a parameter for the temperature range of operation 600 K – 300 K.

Practically, hot side temperatures involving bipolar conduction are necessary to reach highest efficiency. Hence, transport models beyond a single band model are required to describe TE properties. Using a two-band model for describing the properties of n-type Mg₂Sn as an example, the advantages of using the combined material-device tool in grading and segmentation studies was demonstrated. Adjusting $n(x)$ such that zT is maximized at each position x , a 7 % gain in efficiency can be obtained in n-type Mg₂Sn, compared to the best homogeneous material with a constant n (optimized for maximum efficiency). Additionally,

the compatibility criterion was checked and it was found that this grading results in an efficiency very close to the maximum possible efficiency. Such a grading improved the overall zT in addition to improving the self-compatibility of the material. Studies on other material systems with such a combined model can not only provide insights into the achievable gain in efficiency through such engineering approaches but can give direct correlation of device performance based on fundamental material parameters.

Additionally, the integrated performance analysis tool provides flexibility to study the effect of fundamental material parameters such as effective mass, valley degeneracy, scattering mechanisms, deformation potentials and many others, directly on TEG performance, which can be quite useful in TE material development. This tool can further be developed to incorporate the effect of contact resistances, providing realistic estimates on accurate gains in TEG performance through grading and segmentation.

Quantification of asymmetry in heat distribution

In Chapter 4 (Paper 2), it was mentioned that, besides the change of the Peltier-Thomson heat balance due to the CPM assumption, the asymmetry in heat distribution (local asymmetry in release of Joule heat and local asymmetry in the outflow of inner heat due to asymmetric distribution of thermal conductivity along the leg) leads to the remaining differences between CPM and exact calculations. It would be recommended to quantify this by studying the slope of the $\alpha(T)$, $\sigma(T)$ and $\kappa(T)$ curves and be able to correct for this asymmetry in CPM using analytical expressions. This can be done by performing a study using generally observed slopes of TE material properties and quantifying the asymmetry based on the slopes.

Given the importance of temperature dependence of material properties in altering the heat generation and distribution, it would be interesting to see if a gain in efficiency could be obtained by adjusting the temperature dependence of material properties and thereby altering the heat flow within the leg, to reduce or relocate resistive losses and improve efficiency. For example, a falling $\alpha(T)$ curve takes away Thomson heat from the hot side, contributing to increased efficiency compared to an equivalent material with rising $\alpha(T)$. It would also be interesting to study what type of curvature of the three main TE properties is optimum for best efficiency and power output. Similar studies have been done previously in simpler forms [136, 137] and can be quite useful especially for designing graded and segmented modules.

Effect of 3D current and heat flow

While the focus of the thesis was to find faster and accurate ways to perform TEG performance calculations, it has to be kept in mind that the developed tools are all based on the assumption that the transport is homogeneous with respect to the leg cross section, reducing the geometry of the problem to 1D, disregarding e.g. the potential impact of radiative and convective losses from the leg's envelope surface that might be relevant in realistic application scenarios. These can be modelled using appropriate mathematical description and it would be interesting to see the effects in comparison to the 1D assumption. In an approximate approach, the convective and radiative exchange terms can be added to the 1D model described in Chapter 3 and the iterative solution can be expanded accordingly. Previously similar attempts have been made on 1D models [74, 138] and have proved useful. Such a quasi-1D model can be an improvement over the simple 1D model implemented in the course of this thesis. It could be validated against 3D FEM simulations with not just a single leg but a unicouple to make the model more realistic also geometrically, as this will involve that the current in- and outflow into the leg is not symmetric due to the typical pi-shape of a thermocouple. Based on this study correction factors could be derived to be added to the 1D model so that the simplicity is maintained yet the output is more realistic. Further, the effect of module filling factors (the way the pn couple is packed in a TEG), area ratio between p-type and n-type legs and of non-ideal metal contacts need to be incorporated.

Additionally, when the effect of metal contacts is included, more geometrical effects as mentioned previously such as current constriction in a p/n-couple can become important. Hence, a comparative study using 2D or 3D FEM simulation for an actual p/n-couple is recommended.

Effect of scattering mechanisms on temperature dependence and therefore on heat flow

Since scattering mechanisms of charge carriers and phonons are what alters the temperature dependence of the TE properties mainly in addition to intrinsic carrier effects, with the combined material-device tool it would be interesting to see how scattering mechanism can be tuned to obtain a gain in efficiency if possible. From such a study, it could also be possible then to obtain the convenient scattering mechanism for a material class and tune it accordingly.

Further, it would be recommended to study different types of grading such as by tuning the composition, or using a criterion other than zT_{\max} as used in Chapter 6. In Chapter 6, it was found that there was an increase in compatibility in addition to improving overall zT by grading. While this might be a coincidence for this material case, it would be useful to study the correlation between increase in zT vs variation in compatibility while grading.

Generally, with the combined material-device model, the effect of several material parameters on device performance can be studied in a direct and easily operable tool.

8 References

This section contains references for Chapters 1, 6, 7.

1. de Winter, F., G. Stapfer, and E. Medina, *The design of a nuclear power supply with a 50 year life expectancy: the JPL Voyager's SiGe MHW RTG*. 1999, SAE Technical Paper.
2. Kelly, C., *MHW RTG performance during LES 8/9 and voyager missions*. Space Nuclear Power Systems, 1987: p. 197-200.
3. Boston, M.D. *Simplistic propulsion analysis of a breakthrough space drive for Voyager*. in *AIP Conference Proceedings*. 2000. American Institute of Physics.
4. Solutions, R. and A.N. Cafe, *Research & Applications*. Consultant, 2021. **12**: p. 00PM.
5. Maki, J., et al., *The Mars 2020 Engineering Cameras and microphone on the perseverance rover: A next-generation imaging system for Mars exploration*. Space Science Reviews, 2020. **216**(8): p. 1-48.
6. Bennett, G., et al. *Mission of daring: the general-purpose heat source radioisotope thermoelectric generator*. in *4th international energy conversion engineering conference and exhibit (IECEC)*. 2006.
7. Looney, B., *Statistical Review of World Energy, 2020*. J Bp, 2020. **69**: p. 66.
8. Ma, Z., et al., *Review of experimental approaches for improving zT of thermoelectric materials*. Materials Science in Semiconductor Processing, 2021. **121**: p. 105303.
9. Hasan, M.N., et al., *Inorganic thermoelectric materials: A review*. International Journal of Energy Research, 2020. **44**(8): p. 6170-6222.
10. Gayner, C. and K.K. Kar, *Recent advances in thermoelectric materials*. J Progress in Materials Science, 2016. **83**: p. 330-382.
11. Newell, R.G. and D. Raimi, *Global energy outlook comparison methods: 2020 update*. 2020, Resources for the Future.

12. Zhang, X. and L.-D. Zhao, *Thermoelectric materials: Energy conversion between heat and electricity*. Journal of Materiomics, 2015. **1**(2): p. 92-105.
13. Shakouri, A., *Recent developments in semiconductor thermoelectric physics and materials*. Annual review of materials research, 2011. **41**: p. 399-431.
14. Bell, L.E., *Cooling, heating, generating power, and recovering waste heat with thermoelectric systems*. J Science, 2008. **321**(5895): p. 1457-1461.
15. LeBlanc, S., *Thermoelectric generators: linking material properties and systems engineering for waste heat recovery applications*. Sustainable Materials and Technologies, 2014. **1**: p. 26-35.
16. Rowe, D.M., *CRC handbook of thermoelectrics*. 1995: CRC press.
17. Rowe, D.M., *Thermoelectrics and its Energy Harvesting, 2-Volume Set*. 2018: CRC press.
18. Rowe, D.M., *Thermoelectrics handbook: macro to nano*. 2005, CRC press.
19. Stachowiak, H., et al., *A thermoelectric sensor for fluid flow measurement. principles, calibration and solution for self temperature compensation*. Flow Measurement and Instrumentation, 1998. **9**(3): p. 135-141.
20. Romdhane, M., C. Gourdon, and G. Casamatta, *Development of a thermoelectric sensor for ultrasonic intensity measurement*. Ultrasonics, 1995. **33**(2): p. 139-146.
21. Fleurial, J., et al. *Thermoelectrics: From space power systems to terrestrial waste heat recovery applications*. in *Proceedings of the Thermoelectrics Applications Workshop, San Diego, CA, USA*. 2011.
22. Yang, J. and T. Caillat, *Thermoelectric materials for space and automotive power generation*. MRS bulletin, 2006. **31**(03): p. 224-229.
23. Mueller, E., et al., *Functionally graded materials for sensor and energy applications*. Materials Science Engineering: A, 2003. **362**(1-2): p. 17-39.
24. Harman, T.C. and J.M. Honig, *Thermoelectric and thermomagnetic effects and applications*. 1967.
25. Snyder, G.J. and E.S. Toberer, *Complex thermoelectric materials*. Nature materials, 2008. **7**(2): p. 105-114.
26. Seebeck, T., *Magnetic polarization of metals and minerals*. Abhandlungen der Deutschen Akademie der Wissenschaften zu Berlin, 1822. **265**: p. 1823.
27. Ioffe, A.F., et al., *Semiconductor thermoelements and thermoelectric cooling*. PhT, 1959. **12**(5): p. 42.
28. Goupil, C., *Continuum theory and modeling of thermoelectric elements*. 2015: John Wiley & Sons.
29. Koolatran. *Koolatron*. [cited 2016 03 June]; Available from: <https://www.koolatron.com/us/en>.
30. Bojić, M., et al., *Thermoelectric cooling of a train carriage by using a coldness-recovery device*. Energy, 1997. **22**(5): p. 493-500.
31. Brown, W.K. and S.W. Rabb, *Refrigerator-package arrangement*. 1966, Google Patents.

32. Min, G. and D. Rowe, *Cooling performance of integrated thermoelectric microcooler*. Solid-State Electronics, 1999. **43**(5): p. 923-929.
33. Boehmer, A.P. and B.M. Jaremus, *Thermoelectric refrigerator*. 1965, Google Patents.
34. Zhao, D. and G. Tan, *A review of thermoelectric cooling: materials, modeling and applications*. Applied thermal engineering, 2014. **66**(1-2): p. 15-24.
35. Elarusi, A., A. Attar, and H. Lee, *Optimal design of a thermoelectric cooling/heating system for car seat climate control (CSCC)*. J Journal of Electronic Materials, 2017. **46**(4): p. 1984-1995.
36. Lundstrom, M.S. and C. Jeong, *Near-equilibrium transport: fundamentals and applications*. Vol. 2. 2012: World Scientific Publishing Company.
37. Heikes, R. and R. Ure, *Thermoelectricity: science and engineering*. 1961. Interscience Publishers.
38. Zabrocki, K., et al., *Continuum Theory of TE Elements*. Continuum Theory and Modeling of Thermoelectric Elements, 2015.
39. Apertet, Y. and C. Goupil, *On the fundamental aspect of the first Kelvin's relation in thermoelectricity*. International Journal of Thermal Sciences, 2016. **104**: p. 225-227.
40. Lee, H., *The Thomson effect and the ideal equation on thermoelectric coolers*. Energy, 2013. **56**: p. 61-69.
41. Sandoz-Rosado, E.J., *Investigation and development of advanced models of thermoelectric generators for power generation applications*. 2009: Rochester Institute of Technology.
42. Domenicali, C.A., *Irreversible thermodynamics of thermoelectric effects in inhomogeneous, anisotropic media*. J Physical Review, 1953. **92**(4): p. 877.
43. Antonova, E.E. and D.C. Looman. *Finite elements for thermoelectric device analysis in ANSYS*. in *Thermoelectrics, 2005. ICT 2005. 24th International Conference on*. 2005. IEEE.
44. Kim, C.N., *Development of a numerical method for the performance analysis of thermoelectric generators with thermal and electric contact resistance*. Applied Thermal Engineering, 2018. **130**: p. 408-417.
45. Hogan, T. and T. Shih, *Modeling and characterization of power generation modules based on bulk materials*. Thermoelectrics Handbook: Macro to Nano, 2006: p. 12.1-12.23.
46. Oliveira, K.S., R.P. Cardoso, and C.J. Hermes, *Two-Dimensional Modeling of Thermoelectric Cells*. 2014.
47. Sherman, B., R. Heikes, and R. Ure Jr, *Calculation of efficiency of thermoelectric devices*. Journal of Applied Physics, 1960. **31**(1): p. 1-16.
48. Brandt, J.A., *Solutions to the differential equations describing the temperature distribution, thermal efficiency, and power output of a thermoelectric element with variable properties and cross sectional area*. Advanced Energy Conversion, 1962. **2**: p. 219-230.

49. Courant, R. and a. mathematics, *Variational methods for the solution of problems of equilibrium and vibrations*. J Lecture notes in pure, 1994: p. 1-1.
50. Zlámal, M., *On the finite element method*. Numerische Mathematik, 1968. **12**(5): p. 394-409.
51. Zienkiewicz, O.C., K. Morgan, and K. Morgan, *Finite elements and approximation*. 2006: Courier Corporation.
52. Lau, P.G. and R.J. Buist. *Calculation of thermoelectric power generation performance using finite element analysis*. in *XVI ICT'97. Proceedings ICT'97. 16th International Conference on Thermoelectrics (Cat. No. 97TH8291)*. 1997. IEEE.
53. Strutynsky, M., *Computer technologies in thermoelectricity*. Journal of Thermoelectricity, 2009(4): p. 29-44.
54. Zeier, W.G., et al., *Engineering half-Heusler thermoelectric materials using Zintl chemistry*. Nature Reviews Materials, 2016. **1**(6): p. 1-10.
55. He, H., et al., *Comprehensive modeling for geometric optimization of a thermoelectric generator module*. Energy conversion and management, 2019. **183**: p. 645-659.
56. Omer, S. and D. Infield, *Design optimization of thermoelectric devices for solar power generation*. Solar Energy Materials and Solar Cells, 1998. **53**(1-2): p. 67-82.
57. Wang, J., et al., *An optimization study of structural size of parameterized thermoelectric generator module on performance*. Energy Conversion and Management, 2018. **160**: p. 176-181.
58. Bitschi, A., *Modelling of thermoelectric devices for electric power generation*. 2009, Diss., Eidgenössische Technische Hochschule ETH Zürich, Nr. 18441, 2009.
59. Decher, R., *Direct Energy Conversion: fundamentals of electric power production*. 1997: Oxford University Press on Demand.
60. Lee, H., et al., *Modeling and analysis of the effect of thermal losses on thermoelectric generator performance using effective properties*. Applied Energy, 2018. **211**: p. 987-996.
61. Kim, H.S., et al., *Relationship between thermoelectric figure of merit and energy conversion efficiency*. Proceedings of the National Academy of Sciences, 2015. **112**(27): p. 8205-8210.
62. Tuley, R. and K. Simpson, *ZT Optimization: An Application Focus*. Materials, 2017. **10**(3): p. 309.
63. Armstrong, H., et al., *Estimating Energy Conversion Efficiency of Thermoelectric Materials: Constant Property Versus Average Property Models*. Journal of Electronic Materials, 2017. **46**(1): p. 6-13.
64. Lau, P.G. and R.J. Buist. *Calculation of thermoelectric power generation performance using finite element analysis*. in *Thermoelectrics, 1997. Proceedings ICT'97. XVI International Conference on*. 1997. IEEE.
65. Mahan, G., *Inhomogeneous thermoelectrics*. Journal of Applied Physics, 1991. **70**(8): p. 4551-4554.

66. Fraisse, G., et al., *Comparison of different modeling approaches for thermoelectric elements*. Energy conversion and management, 2013. **65**: p. 351-356.
67. Chen, J., Z. Yan, and L. Wu, *The influence of Thomson effect on the maximum power output and maximum efficiency of a thermoelectric generator*. Journal of Applied Physics, 1996. **79**(11): p. 8823-8828.
68. Huang, M.-J., R.-H. Yen, and A.-B. Wang, *The influence of the Thomson effect on the performance of a thermoelectric cooler*. International Journal of Heat and Mass Transfer, 2005. **48**(2): p. 413-418.
69. Sandoz-Rosado, E.J., S.J. Weinstein, and R.J. Stevens, *On the Thomson effect in thermoelectric power devices*. International Journal of Thermal Sciences, 2013. **66**: p. 1-7.
70. Bjørk, R., et al., *Analysis of the internal heat losses in a thermoelectric generator*. J International Journal of Thermal Sciences, 2014. **85**: p. 12-20.
71. Ziolkowski, P., et al., *Estimation of thermoelectric generator performance by finite element modeling*. Journal of electronic materials, 2010. **39**(9): p. 1934-1943.
72. Min, G. and D.J.J.o.p.S. Rowe, *Optimisation of thermoelectric module geometry for 'waste heat' electric power generation*. 1992. **38**(3): p. 253-259.
73. Slack, G.A. and D. Rowe, *CRC handbook of thermoelectrics*. 1995, CRC press Boca Raton, FL.
74. Rowe, D., G. Min, and Technology, *Design theory of thermoelectric modules for electrical power generation*. IEE Proceedings-Science, Measurement, 1996. **143**(6): p. 351-356.
75. Goldsmid, H.J., *Bismuth Telluride and Its Alloys as Materials for Thermoelectric Generation*. Materials (Basel), 2014. **7**(4): p. 2577-2592.
76. Chen, Z.G., et al., *High-performance SnSe thermoelectric materials: Progress and future challenge*. Progress in Materials Science, 2018. **97**: p. 283-346.
77. de Boor, J., T. Dasgupta, and E. Müller, *Thermoelectric properties of magnesium silicide based solid solutions and higher manganese silicides*. 2016: CRC Press, Taylor & Francis Group Boca Raton, NW, USA.
78. Hu, C., et al., *Transport mechanisms and property optimization of p-type (Zr, Hf) CoSb half-Heusler thermoelectric materials*. Materials Today Physics, 2018. **7**: p. 69-76.
79. Rogl, G. and P. Rogl, *Skutterudites, a most promising group of thermoelectric materials*. Current Opinion in Green and Sustainable Chemistry, 2017. **4**: p. 50-57.
80. Mao, J., et al., *Defect Engineering for Realizing High Thermoelectric Performance in n-Type Mg₃Sb₂-Based Materials*. ACS Energy Letters, 2017. **2**(10): p. 2245-2250.
81. Wang, Y., et al., *Optimizing the thermoelectric performance of p-type Mg₃Sb₂ by Sn doping*. Vacuum, 2020. **177**: p. 109388.
82. Pei, Y., et al., *Convergence of electronic bands for high performance bulk thermoelectrics*. Nature, 2011. **473**(7345): p. 66-9.

83. May, A.F. and G.J. Snyder, *Introduction to modeling thermoelectric transport at high temperatures*. Materials, preparation, characterization in thermoelectrics, 2012: p. 1-18.
84. Naithani, H. and T. Dasgupta, *Critical Analysis of Single Band Modeling of Thermoelectric Materials*. ACS Applied Energy Materials, 2019. **3**(3): p. 2200-2213.
85. Pei, Y., et al., *Low effective mass leading to high thermoelectric performance*. Energy & Environmental Science, 2012. **5**(7): p. 7963-7969.
86. Kim, H.S., W.S. Liu, and Z.F. Ren, *The bridge between the materials and devices of thermoelectric power generators*. Energy & Environmental Science, 2017. **10**(1): p. 69-85.
87. Ryu, B., J. Chung, and S. Park, *Thermoelectric efficiency has three Degrees of Freedom*. J arXiv preprint arXiv:11148, 2018.
88. Fistul, V.I., *Heavily doped semiconductors*. Vol. 1. 2012: Springer Science & Business Media.
89. Grundmann, M., *Physics of semiconductors*. Vol. 11. 2010: Springer.
90. Liu, W., et al., *Advanced thermoelectrics governed by a single parabolic band: Mg₂Si_{0.3}Sn_{0.7}, a canonical example*. Physical Chemistry Chemical Physics, 2014. **16**(15): p. 6893-6897.
91. Tobola, J., S. Kaprzyk, and H. Scherrer, *Mg-Vacancy-Induced Semiconducting Properties in Mg₂Si_{1-x}Sb_x from Electronic Structure Calculations*. Journal of electronic materials, 2010. **39**(9): p. 2064-2069.
92. Rowe, D.M., *Materials, preparation, and characterization in thermoelectrics*. 2017: CRC press.
93. Ashcroft, N.W. and N.D. Mermin, *Solid state physics*. 1976, holt, rinehart and winston, new york London.
94. Kamila, H., et al., *Analyzing transport properties of p-type Mg₂Si–Mg₂Sn solid solutions: optimization of thermoelectric performance and insight into the electronic band structure*. Journal of Materials Chemistry A, 2019. **7**(3): p. 1045-1054.
95. Sankhla, A., et al., *Analyzing thermoelectric transport in n-type Mg₂Si_{0.4}Sn_{0.6} and correlation with microstructural effects: An insight on the role of Mg*. Acta Materialia, 2020. **199**: p. 85-95.
96. Koizumi, M., *The concept of FGM*. Ceramic transactions, 1993. **34**: p. 3-10.
97. Pham, H.N., *Design and Optimization of Effective Segmented Thermoelectric Generator for Waste Heat Recovery*. 2015.
98. Sherman, B., R. Heikes, and R. Ure Jr, *Calculation of efficiency of thermoelectric devices*. J Journal of Applied Physics, 1960. **31**(1): p. 1-16.
99. Snyder, G.J. and T.S. Ursell, *Thermoelectric efficiency and compatibility*. Phys Rev Lett, 2003. **91**(14): p. 148301.
100. Snyder, G.J., *Application of the compatibility factor to the design of segmented and cascaded thermoelectric generators*. Applied physics letters, 2004. **84**(13): p. 2436-2438.

101. Ursell, T. and G. Snyder. *Compatibility of segmented thermoelectric generators*. in *Twenty-First International Conference on Thermoelectrics, 2002. Proceedings ICT'02*. 2002. IEEE.
102. Li, A., et al., *High-Performance Mg₃Sb₂-xBi_x Thermoelectrics: Progress and Perspective*. 2020. **2020**.
103. Toberer, E.S., A.F. May, and G.J. Snyder, *Zintl chemistry for designing high efficiency thermoelectric materials*. *J Chemistry of Materials*, 2010. **22**(3): p. 624-634.
104. Pei, Y., H. Wang, and G.J.J.A.m. Snyder, *Band engineering of thermoelectric materials*. 2012. **24**(46): p. 6125-6135.
105. Foster, S. and N. Neophytou, *Doping optimization for the power factor of bipolar thermoelectric materials*. *Journal of Electronic Materials*, 2019. **48**(4): p. 1889-1895.
106. Qin, F., et al., *Crystal Structure and Atomic Vacancy Optimized Thermoelectric Properties in Gadolinium Selenides*. 2020. **32**(23): p. 10130-10139.
107. Kang, S.D. and G.J. Snyder, *Transport property analysis method for thermoelectric materials: material quality factor and the effective mass model*. arXiv preprint arXiv:.06896, 2017.
108. McKinney, R.W., et al., *Search for new thermoelectric materials with low Lorenz number*. 2017. **5**(33): p. 17302-17311.
109. Kumar, A., et al., *A Review on Fundamentals, Design and Optimization to High ZT of Thermoelectric Materials for Application to Thermoelectric Technology*. 2021: p. 1-23.
110. Mueller, E., et al., *Functionally graded materials for sensor and energy applications*. 2003. **362**(1-2): p. 17-39.
111. Shiota, I. and Y. Miyamoto, *Functionally graded materials 1996*. 1997: Elsevier.
112. Ioffe, A.F., et al., *Semiconductor thermoelements and thermoelectric cooling*. 1959. **12**(5): p. 42.
113. Cramer, C.L., H. Wang, and K.J.J.o.E.M. Ma, *Performance of functionally graded thermoelectric materials and devices: A review*. 2018. **47**(9): p. 5122-5132.
114. Anatyshuk, L. and L. Vikhor, *Computer design of thermoelectric functionally graded materials*, in *Functionally Graded Materials 1996*. 1997, Elsevier. p. 501-507.
115. Teraki, J. and T. Hirano, *A design procedure of functionally graded thermoelectric materials*, in *Functionally Graded Materials 1996*. 1997, Elsevier. p. 483-488.
116. Edry, I., et al. *Calculation of Temperature Profile and Power Performance of Thermoelectric Energy Materials*. in *2 nd European Conference on Thermoelectrics, Poland*. 2004.
117. Anatyshuk, L. and L. Vikhor. *Physics and methods of FGTM design*. in *Proceedings ICT'03. 22nd International Conference on Thermoelectrics (IEEE Cat. No. 03TH8726)*. 2003. IEEE.
118. Kaliazin, A., V. Kuznetsov, and D. Rowe. *Rigorous calculations related to functionally graded and segmented thermoelements*. in *Proceedings ICT2001. 20 International Conference on Thermoelectrics (Cat. No. 01TH8589)*. 2001. IEEE.

119. Hirano, T., J. Teraki, and Y. Nishio. *Computational design for functionally graded thermoelectric materials*. in *Materials science forum*. 1999. Trans Tech Publ.
120. Anatyshuk, L. and L. Vikhor. *Functionally graded materials and new prospects for thermoelectricity use*. in *XVI ICT'97. Proceedings ICT'97. 16th International Conference on Thermoelectrics (Cat. No. 97TH8291)*. 1997. IEEE.
121. Guélou, G., et al., *Issues and opportunities from Peltier effect in functionally-graded colusites: From SPS temperature modeling to enhanced thermoelectric performances*. 2021. **22**: p. 100948.
122. Ma, T., et al., *Continuously graded doped semiconducting polymers enhance thermoelectric cooling*. 2021. **119**(1): p. 013902.
123. Yang, S.E., et al., *Composition-segmented BiSbTe thermoelectric generator fabricated by multimaterial 3D printing*. 2021. **81**: p. 105638.
124. Snyder, G.J.J.A.p.l., *Application of the compatibility factor to the design of segmented and cascaded thermoelectric generators*. 2004. **84**(13): p. 2436-2438.
125. Zaitsev, V., et al., *Highly effective Mg₂Si_{1-x}Sn_x thermoelectrics*. 2006. **74**(4): p. 045207.
126. Liu, W., et al., *Convergence of conduction bands as a means of enhancing thermoelectric performance of n-type Mg₂Si_{1-x}Sn_x solid solutions*. 2012. **108**(16): p. 166601.
127. Sankhla, A., et al., *Experimental investigation of the predicted band structure modification of Mg₂X (X: Si, Sn) thermoelectric materials due to scandium addition*. 2019. **125**(22): p. 225103.
128. Zhu, Y., et al., *Thermodynamic criteria of the thermoelectric performance enhancement in Mg₂Sn through the self-compensation vacancy*. *Materials Today Physics*, 2021. **16**: p. 100327.
129. Kim, S., et al., *Electronic structure and thermoelectric properties of p-type Ag-doped Mg₂Sn and Mg₂Sn_{1-x}Si_x (x = 0.05, 0.1)*. *Journal of Applied Physics*, 2014. **116**(15): p. 153706.
130. Kamila, H., et al., *Analyzing transport properties of p-type Mg₂Si–Mg₂Sn solid solutions: optimization of thermoelectric performance and insight into the electronic band structure*. 2019. **7**(3): p. 1045-1054.
131. Ponnusamy, P., et al., *Efficiency as a performance metric for material optimization in thermoelectric generators*. 2021.
132. Naithani, H., E. Müller, and J. De Boor, *Developing a two-parabolic band model for thermoelectric transport modelling using Mg₂Sn as example*. In preparation, 2021.
133. Ponnusamy, P., J. de Boor, and E. Müller, *Using the constant properties model for accurate performance estimation of thermoelectric generator elements*. *Applied Energy*, 2020. **262**: p. 114587.
134. Helmers, L., et al., *Graded and stacked thermoelectric generators—numerical description and maximisation of output power*. 1998. **56**(1): p. 60-68.
135. Pei, Y., et al., *High thermoelectric figure of merit in heavy hole dominated PbTe*. *Energy and Environmental Science*, 2011. **4**(6): p. 2085-2089.

136. Müller, E., S. Walczak, and W. Seifert, *Optimization strategies for segmented Peltier coolers*. *physica status solidi*, 2006. **203**(8): p. 2128-2141.
137. Schilz, J., et al. *On the composition function of graded thermoelectric materials*. in *Materials science forum*. 1999. Trans Tech Publ.
138. Li, T., et al., *Thermoelectric properties and performance of flexible reduced graphene oxide films up to 3,000 K*. *Nature Energy*, 2018. **3**(2): p. 148-156.

Co-authorship statement

The co-author contribution for the three publications presented in this thesis are as follows. These were published in peer-reviewed journals with accordance to the corresponding journals regulations.

Publication 1 (Chapter 3): Ponnusamy, P., J. de Boor, and E. Müller, *Using the constant properties model for accurate performance estimation of thermoelectric generator elements*. *Applied Energy*, 2020. **262: p. 114587.**

Contributor	Affiliation and Contact details	Contribution
Prasanna Ponnusamy, M.Sc. (First and corresponding author)	German Aerospace Center, Institute of Materials Research, Dept. of Thermoelectric Materials & Systems, Cologne, 51147, Germany. Prasanna.ponnusamy@dlr.de	Conceptualization, Methodology, Software, Validation, Formal analysis, Investigation, Resources, Data curation, Writing - original draft, Visualization.
Johannes de Boor, Dr.rer.nat Jun-Prof.	German Aerospace Center, Institute of Materials Research, Dept. of Thermoelectric Materials & Systems, Cologne, 51147, Germany. Johannes.deboor@dlr.de	Conceptualization, Methodology, Supervision, Project administration, Funding acquisition,

		Writing - review & editing.
Eckhard Müller, Dr.rer.nat Prof. (corresponding author)	German Aerospace Center, Institute of Materials Research, Dept. of Thermoelectric Materials & Systems, Cologne, 51147, Germany. Justus Liebig University Giesen, Institute of Inorganic and Analytical Chemistry, D-35392 Giesen, Germany. Eckhard.mueller@dlr.de	Conceptualization, Methodology, Supervision, Project administration, Funding acquisition, Writing – review & editing.

Publication 2 (Chapter 4): Ponnusamy, P., de Boor, J., and Müller, E., *Discrepancy between constant property model and temperature dependent material properties for performance estimation of thermoelectric generators. Entropy 22.10 (2020): 1128.*

Contributor	Affiliation and Contact details	Contribution
Prasanna Ponnusamy, M.Sc. (First and corresponding author)	German Aerospace Center, Institute of Materials Research, Dept. of Thermoelectric Materials & Systems, Cologne, 51147, Germany. Prasanna.ponnusamy@dlr.de	Conceptualization, Methodology, Software, Validation, Formal analysis, Investigation, Resources, Data curation, Writing - original draft, Visualization.
Johannes de Boor, Dr.rer.nat Jun-Prof.	German Aerospace Center, Institute of Materials Research, Dept. of Thermoelectric Materials & Systems, Cologne, 51147, Germany. Johannes.deboor@dlr.de	Supervision, Project administration, Funding acquisition, Validation, Formal analysis, Investigation, Writing - review & editing.

Eckhard Müller, Dr.rer.nat Prof. (corresponding author)	German Aerospace Center, Institute of Materials Research, Dept. of Thermoelectric Materials & Systems, Cologne, 51147, Germany. Justus Liebig University Giesen, Institute of Inorganic and Analytical Chemistry, D-35392 Giesen, Germany. Eckhard.mueller@dlr.de	Conceptualization, Methodology, Validation, visualization, Formal analysis, Investigation, Supervision, Project administration, Funding acquisition, Writing – review & editing.

Publication 3 (Chapter 5): Ponnusamy, P., Kamila, H., Müller, E., and de Boor, J.,
Efficiency as a performance metric for material optimization in thermoelectric generators.
Journal of Physics:Energy (2021).

Contributor	Affiliation and Contact details	Contribution
Prasanna Ponnusamy, M.Sc. (First and corresponding author)	German Aerospace Center, Institute of Materials Research, Dept. of Thermoelectric Materials & Systems, Cologne, 51147, Germany. Prasanna.ponnusamy@dlr.de	Conceptualization, Methodology, Software, Validation, Formal analysis, Investigation, Resources, Data curation, Writing - original draft, Visualization.
Hasbuna Kamila, Dr.rer.nat	German Aerospace Center, Institute of Materials Research, Dept. of Thermoelectric Materials & Systems, Cologne, 51147, Germany. hasbuna.kamila@dlr.de	Software, Validation, Visualization.

<p>Eckhard Müller, Dr.rer.nat Prof.</p>	<p>German Aerospace Center, Institute of Materials Research, Dept. of Thermoelectric Materials & Systems, Cologne, 51147, Germany.</p> <p>Justus Liebig University Giesen, Institute of Inorganic and Analytical Chemistry, D-35392 Giesen, Germany.</p> <p>Center for Materials Research/LaMa, Justus Liebig University, Giessen, D-35392 Giessen, Germany.</p> <p>Eckhard.mueller@dlr.de</p>	<p>Validation, visualization, Investigation, Supervision, Project administration, Funding acquisition, Writing – review & editing.</p>
<p>Johannes de Boor, Dr.rer.nat Jun-Prof. (corresponding author)</p>	<p>German Aerospace Center, Institute of Materials Research, Dept. of Thermoelectric Materials & Systems, Cologne, 51147, Germany.</p> <p>Faculty of Engineering, Institute of Technology for Nanostructures (NST), University of Duisburg-Essen, Building BA, Bismarckstr. 81, 47057 Duisburg, Germany.</p> <p>Johannes.deboor@dlr.de</p>	<p>Conceptualization, Methodology, Supervision, Project administration, Funding acquisition, Validation, Formal analysis, Investigation, Writing - review & editing.</p>

DuEPublico

Duisburg-Essen Publications online

UNIVERSITÄT
DUISBURG
ESSEN

Offen im Denken

ub | universitäts
bibliothek

Diese Dissertation wird via DuEPublico, dem Dokumenten- und Publikationsserver der Universität Duisburg-Essen, zur Verfügung gestellt und liegt auch als Print-Version vor.

DOI: 10.17185/duepublico/77081

URN: urn:nbn:de:hbz:465-20230420-121301-4



Dieses Werk kann unter einer Creative Commons Namensnennung - Nicht kommerziell - Keine Bearbeitungen 4.0 Lizenz (CC BY-NC-ND 4.0) genutzt werden.